Dissertation
submitted to the
Combined Faculties of the Natural Sciences and Mathematics
of the Ruperto-Carola-University of Heidelberg, Germany
for the degree of
Doctor of Natural Sciences

put forward by
Raúl Tonatiuh Jiménez Bustamante, MSc
born in Coyoacán, Mexico City, Mexico
Oral examination: 22.06.2018

Inclusive J/ψ production at mid-rapidity in Pb–Pb collisions at $\sqrt{s_{\mathrm{NN}}} = 5.02$ TeV

Referees: Prof. Dr. Silvia Masciocchi
Prof. Dr. Stephanie Hansmann-Menzemer

A Luz María, Raúl y a mi abuela
Nunca dejaré de agradecerles todo el cariño

“One does not discover new lands without consenting to lose sight of the shore for a very long time" André Gide

“Thou shalt say what thou doest, and thou shalt be able to justify it out of thine own mouth: not the mouth of thy supervisor, nor thy colleague who did the analysis last time, nor thy local statistics guru, nor thy mate down the pub” R. Barlow.

Zusammenfassung

Die Produktion von Charmonium ist eine Schlüsselobservable im Studium der Eigenschaften des Quark-Gluon-Plasmas, das in ultrarelativistischen Schwerionenkollisionen erzeugt wird. Der ALICE-Detektor am LHC bietet die einzigartige Möglichkeit, Charmonium bei mittlerer Rapidität und niedrigem Transversalimpuls zu untersuchen. J/ψ-Mesonen können aus ihrem dielektronischen Zerfallskanal J/$\psi \rightarrow e^+e^-$ rekonstruiert werden. Diese Doktorarbeit stellt die Messung inklusiver J/ψ Produktion in Pb–Pb Kollisionen bei einer Schwerpunktsenergie von $\sqrt{s_{\mathrm{NN}}} = 5.02$ TeV vor. Aufgrund der hohen integrierten Luminosität, die von ALICE während der zweiten Betriebsphase des LHC aufgenommen wurde, konnte der nukleare Modifikationsfaktor von inklusivem J/ψ als Funktion der Zentralität, sowie als Funktion des Transversalimpulses in verschienen Zentralitätsklassen gemessen werden. Der nukleare Modifikationsfaktor von inklusivem J/ψ zeigt eine Zunahme bei niedrigem Transversalimpuls, wobei ein Wert um Eins herum erreicht wird, und eine Unterdrückung bei hohem Transversalimpuls, wo Mechanismen des Energieverlusts dominieren. Eine qualitative Beschreibung der Messungen kann mit Modellen erreicht werden, die einen hohen Anteil an J/ψ Produktion aus Rekombination beinhalten. Darüber hinaus wird die Beobachtung der Zunahme von J/ψ Produktion bei mittlerer Rapidität in periphären Kollisionen bei niedrigem Transversalimpuls (< 150 MeV/c) vorgestellt.

Abstract

Charmonium production is a key observable in the study of the properties of the Quark-Gluon Plasma created in ultrarelativistic heavy-ion collisions. The ALICE detector at the LHC provides unique capabilities at mid-rapidity to study charmonium production at low transverse momentum. J/ψ mesons can be reconstructed via their dielectron decay channel J/$\psi \rightarrow e^+e^-$. This thesis presents the measurement of inclusive J/ψ production in Pb–Pb collisions at the center of mass energy of $\sqrt{s_{\mathrm{NN}}} = 5.02$ TeV. Due to the large integrated luminosity collected by ALICE during the second stage of operation of the LHC, the inclusive J/ψ nuclear modification factor was measured as a function of centrality and as a function of transverse momentum in different centrality classes. The inclusive J/ψ nuclear modification factor exhibits an enhancement towards lower transverse momentum, reaching a value around unity, and a suppression at high transverse momentum where energy-loss mechanisms are dominant. A qualitative description of the measurements is achieved by the models which include a large fraction of J/ψ production by recombination. In addition, in peripheral collisions the observation at mid-rapidity of an excess of J/ψ with low transverse momentum (< 150 MeV/c) is presented.

Index

1

Introduction

In this chapter, a basic theoretical background is presented, starting with a brief description of the Standard Model in Section 1.1. The field theory of the strong interactions is presented in Section 1.2 followed by a brief description of the Quark-Gluon Plasma in Section 1.3. Several general properties of the Heavy-ion collisions are discussed in Section 1.4, and the common variables used in heavy-ion collisions are introduced in Section 1.5.

1.1 The Standard Model

The Standard Model (SM) [1–3] of the elementary particles and their interactions is the fundamental framework in particle physics developed in the early 1970's and has successfully explained many experimental results. The SM describes the composition of matter and the interaction between particles via the fundamental forces, the electromagnetic, the weak and the strong force. Gravity does not enter in the standard model and all the efforts to include it has been unsuccessful so far. Fermions are the basic constituents of matter and are particles with half-integer spin. The bosons can be classified into two types: scalar and vector bosons. The vector bosons are particles with spin 1 in charge of the interactions between fermions. The photons (γ), $W^{\pm}$, Z^0 mediate the electro-weak interaction, while the gluons (g) mediate the strong force. The scalar boson with spin 0 corresponds to the Higgs boson and is responsible for providing mass to the particles. The classification of fermions and bosons is shown in Figure 1.1.

The fermions are classified in 3 families of leptons: (e, ν_e), (μ, ν_μ), (τ, ν_τ); and 3 families of quarks (u, d), (s, c), (b, t). The leptons have electric charge $Q = -1$ and its neutrinos $Q = 0$. The quarks u, c, t have an electric charge $Q = +2/3$, while the charge of the quarks d, s, t is $Q = -1/3$. The antiparticles complement the SM.

The 4 fundamental interactions of nature are summarized in Table 1.1. The theory focused on the study of the strong interaction is known as Quantum Chromodynamics (QCD). Quantum Electrodynamics (QED) focuses on the electromagnetic interaction. The weak force is described by the electroweak interaction which incorporates the electromagnetic interaction.

Interaction	Gravity	Weak	Electromagnetic	Strong
Acts on	Massive particles	Leptons, quarks	Charged particles	Quarks and gluons
Gauge boson	Graviton	W^+, W^-, Z^0	Photon (γ)	8 Gluons
Strength	$\approx 10^{-42}$	$\approx 10^{-13}$	$\approx 10^{-2}$	10

Table 1.1: Fundamental interactions. Each interaction is mediated by the exchange of gauge bosons between the particles the interaction acts on. The values of the relative strength are also shown. The strength of the interactions depends on the nature on the source and distance, specially for the weak interaction. The numbers on the table should not be taken literally. Values taken from Ref. [5].

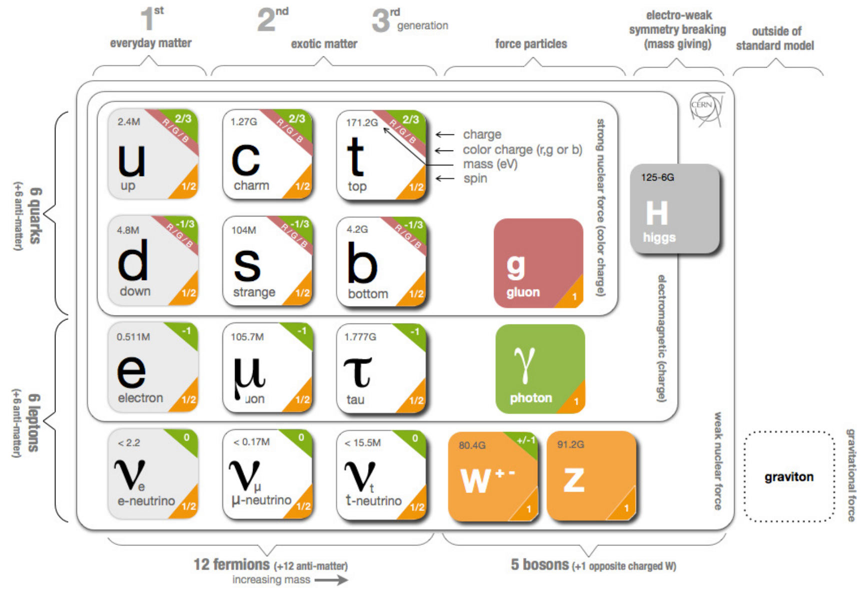

Figure 1.1: Basic constituents of the Standard Model. Figure taken from Ref. [4].

1.2 Quantum Chromodynamics

Quantum Chromodynamics (QCD) is a non-abelian gauge field theory of the strong interaction and describes the interactions between quarks and gluons. Its Lagrangian, invariant under local SU(3) symmetry transformations, can be written as:

$$\mathscr{L}_{\rm QCD} = -\frac{1}{4}\sum_a F^a_{\mu\nu}F^{\mu\nu}_a + \sum_f^{N_f} \bar{\Psi}_f \left(i\gamma^\mu\partial_\mu - g\gamma^\mu \sum_a A^a_\mu \frac{\lambda^a}{2} - m_f \right) \Psi_f, \tag{1.1}$$

where Ψ_f represents the quark fields with the index f indicating the quark flavor ($f = u, d, s, c, b, t$). The term A^a_μ accounts for the gluon field with color index a for the different colors ($a = 1, ...8$). The strong coupling constant is represented with g, the Dirac and Gell-Mann matrices are represented by the terms γ^μ and λ^a, respectively.

The term $F^{\mu\nu}_a$ represents the non-linear gluon field strength and is defined as:

$$F^{\mu\nu}_a = \partial^\mu A^\nu_a - \partial^\nu A^\mu_a - g f_{abc} A^b_\mu A^c_\nu, \tag{1.2}$$

where the coefficients f_{abc} are the structure constants of the SU(3) group. The Lie algebra of the SU(3) group is defined in terms of the generators of the SU(3) group. These generators correspond to the Gell-Mann matrices divided by a factor two and satisfy the commutation rules

$$\left[\frac{\lambda_a}{2}, \frac{\lambda_b}{2}\right] = i f_{abc} \frac{\lambda_c}{2}. \tag{1.3}$$

The local SU(3) gauge transformations of the quark wave function has the form $\Psi \rightarrow \Psi' = U(x)\Psi$, where the matrices $U(x) \in \mathrm{SU}(3)$. The $\mathscr{L}_{QCD}$ will remain invariant under transformation if at the same time, the gluon field changes according to the rule:

$$A^\mu = A^\mu_a \frac{\lambda_a}{2} \rightarrow A'^\mu = U(x)A^\mu U^{-1}(x) - \frac{i}{g} U(x)\partial^\mu U^{-1}(x). \tag{1.4}$$

In the perturbative QCD framework (pQCD), one can solve the renormalization group equation for the running coupling constant to first order [6, 7] obtaining:

$$\alpha_s(Q^2) = \frac{12\pi}{(33 - 2n_f)\ln(Q^2/\Lambda^2_{QCD})} \tag{1.5}$$

where n_f is the number of participating flavors and Q represents the momentum transfer in a given process. The term Λ_{QCD} represents the intrinsic QCD scale parameter at which perturbative QCD cannot be applied anymore, and may be thought of as the parameter setting the boundary between the partonic and hadronic worlds. The value of the coupling defined in the most widely used scheme corresponds to $\Lambda_{\mathrm{QCD}} \approx 200$ MeV [8]. Note that α_s blows up as the momentum transfer approaches Λ_{QCD}. The running coupling constant has been measured at different energy scales as shown in Figure 1.2 [8]. At large values of Q^2, the coupling constant decreases continuously, until the quarks behave as quasi-free particles. This behavior is denominated asymptotic freedom. At small values of Q and larges distances, the opposite behavior is observed, and the interaction between the quarks increases with distance. Neither quarks nor gluons have been observed as free particles. The quarks and gluons are contained in color-neutral objects denominated hadrons. This feature of the strong interaction is called *confinement*.

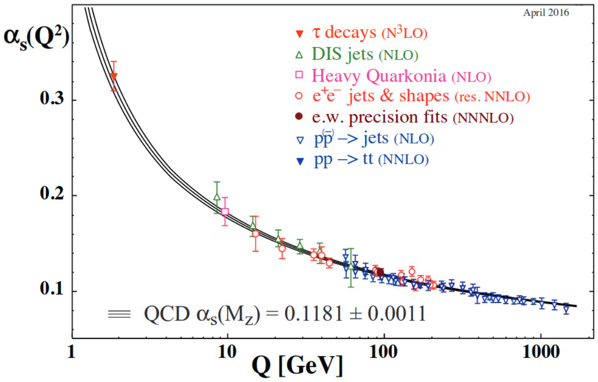

Figure 1.2: Running of the strong coupling constant α_s as a function of the momentum transfer Q. Measurements are compared with the parameterization based on measurements at the scale of the Z-boson mass. Figure taken from Ref. [8].

1.3 The Quark-Gluon Plasma

The considerations explained above apply at low temperatures and low energy densities. However, in the limit of very high temperature $T \gg \Lambda_{\mathrm{QCD}}$, the interactions between quarks and gluons with thermal momenta $p \approx T$ are negligible. These particles will form a non-interacting plasma of color charges denominated Quark-Gluon Plasma (QGP) [9]. As the quarks and gluons are no longer confined into hadrons in the QGP, this indicates the existence of a phase transition separating the low-temperature hadronic phase from the high-temperature QGP phase. This is illustrated in the QCD phase diagram shown in Figure 1.3 where the QCD phase diagram is shown as a function of temperature (T) and net baryonic density (ρ).

The point $T = \rho = 0$ in the phase diagram corresponds to the vacuum of QCD, the white region in the lower-left corresponds to the ordinary hadronic matter under confinement. The point at $T = 0, \rho = 1$ indicates the nuclear matter under normal conditions in the universe. The regions concerning the nuclei are well understood within the nuclear theory. The phase of color superconductivity at high baryon density will not be discussed here, as it is not expected to play a role in the ultra-relativistic heavy-ion collisions. The arrow at high temperature indicates that the phase transition was first experienced by the early universe, where the QPG was created after the Big Bang. the phase transition can be investigated nowadays with the ultra-relativistic heavy-ion colliders [11, 12], starting from the two nuclei colliding at sufficiently high energies. The aim of ultra-relativistic heavy ion collisions is to study the QCD phase transition and physics of the QGP. The phase transition with increasing the temperature can also be studied in the lattice QCD framework [13]. Current studies indicate a critical temperature T_C of about $T_C = 150 - 170$ MeV [14, 15].

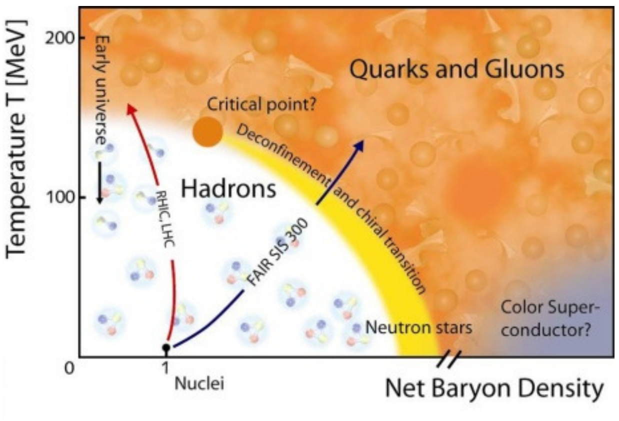

Figure 1.3: The phase diagram for QCD matter, as a function of net baryonic density and temperature. Figure taken from Ref. [10].

1.4 Heavy-ion collisions

The evolution of the system created in the heavy-ion collisions (shown in Figure 1.4) can be divided into different phases [16]. The earliest time after the initial nuclear impact is considered the pre-equilibrium stage where hard parton scattering processes occur leading to the creation of high p_{T} particles *e.g.* jets; heavy quarks *e.g* charm, and vector bosons. The formation of a bound state of charm-anticharm quark pairs will be discussed in Chapter 2. The pre-equilibrium phase is rapidly followed by a QGP-thermalization phase, in which the quarks and gluons suffer multiple scatterings leading to a formation of a system in local thermal equilibrium. The medium expands hydrodynamically and cools down. When the plasma reaches the T_C of the QGP phase transition, the quarks and gluons get bounded within colorless hadrons. Inelastic interactions among the hadrons can take place in the still dense medium in local thermal equilibrium. Eventually, after further expansion, the density becomes so low that the hadrons stop interacting and the system freezes-out. First, chemically, fixing the relative abundance of hadron species and then kinetically, fixing the momentum distributions of the final state particles that stream to the detectors.

Centrality of a heavy-ion collision

A fundamental concept used to classify the different types of nucleus-nucleus collisions is the centrality of the collision. Figure 1.5 illustrates the collision of two nuclei, which are Lorentz contracted, separating the so-called participant and spectator nucleons. The nucleons that undergo in at least one binary collision (N_{coll}) with nucleons of the other nucleus are called participants (N_{part}). The nucleons that do not interact with other nucleons on their way and keep traveling undeflected, close to the beam are denominated spectators.

The impact parameter (b) represents the distance between the centers of the two colliding nuclei in the plane transverse to the collision axis. The impact parameter is used to classify the events in different centrality classes: the collisions where $b \approx 0$ are called central collisions; the collisions where $b \lesssim$ two times the radius of the nuclei are denominated peripheral collisions. The minimum-bias (MB) collisions correspond to the measurements averaged over different impact parameters. A more detailed description and the way to determine it experimentally will be presented in Section 3.5.

Elliptic flow

In central heavy-ion collisions, the spatial distribution of the created system is approximately symmetric, resulting in radial expansion. In semi-central collisions, the initial asymmetric overlap region of the particle production has an almond shape in the transverse plane as shown in Figure 1.6. Due to the pressure gradients, the almond-shaped region becomes more symmetric as the system expands. This spatial asymmetry leads to an azimuthal asymmetry

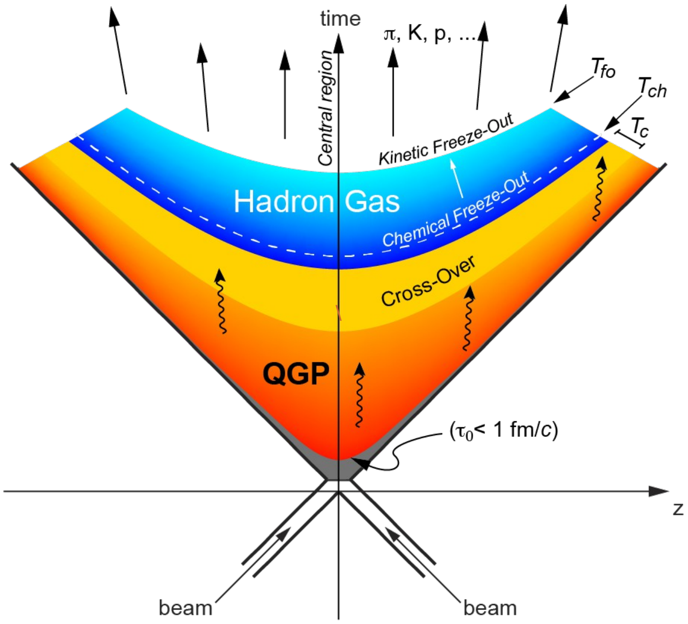

Figure 1.4: Space-time diagram of the longitudinal evolution of the Quark-Gluon Plasma.

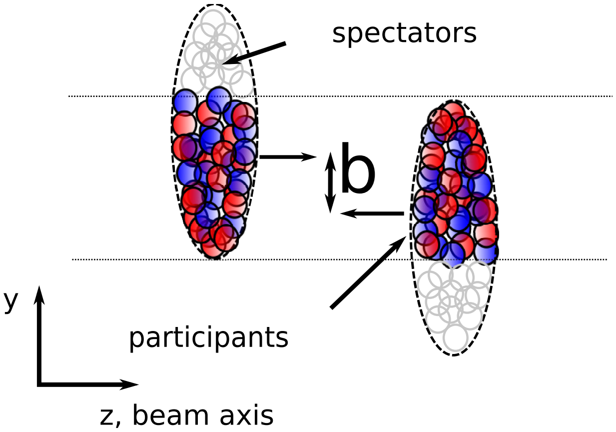

Figure 1.5: Schematic view of a nucleus-nucleus collision with impact parameter $\vec{b}$. The participant nucleons are represented in color (red, blue). The spectator nucleons are shown in white.

of the momentum distributions of the particles produced with respect to the reaction plane. The reaction plane is defined by the impact parameter and the beam directions. The angle Ψ_R determines the direction of the reaction plane with respect to the beam axis.

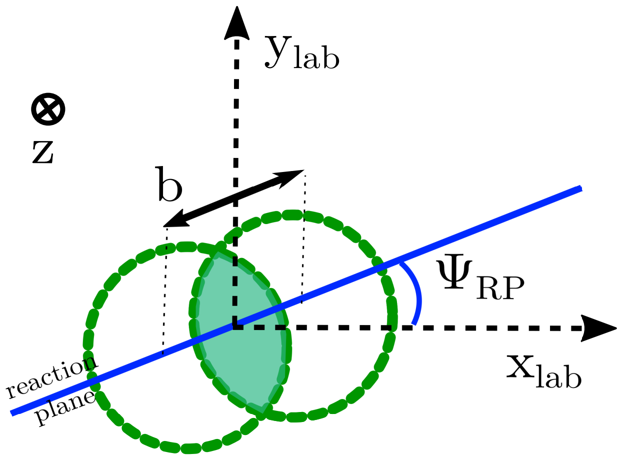

Figure 1.6: Schematic view of the collision geometry in the transverse plane to the beam direction. The variables are explained in the text.

1.5 Kinematics and detector acceptance

In colliders, the phase space of the produced particles is commonly studied differentially in terms of the transverse momentum ($p_{\rm T}$) and the rapidity (y). The $p_{\rm T}$ is defined as the momentum component perpendicular to the beam axis $p_{\rm T} = \sqrt{p_x^2 + p_y^2}$. Experimentally the $p_{\rm T}$ is obtained from the curvature of the track. On the other hand, y is defined in terms of the energy of the particle (E) and its longitudinal momentum (p_z) as:

$$y = \frac{1}{2} \ln \frac{E + p_z}{E - p_z}. \tag{1.6}$$

Commonly the region around $y = 0$ is called mid-rapidity, while large positive or negative values of y are defined as forward or backward rapidity. An analogous variable is the pseudo-rapidity (η), defined as:

$$\eta = -\ln\left(\tan\frac{\theta}{2}\right) = \frac{1}{2} \ln \frac{|\vec{p}| + p_z}{|\vec{p}| - p_z}, \tag{1.7}$$

where θ represents the angle between the momentum direction of the particle and the beam axis. The variable η is commonly used since is a purely geometrical quantity.

2

Charmonium

In this chapter, the properties of interest of the J/ψ meson are described. A general introduction to the charmonium family and its characteristics are presented in Sections 2.1 to 2.3. The production mechanisms of J/ψ in pp collisions and the production mechanisms that could lead to changes in the J/ψ production in heavy-ion collisions are explained in Sections 2.4 and 2.5, respectively. This chapter concludes with an experimental overview of J/ψ results obtained at different energies to assess the results obtained in this work.

2.1 The November revolution: the discovery of the J/ψ

The first experimental evidence for the existence of a charm quark came with the discovery of the J/ψ meson in 1974. The discovery was made simultaneously by two different experiments: in Brookhaven National Laboratory (BNL) [17], a particle, named J, was observed in the process $pBe \rightarrow e^+e^-$; at Standford Linear Accelerator Center (SLAC) [18] the particle named ψ was observed in three different decay channels $e^+e^- \rightarrow$ (1) hadrons, (2) e^+e^-, and (3) $\mu^+\mu^-$, $\pi^+\pi^-$, K^+K^-. As the discovery was made at the same time, the particle is named nowadays J/ψ and the Nobel prize in 1976 was shared among Samuel Ting and Burton Richter who were the leaders of the research team at BNL and SLAC, respectively. The J/ψ is a bound state of a charm-anticharm ($c\bar{c}$) quark with quantum numbers $J^{PC} = 1^{--}$ and has a mass of 3096.900 ± 0.006 MeV/c^2 [8]. The higher $c\bar{c}$ bound state ψ(2S) $\equiv \psi'$ was discovered a couple of weeks later at SLAC [19]. Both resonances have a narrow decay width of 92.9 ± 2.8 keV for the J/ψ and 296 ± 8 keV [8] for the ψ(2S) indicating a long lifetime. Appelquist and Politzer [20] suggested the existence of charmonium before the discoveries at SLAC and BNL. A plausible explanation for the two resonances was that they corresponded to $c\bar{c}$-quarks bound states, with a mass below the threshold for the production of two hadrons with charm quark content. Some predictions for the spectrum were made [21] and due to its similarities with the positronium, the system was named charmonium.

2.2 Charmonium family

Besides the J/ψ meson (1S), and the ψ(2S), there are other four stable charmonium bound states (shown in Figure 2.1), which differ from the J/ψ in the quantum number and mass, the scalar η_c (1S), and three χ_c(1P) states. Charmonium states with masses below the open charm mass threshold ($m(D\bar{D})$ = 3729 MeV/c^2) are considered stable since they cannot decay to non-charmonium states without the annihilation of the $c\bar{c}$-quark pair. The annihilation of the $c\bar{c}$- quark pair to form light-flavored hadrons follows an old phenomenological rule commonly known as the Okubo-Zweig-Iizuka [22] (OZI). Although the strong decays are not forbidden by any conservation law, they are suppressed. One gluon decay of the $c\bar{c}$ pair annihilation is forbidden due to color conservation. In addition, for charmonium states *e.g.* $^3S_1$ the two-gluons final state is excluded by the negative C parity of the initial state.

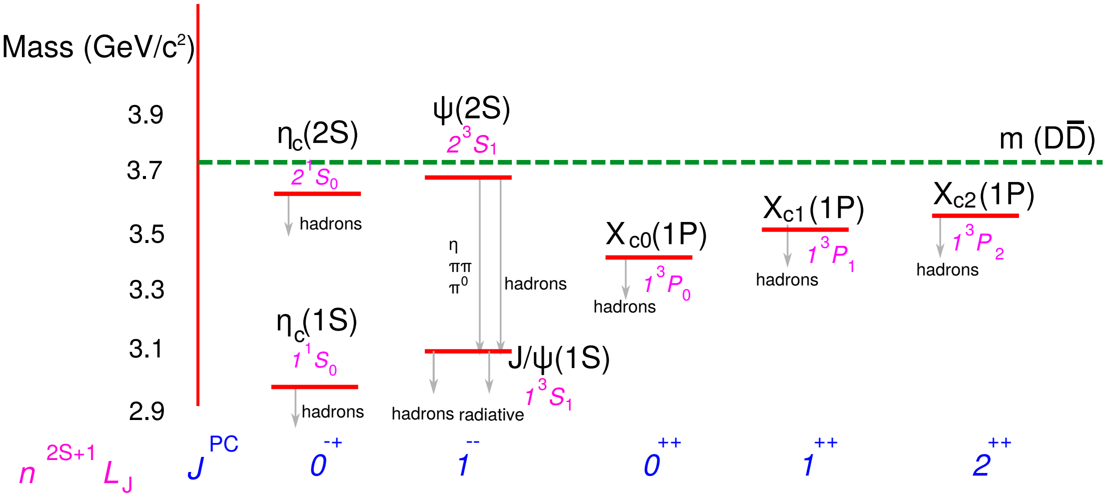

Figure 2.1: Member of the charmonium family below the open charm mass threshold ($m_{D\bar{D}}$), only hadronic transitions are shown, the single photon transitions are omitted for clarity. The J^{PC} values of angular momentum ($J = L + S$), the parity ($P = (-1)^{L+1}$) and the charge conjugation parity ($C = (-1)^{L+S}$) are shown at the bottom of the figure. The spectroscopic notation for each state is shown in magenta.

Due to the high bare mass of the c quark ($m_c \approx 1.3$ GeV/c^2), its velocity in the quarkonium rest frame can be considered small. The *Cornell potential* [23] was proposed to calculate quarkonium properties based in the non-relativistic potential theory [24]. The binding potential shown in Eq. 2.1 has a Coulomb-like term and an increasing linear term to prevent free quarks.

$$V(r) = -\frac{4\alpha_s}{3r} + k \cdot r \tag{2.1}$$

The first term corresponds to the Coulomb-like part which dominates at short distances and represents the single-gluon exchange between a quark and an antiquark. The factor 4/3 accounts for the Casimir factor corresponding to SU(3) group [1] and α_s represents the strong (running) coupling constant of QCD. A common value assigned to k corresponds to $k \approx$0.2 GeV^2 [25]. The second term ($k \cdot r$) corresponds to the confining potential, with r representing the separation between the quark-antiquark and k representing the string tension.

The mass of the quarkonium levels shown in Figure 2.1 can be obtained solving the Schrödinger equation using the potential of Eq. 2.1. Table 2.1 contains some charmonium properties, *e.g.* the binding energy (ΔE), the separation between the charm quarks (r_0) and the mass difference between experimental and calculated values (ΔM) obtained using the Cornell potential showing an agreement within 1 % with the measured values.

State	J/ψ	χ_c	ψ'
$M_{\rm exp}$ (GeV/c^2)	3.0969	3.4148-3.5562	3.6861
ΔE (GeV)	0.642	0.324-0.183	0.053
ΔM (GeV/c^2)	0.02	-0.03	0.03
r_0 [fm]	0.50	0.72	0.90

Table 2.1: Charmonium properties: mass, and binding energy (ΔE) defined as the difference between the quarkonium masses and the open charm threshold. The values of ΔM show the difference from the values obtained by solving the Schrödinger equation and the data, with an agreement within 1 % in all cases. The potential does not include any spin-orbit or spin-spin couplings, therefore no separation between the three χ_c states or the separation between J/ψ and η_c are possible. Values are taken from [25].

---

[1] The Casimir operator commutes with the generators of SU(N) and it is calculated according to the SU group as $\frac{N^2-1}{2N}$.

2.3 Inclusive J/ψ production

Inclusive J/ψ production refers to all the observed final-state J/ψ regardless of the source. The inclusive J/ψ production in hadronic collisions is composed of three different sources (see Figure 2.2 (Left)) enlisted in the following.

- The direct production includes the J/ψ generated directly from a hard parton-parton scattering.
- The feed-down from heavier directly produced charmonium states includes decays like $\chi_c \rightarrow \mathrm{J}/\psi + \gamma$ and $\psi(2\mathrm{S}) \rightarrow \mathrm{J}/\psi + \mathrm{X}$, where X refers to any unobserved particle. The feed-down from χ_c into J/ψ has been measured as a function of p_{T} by two different experiments: The Collider Detector at Fermilab (CDF) at Tevatron [26] in the mid-rapidity region ($|y_{\mathrm{J}/\psi}| < 0.6$) at $\sqrt{s} = 1.8$ TeV and LHCb [27] [2] at forward rapidity (2.0< $y_{\mathrm{J}/\psi} < 4.5$) in pp collisions at $\sqrt{s} = 7.0$ TeV. The measurements show a χ_c feed-down going from 12% up to 31%. The fraction of feed-down J/ψ from ψ(2S) has been estimated from the ratio of the J/ψ and ψ(2S) cross-sections in pp collisions in [28–30]; resulting in a fraction of ψ(2S) feed-down of approximately 8% constant with $\sqrt{s}$ and p_T. The sum of the directly produced J/ψ and J/ψ's from a decay of heavy charmonium states is referred to as prompt production.
- The non-prompt J/ψ's are produced in the weak decays of hadrons containing a b-quark [3]. Due to the relatively long lifetime of b-hadrons ($c\tau \approx 500\ \ \mu$m), its vertex is usually displaced from the primary vertex.

The fraction of non-prompt J/ψ production (f_B) in Pb–Pb collisions has been measured in complementary p_{T} regions by ALICE [31] and CMS [32]. Additionally, the non-prompt J/ψ production has been also measured in pp collisions at several LHC energies by ATLAS [33], CMS [34] and ALICE [35]. Figure 2.2 (right) shows the measured p_{T} dependence of f_B in pp and Pb–Pb collisions. The fraction of non-prompt J/ψ production has a strong p_{T} dependence. Starting from 10% it increases with p_{T} up to 70% in pp and 30 % in Pb–Pb collisions.

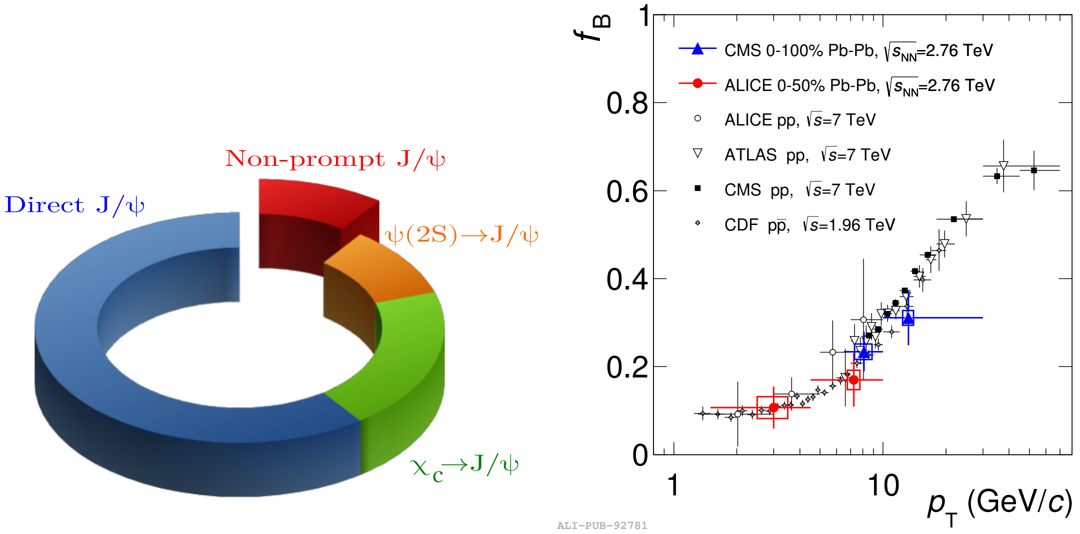

Figure 2.2: *Left*: Different fractions of inclusive J/ψ production at central rapidity integrated over p_{T}. *Right*: Measurements showing the fraction of non-prompt J/ψ as a function of p_{T} measured by CDF ($|y_{\mathrm{J}/\psi}| < 0.6$) [36], CMS ($|y_{\mathrm{J}/\psi}| < 0.9$) [32, 34], ATLAS ($|y_{\mathrm{J}/\psi}| < 0.75$) [33], and ALICE in $|y_{\mathrm{J}/\psi}| < 0.8$ in Pb–Pb and ($|y_{\mathrm{J}/\psi}| < 0.9$ in pp collisions [31, 35].

---

[2] LHCb, CMS, ATLAS ans ALICE are the four main experiments at the Large Hadron Collider (LHC). A brief introduction to the LHC and these four experiments will be discussed in Chapter 3.

[3] This refers to b-flavored hadrons: B^+, B^0, B^0_S, Λ_b and their antiparticles.

2.4 Charmonium production in pp collisions

The LHC [4] accessible parton kinematics region in pp collisions at $\sqrt{s} = 13$ TeV, with a rapidity coverage $|y| < 6.0$, is shown in Fig 2.3 (Left). For a state with a mass $M = Q$ at an energy=13 TeV and at a given rapidity (y) the incoming partons have a Bjorken-$x_{1,2} = \frac{M}{13\text{TeV}} e^{\pm y}$, where Q is the four-momentum, and Bjorken-x refers to the momentum fraction carried by the parton. The inspected Bjorken-x region regime $\approx 10^{-2} - 10^{-4}$, at a factorization scale $Q = 10$ GeV^2, correspond to the region on the parton distribution functions, where the gluons dominate over the quarks, as shown on the right side of Figure 2.3. The dominant charmonium production processes at LHC energies correspond to gluon fusion. Example of corresponding Feynman diagrams of this processes ([37, 38]) are shown in Figures 2.4 to 2.7, their relevance will be discussed through the description of the different models.

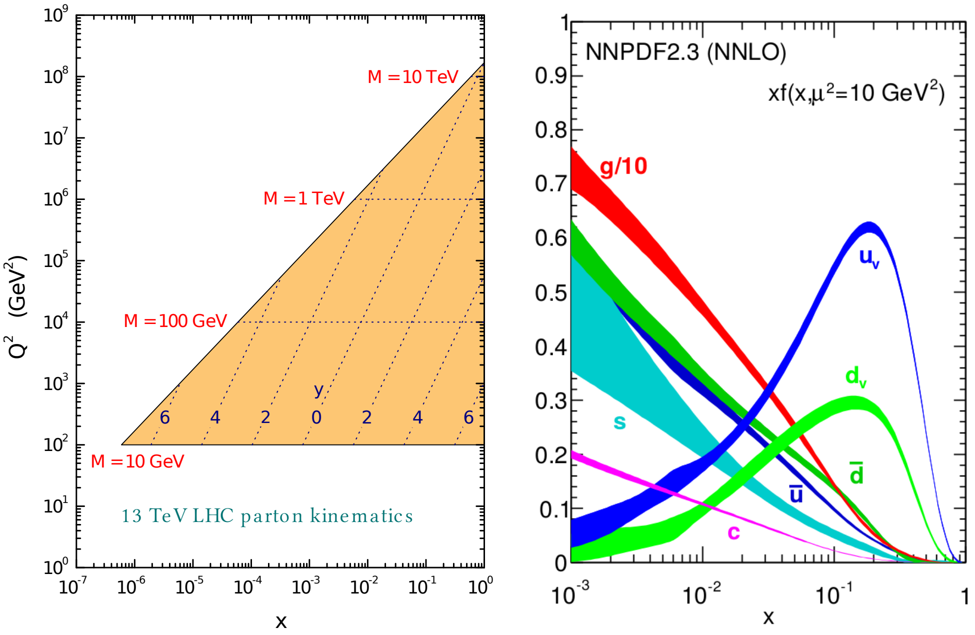

Figure 2.3: Left: Accessible values of factorization scale (Q^2) and Bjorken-x range for different rapidities based on an energy $\sqrt{s} = 13$ TeV. Right: Proton parton distribution functions at scales $Q^2 = 10$ GeV^2. Figures taken from [8].

The charmonium production can be separated into two stages. In the first stage the $c\bar{c}$-quark pair is produced through a hard-parton scattering in a very short formation time $\tau_{c\bar{c}} \approx 1/2m_c \approx 0.05$ fm. After the $c\bar{c}$-pair is produced, the quarks can either bind with light quarks and form open charm particles or bind together to form a charmonium state. The second stage consists of obtaining the charmonium bound state from the $c\bar{c}$ pair, with the correct angular momentum, and spin quantum numbers.

Since the bare charm quark mass is much larger than the $\Lambda_{QCD} \approx 200$ MeV, the associated values to the coupling constant (α_s) are much smaller than one and perturbative QCD (pQCD) computations can be applied for the first stage. Additionally, it is necessary to neutralize the color charge of the $c\bar{c}$ pair produced because the final bound state is colorless. The formation time of the charmonium bound state can be estimated in a model-independent approach [39] and can be related to the mass splitting between the states 1S and 2S, thus the formation time $\tau_{J/\psi} \approx (m_{2S} - m_{1S})^{-1} \approx 0.3 - 0.4$ fm. Another approach [40] estimates $\tau_{J/\psi} \approx 2m_c\lambda_{QCD} \approx 0.25$ fm based on the lowest energy allowed for the emitted gluon. In principle due to the large difference in time scales between $\tau_{c\bar{c}}$ and $\tau_{J/\psi}$, non-perturbative processes like gluon emission can occur. The time scale introduced here will also be relevant for the charmonium production in heavy-ion collisions discussed in Section 2.5.

The two stages of charmonium production are used in most of the models. The hadronization stage computation is the main difference between the models. In addition, they may consider or neglect different orders of Feynman diagrams. Currently, the different models proposed to describe charmonium production are the Color Evaporation

---

[4] The Large Hadron Collider will be explained in detail in Section 3.1.

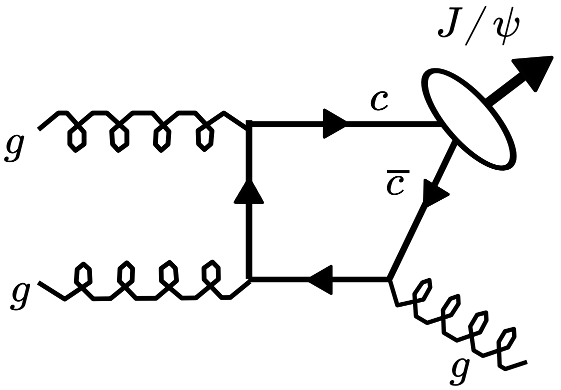

Figure 2.4: Leading-order color-singlet: $g + g \to c\bar{c}[^3S_1^{(1)}] + g$.

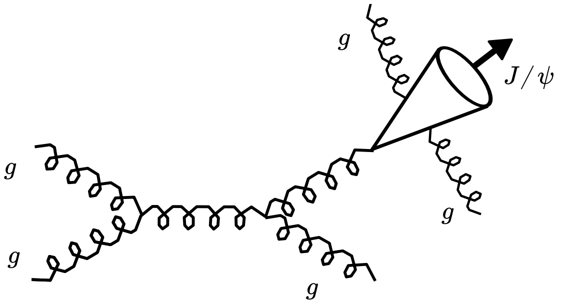

Figure 2.5: Color-singlet fragmentation: $g + g \to [c\bar{c}[^3S_1^{(1)}] + gg] + g$

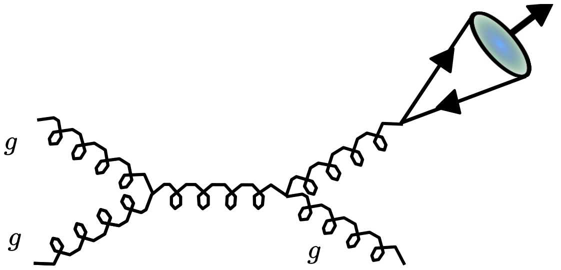

Figure 2.6: Color-octet fragmentation: $g + g \to c\bar{c}[^3S_1^{(8)}] + g$.

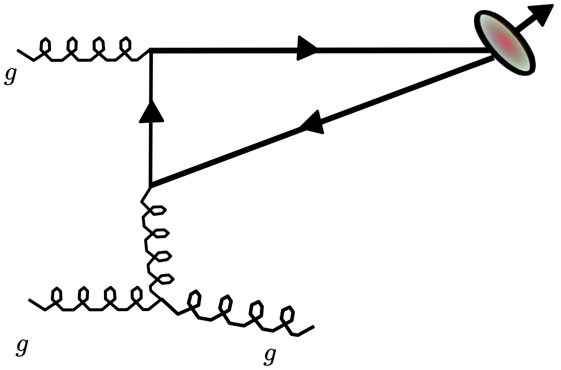

Figure 2.7: Color-octet t-channel gluon exchange: $g + g \to c\bar{c}[^3S_1^{(8)}, P_J^{(8)}] + g$.

Model (CEM), the Color-Singlet Model (CSM) and the Non-Relativistic QCD (NRQCD) model. None of them achieves an entirely successful theoretical description of charmonium production when compared to the current data. In the following, these production mechanisms are briefly described. A more detailed description and comparisons can be found in Ref. [41].

Color Evaporation Model

The Color Evaporation Model (CEM) [42] is a simple approach that describes the quarkonium formation probability in a statistical manner. The model assumes that the $c\bar{c}$-pair is produced in a color-octet state and after its production, the spin and the color of the pre-resonance state is randomized by non-perturbative gluon emissions. The produced $c\bar{c}$ pair neutralizes its color interacting with the color field; hence the color is ”evaporated”. This model also takes into account that quarks can either combine with light quarks to produce charm-flavored hadrons or bind together to form charmonium. The CEM calculates the total cross-section to produce a charmonium state σ_{ch} obtained from integrating the cross section of the $c\bar{c}$ pair, obtained with pQCD, over the invariant mass gap from $2m_c$ to the lowest mass meson that can be formed with the charm quark, $2M_D$, like:

$$\sigma_{\mathrm{ch}} = \frac{1}{9}\int_{2m_c}^{2M_D} \mathrm{d}m \frac{\mathrm{d}\sigma_{c\bar{c}}}{\mathrm{d}m} \tag{2.2}$$

where σ_{ch} is distributed among the charmonium states. Thus the cross section to produce a J/ψ is determined by: $\sigma_{J/\psi} = f_{J/\psi}\sigma_{\mathrm{ch}}$, where $f_{J/\psi}$ is an energy independent factor that is determined in a phenomenological way. This leads directly to the constant and energy independent production ratios of different charmonium states (1,2): $\sigma_m(s)/\sigma_n(s) = f_m/f_n = const.$

The model is not able to provide any information about the polarization of charmonium and presents some discrepancies in describing the transverse momentum spectra.

Color-Singlet Model

The Color-Singlet Model [43, 44] assumes that the quantum state of the produced $c\bar{c}$ pair does not change during the binding stage, neither in spin nor in color [5]. Therefore, as the physical state is color neutral, the pair produced must be a color-singlet state ${}^3S_1^{(1)}$; hence the name Color-Singlet Model (CSM). An example Feynman diagram for this process is shown in Figure 2.4.

As the $c\bar{c}$ pair is already produced in a color-singlet state, the velocity of the c quarks in the meson must be small. Therefore the two constituents quarks must be at rest in the meson reference frame, while the hard gluon is produced. The perturbative part is calculated from Feynman diagrams while the non-perturbative part, corresponding to the binding probability, is related to the quarkonium wave function obtained from the potential model. In the potential model, the amplitude to produce the meson can be expressed in terms of the L’th derivative [43] of the radial wavefunction at the origin ($R_S(0)$). $R_S(0)$ can be extracted from the experimentally measured leptonic decay widths (Γ_{ee}) of the corresponding state. In the case of J/ψ:

$$\Gamma_{ee} \equiv \Gamma(\mathrm{J}/\psi \to l^+ + l^-) \approx 4\frac{\alpha^2}{9m_c^2}|R_{\mathrm{J}/\psi}(0)|^2 \tag{2.3}$$

Then the inclusive differential cross section for the J/ψ state plus some other specific final state (X) in the CSM has the form:

$$\mathrm{d}\sigma(\mathrm{J}/\psi + X) = \mathrm{d}\hat{\sigma}(c\bar{c}({}^3S_1^{(1)}) + X)|R_{\mathrm{J}/\psi}(0)|^2 \tag{2.4}$$

where the first term $\hat{\sigma}(c\bar{c}({}^3S_1^{(1)}) + X)$ corresponds to the inclusive cross section for producing the correct singlet state calculated in pQCD.

Later on, it was noticed that the terms to LO were not sufficient to describe the CDF data. In particular, they failed in the predictions of the $\psi(2S)$ production by a factor 50 [45]. Fragmentation processes as the ones shown in Figure 2.5 have to be considered in the calculations to describe the data. These processes are higher in order of α_s compared to the gluon splitting process (Figure 2.4). The color-singlet fragmentation process shown in

---

[5] The gluon radiation from the c quarks are suppressed by one power of α_s at the chosen scale.

Figure 2.5 is enhanced by a power $p_{\mathrm{T}}^4/(2m_c)^4$, therefore at high p_{T} ($p_{\mathrm{T}} \gg 2m_c$), the mass can be neglected and this contribution can overtake the fusion contribution. Including the color-singlet fragmentation process in the CSM calculations, the CDF data was still not well described, indicating that additional fragmentation contributions were missing. The gluon splitting processes into color-octet states, ${}^3S_1^8$, as shown in Figures 2.6 and 2.7 are now believed to be the dominant production processes of J/ψ and $\psi(2S)$ at large p_{T}. Including these contributions into the calculations gives a better description of the data within uncertainties. These terms added a posteriori in this model are included naturally in the model explained in the following.

Non-Relativistic QCD

The Non-Relativistic QCD (NRQCD) model [46] is based on an effective field theory, which treats the charmonium as a non-relativistic system, i.e. $\beta = v/c << 1$. In addition to the expansion in powers of α_s done by the other models, the NRQCD factorization introduces an expansion in the velocity v of the heavy quark in the quarkonium rest of frame. It accounts for higher Fock states [6], following the velocity scaling rules [46]. Therefore the quarkonium bound state $|Q\rangle$ has the schematic form:

$$|Q\rangle = \mathcal{O}(1)|q\bar{q}[{}^3S_1^{(1)}]\rangle + \mathcal{O}(v)|q\bar{q}[{}^3P_j^{(8)}g]\rangle + \mathcal{O}(v^2)|q\bar{q}[{}^3S_1^{(1,8)}gg]\rangle + ..., \tag{2.5}$$

where the indexes (1) and (8) indicate the color state of the $q\bar{q}$ pair, and the $\mathcal{O}(v^n)$ represents the order of the velocity expansion at which each Fock state participates in the creation of charmonium. The dominant Fock state $|q\bar{q}[{}^3S_1^{(1)}]\rangle$ consist of a color-singlet state. The higher Fock states, such as $\mathcal{O}(v)|q\bar{q}[{}^3P_j^{(8)}g]\rangle$ include dynamical gluons. In this scenario the differential cross section for the production of the Q bound state associated with a hadron X has the form:

$$\mathrm{d}\sigma(Q+X) = \Sigma \mathrm{d}\hat{\sigma}(q\bar{q}[{}^{2S+1}L_J^{(1,8)}] + X)\langle\mathcal{O}^Q[{}^{2S+1}L_J^{(1,8)}]\rangle. \tag{2.6}$$

where the sum stands for the angular momentum quantum numbers S, L, J and the color. The term $\langle\mathcal{O}^Q[{}^{2S+1}L_J^{(1,8)}]\rangle$ corresponds to the long distance matrix elements (LDME), which take into account the transition between the $q\bar{q}$ pair and the final Q bound state with small relative velocity and energies of order $m_Q v^2$. The LDMEs have a known scaling with v and the current phenomenology of J/ψ, $\psi(2S)$ production uses LDMEs for calculations up to $\mathcal{O}(v^4)$ (see Ref. [47]).

The NRQCD factorization naturally includes both color-singlet and color-octet states (see Feynman diagrams in Figures 2.4 to 2.7). The leading order matrix element for J/ψ $\langle\mathcal{O}^{J/\psi}[{}^3S_1^{(1)}]\rangle$ corresponds to the CSM case, which can be calculated from quarkonium electromagnetic rates as in Eq. 2.3. The color-octet LDME occurs at higher orders in v.

The matrix elements for the color-octet states are determined through comparisons with measurements in pp collisions for one or more processes. Each matrix element has a particular p_{T} dependence. Thus the matrix elements are fitted to the measured p_{T} spectrum in order to make predictions for other processes.

Experimental results

In this section, a brief overview of the experimental results is shown. In general data and the NLO predictions of NRQCD factorization and CSM for quarkonium production agree within uncertainties. However, no definite conclusion can be made due to the theoretical uncertainties. A review of the comparisons between data and theory can be found in Refs. [41, 48].

Figure 2.8 (Left) shows the comparison between the inclusive J/ψ differential cross section as a function of p_{T} measured by ALICE [49] and calculations performed in the CSM including NLO and NNLO contributions. The NRQCD calculations comparison to the same data is shown in Figure 2.8 (Right) where the non-promt production from FONLL is added. Both calculations show a reasonable agreement with the data within the uncertainties.

Although the NRQCD and CSM models provide the most sophisticated theoretical approach, they have some weak points like the fact that the factorization assumptions may not hold at low p_{T}. In addition, polarization

---

[6] In quantum mechanics, a Fock state or number state is a quantum state that is an element of a Fock space with a well-defined number of particles.

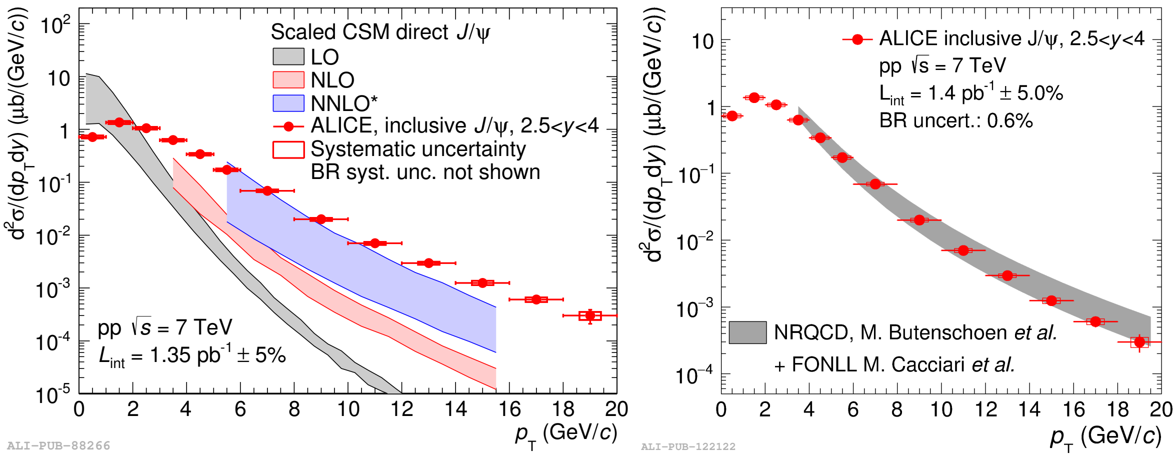

Figure 2.8: Inclusive J/ψ production cross section as a function of p_T in pp collisions at $\sqrt{s} = 7$ TeV. Left: Comparison to CSM calculations. Right: Comparison to NRQCD + FONLL calculations. Figures taken from [49].

measurements are not well reproduced by either of these models (see Ref. [50]) and the measurement of η_c by LHCb [51] is not well described by NRQCD (see Ref. [52]).

In summary, the quarkonium production mechanisms in pp collisions are currently not yet fully understood. There is no model with a global description of the differential cross sections down to low p_T that also describes the polarization measurements. Several attempts to understand quarkonium production are ongoing.

2.5 Charmonium production in heavy-ion collisions

The suppression of charmonium production in heavy-ion collisions was initially proposed as a probe of deconfinement in the dense matter in 1986 [53]. In the original picture suggested it was assumed that the charmonium is rapidly formed after a hard scattering and destroyed in the plasma afterward. In such a medium the color charges are free so that the binding energy potential between the $c\bar{c}$-quark pairs is subject to the color screening by gluons and light quarks, which limits the range of the strong interactions.

The Debye screening length can be determined in lattice gauge theory by calculating the correlation function between a static $c\bar{c}$-quark pair immersed in a gluon heat bath. The gluon exchanged will acquire mass due to the temperature of the heat bath. The Coulomb-like potential part of Eq. 2.1 becomes:

$$\frac{-\alpha_s}{r} \rightarrow \frac{-\alpha_s}{r} e^{-r\mu(T)}, \tag{2.7}$$

where $\mu = 1/r_D$ corresponds to the Debye mass and r_D corresponds to the screening length (radius) and $\mu = \mu(T)$ increases with temperature. Following [54] the confining term is modified so that

$$kr \rightarrow k\Big(\frac{1 - e^{-r\mu(T)}}{\mu(T)}\Big). \tag{2.8}$$

Therefore, the two terms of the Cornell potential from Eq. 2.1 can be parametrized as:

$$V(r,T) \approx \frac{k}{\mu(T)}\Big(1 - e^{-r\mu(T)}\Big) - \frac{\alpha_s}{r} e^{-r\mu(T)}. \tag{2.9}$$

In the case $\mu(T) = 0$, the confining part (Eq. 2.8) can be expanded up to the second term like $\frac{k}{\mu}(1-[1-\mu r+...]) \approx kr$; while the Coulomb-like part (Eq. 2.7) becomes $\frac{-\alpha_s}{r} e^{r\mu(T)} = \frac{-\alpha_s}{r}$, recovering the original form of the Cornell potential. This gives a qualitative picture of the mechanism and it can be observed that when the temperature increases the screening gets stronger. The temperature at which the quarkonium bound state dissociates due to the screening depends on the corresponding binding energy of the state. The dissociation of different states can provide a way to measure the temperature of the medium formed. In this picture, a subsequent dissociation according to the radius size of the different charmonium states (see Table. 2.1) should be observed. As the larger and heavier states $\psi(2S)$ and χ_c contributes by feed down into the J/ψ production, a reduction in the total J/ψ production as a function of the energy density should be observed as sketched in Figure 2.9.

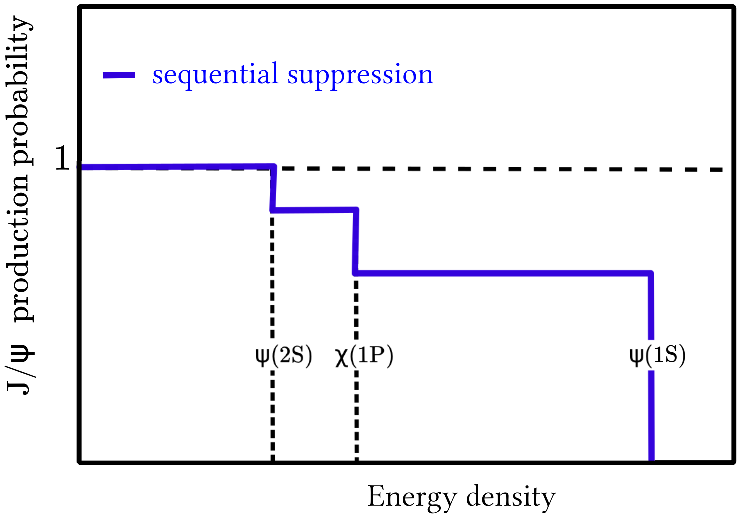

Figure 2.9: Sequential J/ψ suppression.

This representation of the $c\bar{c}$-quark pairs static potential immersed in a gluon heat bath is the starting point to have a qualitative description. A more quantitative and sophisticated description based on Effective Field Theories (EFT) has been developed during the last years (see Ref. [55]). However, a dynamical description of the $c\bar{c}$-quark pairs in the medium remains still as a significant challenge. Nevertheless, first investigations addressing a more realistic scenario description are ongoing (see Ref. [56]).

As discussed in the previous section the charmonium bound state formation requires time to form a bound state after the $c\bar{c}$ quark pair is produced. The formation time of the $c\bar{c}$-quark pair is $\tau_{c\bar{c}} \approx 1/2m_c \approx 0.05$ fm, while the formation time of the J/ψ is larger ($\tau_{J/\psi} \approx 0.25 - 0.4$ fm). The formation time of the QGP produced in heavy-ion collisions at LHC energies (TeV) is likely to be comparable to $\tau_{c\bar{c}}$. The different time scales imply that neither the charmonium nor the pre-resonance state exists before the plasma is formed.

2.5.1 Charmonium (re)-generation

In the year 2000 two new different approaches ([57, 58]) predicted an enhancement of the charmonium production in heavy-ion collisions at LHC energies with respect to the melting scenario previously discussed. The charmonium production can be approximated in terms of the total charged hadrons N_{ch}, leading to $N_{J/\psi} \propto N_{c\bar{c}}^2/N_{ch}$ [59]. At LHC collision energies a considerable increase of the average $c\bar{c}$-quark pairs is expected in comparison to the Super Proton Synchrotron (SPS) and the Relativistic Heavy Ion Collider (RHIC) [7] collision energies. According to the two models, an enhancement of the charmonium production instead of suppression is foreseen at LHC energies. The charmonium states can be formed either at the phase boundary based on a statistical approach or via destruction and formation through a kinetic approach in the plasma. A more detailed description of the models is given in the following.

---

[7] The different results at the different collision energies at SPS and RHIC will be discussed in Section 2.7

Statistical Hadronization Model

The Statistical Hadronization Model (SHM) [57, 60, 61] is based on a grand canonical approach to describe the production of light flavor hadrons [8] showing great success in the description of particle ratios and yield. In this approach, the only fit parameters to estimate the yields are the chemical freeze-out temperature (T), the baryochemical potential (μ_b), and the volume (V). These parameters are obtained for each collision energy from a global fit to particles yields. The energy dependence shows an increase in the temperature with increasing collision energy, flattening at a value ≈ 160 MeV.

Since the thermal production of charm quarks can be neglected, this model assumes that all the $c\bar{c}$-quark pairs are produced by hard scattering. The initially produced charm quarks hadronize together with the light quarks and gluons at the phase boundary.

As the parameters T, μ_b and V are fixed, the only additional parameter used in this model is the charm cross section per unity of rapidity $\frac{d\sigma_{c\bar{c}}}{dy}$. The SHM predicts an increase of the J/ψ production in more central heavy-ion collisions at LHC energies and a rapidity dependence with a maximum at mid-rapidity due to the rapidity dependence of the charm cross section.

Transport models

The Transport models [58, 62–64] assume a slightly different approach where the evolution of the system is treated dynamically. The models assume the possibility of forming a J/ψ directly in the deconfined medium. Therefore, all combinations of $c\bar{c}$-quark pairs are allowed to form a bound state, and continuous dissociation and regeneration of charmonium over the whole deconfined stage is possible. The space-time evolution is described by the relativistic Boltzmann equation which depends on the dissociation rate and the phase-space of each heavy quark in the plasma. The main ingredients in the rate equation are the inelastic reaction rate for dissociation and formation, and the charmonium equilibrium limit. The reaction rate is calculated using QCD to NLO in the quasi-free approximation [65] considering processes like $g + J/\psi \rightarrow g + c + \bar{c}$ induced by the light partons (g) of the heat bath (u, d, s, anti-quarks and gluons). The charmonium equilibrium limit is defined in terms of a thermal relaxation time as a parameter of the model which controls the regeneration contribution in the rate equation. Besides, several inputs from experimental data are required *e.g.* quarkonium and heavy quarks cross sections (including shadowing corrections and nuclear absorption effects). The space-time evolution of the medium assumes an isotropic fireball hydrodynamical-like.

Currently, two transport models present a quantitative description of J/ψ production in AA collisions (This will be addressed in Chapter 4). On the one hand, the model by Rapp et al. described in detail in [63] and on the other hand the model of Zhao et al. described in [64]. The rate equation has been extended to provide a p_{T} dependent charmonium production in heavy-ion collisions [66]. As the (re)generation occurs in the fireball evolution, it is expected that the thermally produced charmonium is dominant at low p_{T} values.

Comovers model

The comovers interaction model [67] (CIM) assumes the interaction of the comoving matter together with the recombination of charm quarks into secondary charmonium states, with a similar dynamic approach as the transport models. The CIM is based on the gain and loss differential equations in transport theory. This includes a term to consider the contribution due to recombination with a magnitude defined by the charm density in pp collisions at the same energy.

2.5.2 Photo-production

Photo-production of J/ψ may also occur in ultra-peripheral nucleus-nucleus collisions (UPCs), where the impact parameter of the collision is larger than two times the radius of the nucleus, due to the strong electromagnetic field of the nuclei. When a nucleus is accelerated to ultra-relativistic speeds, the charges inside the nucleus become a source of (quasi-real) photons [68]. The J/ψ production mechanism in such collisions is shown in Figure 2.10. The

---

[8] All hadrons which include a quark u, d and s.

virtual photon is emitted by one of the accelerated nuclei producing a quark-antiquark pair which then interacts with the other nucleus producing a J/ψ. These processes can be either coherent when the photon couples with the nucleons as a whole; or incoherent when the photon couple only with one of the nucleons.

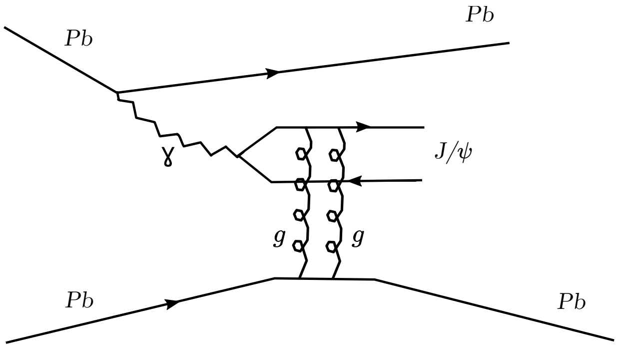

Figure 2.10: Lowest order Feynman diagram for J/ψ photo-production.

The coherent photo-production is characterized by the very low p_{T} of the J/ψ ($\langle p_{\mathrm{T}}\rangle \approx 60$ MeV/c) and no break up of the nucleus. The incoherent production is characterized by a higher p_{T} of the J/ψ ($\langle p_{\mathrm{T}}\rangle \approx 500$ MeV/c) and the nucleus breaks up, but except for single nucleons or nuclear fragments in the very forward region no other particles are produced [69]. Currently, the theoretical models are only applied to UPCs ($b > 2R$) in order to avoid the production due to strong interactions. LHC measurements of J/ψ photo-production in hadronic peripheral collisions lead to new theoretical challenges (see Section 2.7).

2.6 Cold-nuclear matter effects

In order to identify the physical effects on the charmonium production due to the presence of the medium, the additional effects arising from the presence of nuclear matter have to considered. These effects are generally studied in proton-nucleus collisions and are denominated Cold Nuclear Matter effects (CNM) because no hot, dense matter effects are expected to be present. The CNM effects include the modification of the parton distribution functions in the nucleus relative to the nucleon, the Cronin effect and the nuclear absorption of the charmonium state passing through the nucleus [70]. As this thesis is focused in Pb–Pb, only a brief description of the CNM effects is presented in the following. More details can be found in Refs. [41], [71].

Gluon-shadowing

The modification of the parton distribution function due to the presence of other nucleons in the nucleus is known as gluon-shadowing. The nuclear parton distribution functions (nPDF) in the nucleus (A), $f_i^A(x, Q^2)$, are defined as[72]:

$$f_i^A(x, Q^2) = S_i^A(x, Q^2) f_i(x, Q^2), \tag{2.10}$$

where $S_i^A(x, Q^2)$ represents the partonic modification with respect to the free proton PDF ($f_i(x, Q^2)$) (see Figure 2.3) due to the nucleons, x represents the Bjorken-x and Q^2 the four momentum transfer. For values in the region of Bjorken $x \approx 10^{-2} - 10^{-6}$, corresponding to the LHC energies at mid-rapidity, the PDF is suppressed inside the nucleus as shown in Figure 2.11. The shadowing parameterization has large associated uncertainties, since the modifications of the gluon density cannot be directly measured. Shadowing parameterizations are derived from global fits to the nuclear parton distribution functions.

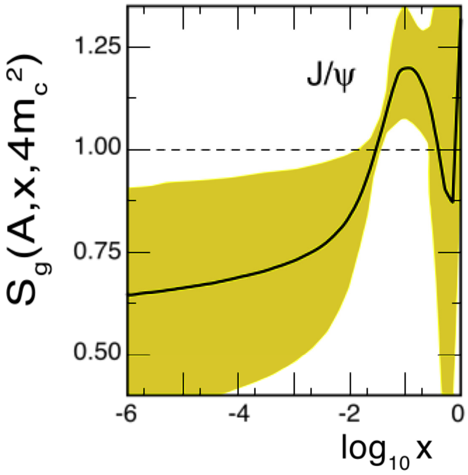

Figure 2.11: EPS09 gluon-shadowing parameterization at $Q = 2m_c$ in a Pb nucleus. Central value is indicated with the line, the shaded yellow band represents the uncertainty. Figure taken from [70, 72].

Nuclear absorption

The nuclear absorption corresponds to the probability of the $c\bar{c}$ pre-resonance state to be dissociated due to its traversal through the nucleus, resulting in a decrease of the cross-section. Recent measurements show that the effective absorption cross-section at $y \approx 0$ decreases with energy as shown in Figure 2.12. At LHC energies the nuclear absorption is negligible because short crossing-over time of the colliding particles.

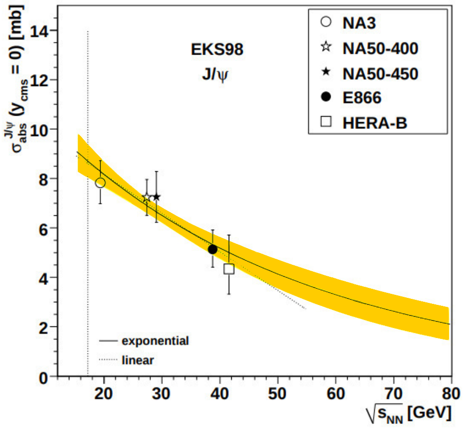

Figure 2.12: J/ψ nuclear absorption cross-section as a function of center-of-mass energy. The solid line represents the fit with an exponential and the error band. The dotted line indicates the linear fit. Figure taken from [73].

Cronin effect

The observation of a peculiar enhancement around of the hadron production when comparing the hadron production in pA with respect to pp collisions is denominated Cronin effect [74]. This enhancement is interpreted as the partons experiencing multiple scatterings with the target nucleons while traversing the nucleus before the hard scattering. Studies show that the Cronin effect may be relevant for the J/ψ [75]. A shift in the transverse momentum of the J/ψ to lower values resulting in a decrease of the average transverse momentum of the J/ψ with respect to pp collisions may be observed.

2.7 Experimental results: Lessons from previous measurements

Different experiments at different collision energies have measured J/ψ production in heavy-ion collisions during the past decades. This section contains experimental charmonium results previously obtained by different experiments up to the results obtained during the first stage of LHC operation (LHC Run 1) [9]. This will serve as an introduction to set the experimental state of the art previous to the realization of this work, which will be discussed in the following chapters.

Most of the models assume that the number of charm quarks is conserved throughout the evolution of the system after its creation. The thermal production is negligible due to the large mass of the $c\bar{c}$. Also, the annihilation rate in the QGP is negligible at LHC energies [76]. Therefore, modifications of the inclusive charmonium production imply a change in the inclusive open charm production, dominated by the open charm mesons which account for $\leq 1\%$ of the total charm cross section. The study of the J/ψ yield relative to the inclusive $c\bar{c}$-pairs would be the ideal observable to quantify any modification in the charmonium production due to the medium [77, 78]. This quantity measured over the entire phase space could allow identifying the final state effects due to the cancellation of possible initial state nuclear modifications like shadowing. Currently the J/ψ yield relative to the inclusive $c\bar{c}$ is experimentally limited due to the large uncertainties in the current $c\bar{c}$-cross-section in nucleus-nucleus collisions (see Ref. [79]).

Another way to estimate medium effects is to compare the J/ψ production in nucleus-nucleus collision to the one in pp collisions at the same energy via the nuclear modification factor ($R_{\rm AA}$) as:

$$R_{AA} = \frac{\mathrm{d}^2 N_{J/\psi}/\mathrm{d}y\mathrm{d}p_T}{\langle T_{AA}\rangle \mathrm{d}^2\sigma^{\rm pp}_{J/\psi}/\mathrm{d}y\mathrm{d}p_T}. \tag{2.11}$$

where $\mathrm{d}^2 N_{J/\psi}/\mathrm{d}y\mathrm{d}p_T$ represents the yield measured in AA collisions, $\mathrm{d}^2\sigma^{\rm pp}_{J/\psi}/\mathrm{d}y\mathrm{d}p_T$ represents the J/ψ inelastic cross-section in pp collisions and $\langle T_{AA}\rangle = \langle N_{coll}\rangle/\sigma_{NN}$ represents the nuclear overlap function, the ratio of the number of binary nucleon-nucleon collisions $\langle N_{coll}\rangle$ (obtained with Glauber model) to the inelastic nucleon-nucleon cross-section σ_{NN} (see Section 3.5). This allows inspecting the medium effects present in charmonium production. In the absence of medium effects, the charmonium production scales with the number of binary nucleon-nucleon collisions and $R_{\rm AA}$ should be equal to the unity.

Nevertheless, at the Super Proton Synchrotron (SPS) the results are reported in terms of the ratio to Drell-Yan (DY) dilepton production ($q\bar{q} \to \gamma^* \to l^+ + l^-$) [10].

At RHIC and LHC collision energies most of the charm quarks are produced by gluons (see Section 2.4), therefore the comparison with DY is not meaningful. The nuclear modification factor ($R_{\rm AA}$) defined in Eq. 2.11 is used instead.

SPS and RHIC

At the Super Proton Synchrotron (SPS)[11] the measurement of NA50 at $\sqrt{s_{\rm NN}} = 150$ GeV in In-In and Pb–Pb [80] shows a slight suppression of the measured J/ψ production in the most central collisions ($N_{part} > 200$) with respect to the production expected as shown in Figure 2.13 [80].

At Relativistic Heavy Ion Collider (RHIC), with an increase of one order of magnitude in energy collision with respect to the SPS collision energies, the J/ψ nuclear modification factor was measured in Au-Au collisions at $\sqrt{s_{\rm NN}} = 200$ GeV in two different rapidity regions ($|y| < 0.35$ and $1.2 < |y| < 2.2$). A stronger suppression was expected at mid-rapidity due to the increase in energy density and temperature of the medium created in heavy-ion collisions. The Pioneering High Energy Nuclear Interaction eXperiment (PHENIX) reported the measurements shown in Figure 2.14 [81], indicating a similar suppression to the one observed at SPS collisions energies. Additionally, for the non-peripheral collisions, the $R_{\rm AA}$ suppression was stronger at forward-rapidity compared to

---

[9] The LHC Run 1 refers to the operation period of data collected between the years 2009 and 2013 (see Chapter 3).

[10] The Drell-Yan mechanism consists in the electromagnetic annihilation of a valence quark of a nucleon with a sea antiquark of a nucleon of the other nucleus. The quark annihilation a lepton pair is created through a virtual photon. Since leptons do not interact strongly, no final state interactions are expected to affect the DY production. The DY cross-section is proportional to the number of nucleon-nucleon collisions.

[11] The SPS is the second largest machine in the CERN complex (see Chapter 3).

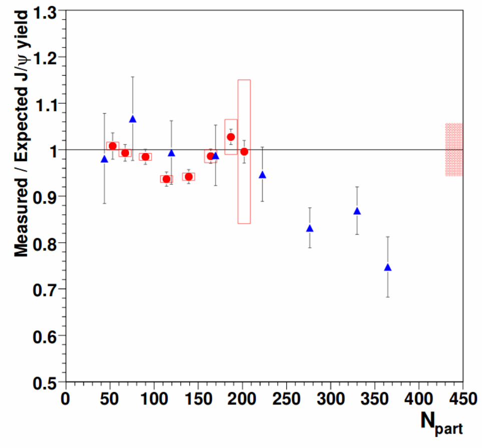

Figure 2.13: Relative J/ψ yield as a function of centrality, measured in In-In (circles) and Pb–Pb (triangles) by NA50. Figure taken from Ref. [80].

the suppression observed at mid-rapidity. This was puzzling at that time because according to the expectations a stronger suppression should be observed at mid-rapidity due to the higher energy density. This was understood with the LHC results confirming a new J/ψ production mechanisms (as predicted by [57] and [58]) emerging at collider energies.

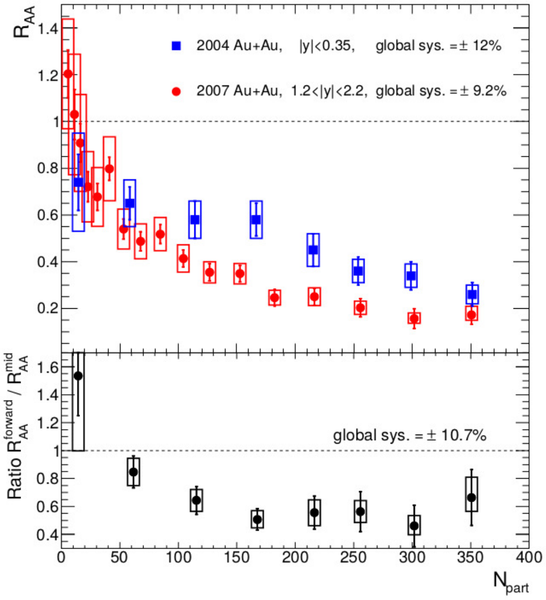

Figure 2.14: J/ψ R_{AA} as a function of N_{part} at mid and forward rapidities measured by PHENIX [81]. Lower panel shows the R_{AA} ratio between forward rapidity and mid-rapidity.

LHC

During LHC Run 1, several charmonium measurements were performed in Pb-Pb collisions at $\sqrt{s_{\mathrm{NN}}} = 2.76$ TeV. These measurements helped to disentangle between the suppression and (re)generation scenario. ALICE results in two different rapidity regions are shown in Figure 2.15. The behavior is similar to the one observed at RHIC energies where the R_{AA} is less suppressed at mid-rapidity. However, a striking difference in the relative R_{AA} values can be observed between the two experiments. The R_{AA} values in the most central collisions at LHC energies are considerably higher compared to RHIC results. There is a clear difference trend towards most central collisions between the two energies as shown on the right side of Figure 2.15 [12].

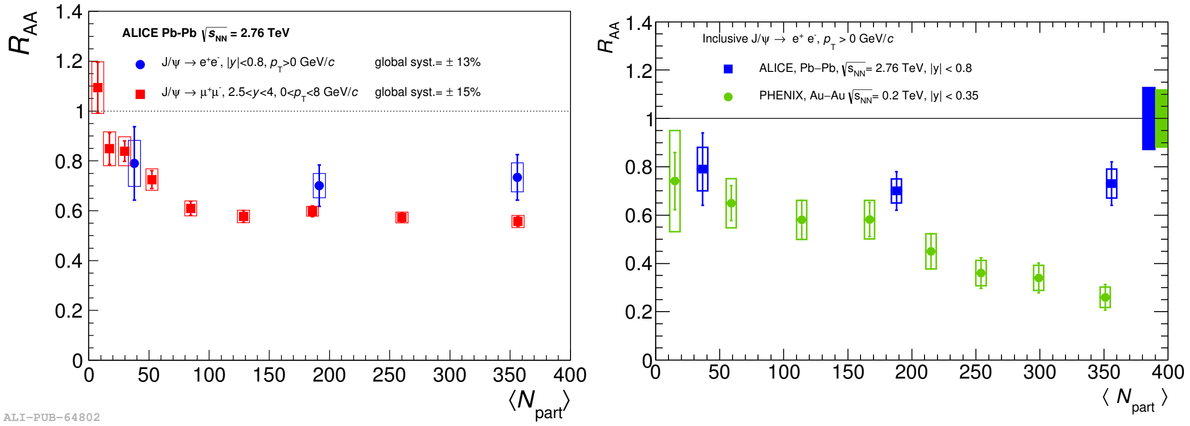

Figure 2.15: *Left*: J/ψ R_{AA} as a function of $\langle N_{part} \rangle$ measured with ALICE at mid and forward rapidity [83]. *Right*: Comparison between ALICE and RHIC measurements at mid-rapidity [81, 83]. A striking difference in the R_{AA} values for the most central case can be observed.

If the (re)combination is the mechanism responsible for the J/ψ production, it is expected to play an important role at low p_{T}. A differential measurement on p_{T} can also provide important information about the J/ψ production mechanism. ALICE measurement of the inclusive R_{AA} at mid-rapidity in three p_{T} intervals for the centrality (0-40%) is shown in Figure 2.16. The stronger difference between PHENIX and ALICE results is appreciated in the R_{AA} values at low p_{T}. The Debye screening scenario is supposed to impact the low p_{T} production. However, an enhancement with respect to PHENIX data is observed instead. The rise of the R_{AA} values towards $p_{\mathrm{T}} = 0$ is qualitatively similar in the models and the data. The transport models attribute this behavior to the dominant contribution from J/ψ regeneration. The scenario by the statistical model, in which the J/ψ is generated at chemical freeze-out. In addition it is also expected that the J/ψ production is dominated by low p_{T} J/ψ. The strong suppression at high p_{T} measured by CMS coincides in magnitude with the one observed by open charm hadrons. This may hint to the fact that the high p_{T} charm quarks have a similar energy loss within the QGP [77].

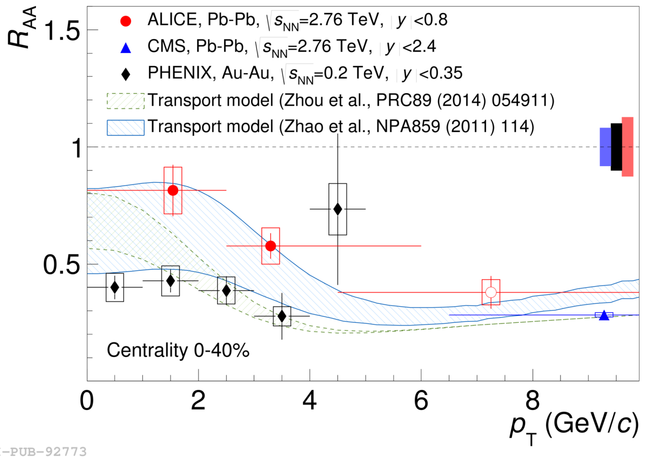

Figure 2.16: J/ψ R_{AA} measured at mid-rapidity as a function of p_{T} in central collisions (0-40%) by ALICE, PHENIX and CMS. The ALICE open marker corresponds to 0-50% centrality. Predictions by Transport models are shown. Figure from [84].

---

[12] The relative values at forward-rapidity are similar and can be consulted in [82]. The plot at mid-rapidity is shown here because the work explained in the following chapters is performed in the mid-rapidity region.

LHC Run 1 measurements point to new productions mechanisms appearing at TeV energies. The results can only be described by models including (re)combination. More precise and differential measurements could help to stifle the models and disentangle the correct physics scenario. With the current measurements it is not possible to disentangle between the transport and the statistical models. More will be discussed after presenting the discussion of the results obtained in this work.

Another interesting charmonium measurement performed in ALICE during LHC Run 1 is the measurement of an unexpected J/ψ yield excess at very low p_{T} ($< 300\mathrm{MeV}/c$) in peripheral collisions (See Figure 2.17). The potential physics origin of the J/ψ produced due to this process is photo-production. Details on the measurement can be found in [85]. Due to low statistics in peripheral collisions, the measurement was not possible at mid-rapidity in ALICE during LHC Run 1.

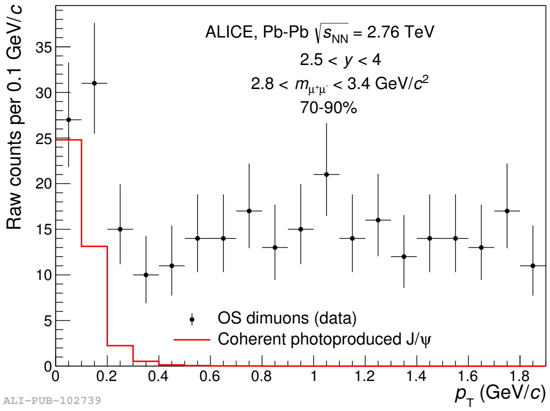

Figure 2.17: Raw dimuon p_{T} distribution in the invariant mass range $2.8 < m_{\mu^+\mu^-} < 3.4$ GeV/c^2 for peripheral collisions. The red line indicates the p_{T} distribution of coherently photoproduced J/ψ predicted by the MC generator STARLIGHT normalized by the number of J/ψ. Figure taken from [85].

After the compilation of results obtained at previous energies, it is clear that the J/ψ production is an excellent probe to study the properties of A-A collisions. Complementary to the LHC Run 1 results, it is essential to measure the evolution of the J/ψ production by increasing the collision energy and perform more differential studies with more statistics. Additional statistics to characterize the centrality and p_{T} dependence can help to constrain the models even if the uncertainties from theory side are large. LHC Run 2 provides an increase in collision energy by a factor two and also an increase in statistics for the non-central events. In the following chapters the procedure to measure J/ψ production with the ALICE detector will be explained in details going from the experimental setup in Chapter 3, and the description of the analysis in Chapters 4-5. The results will be presented in Chapter 6.

3

A Large Ion Collider Experiment at the LHC

The work presented in this thesis is based on the analysis of data collected by A Large Ion Collider Experiment (ALICE) during the year 2015. This chapter contains a brief description of the Large Hadron collider acceleration chain (Section 3.1), followed by a description of the main detector subsystems of ALICE (Section 3.2), the computing framework (Section 3.3) and the track reconstruction procedure (Section 3.4). The centrality determination is detailed in Section 3.5.

3.1 Large Hadron Collider

The Large Hadron Collider (LHC), at the European Organization for Nuclear Research (CERN), is the largest hadron collider ever built reaching the highest center-of-mass-energy ($\sqrt{s}$) ever achieved of $\sqrt{s} = 13$ TeV in the case of proton-proton (pp) collisions. The LHC has a 26.7 km circumference straddling the borders of France, at the foot of the Jura mountain, and Switzerland, near the *Léman* lake in Geneva.

The LHC has been operating since November 2009. It is currently at the second stage of operation, the so called LHC Run 2, which started in 2015. During LHC Run 2, apart from the proton-proton (pp) collisions at $\sqrt{s} = 5.02$ and $\sqrt{s} = 13$ TeV the LHC also provided proton-lead collisions at $\sqrt{s_{\mathrm{NN}}} = 5.02$ and 8.16 TeV, lead-lead (Pb–Pb) at $\sqrt{s_{\mathrm{NN}}} = 5.02$ TeV and xenon-xenon (Xe–Xe) at $\sqrt{s_{\mathrm{NN}}} = 4.44$ TeV [1].

The full LHC accelerator chain is shown in Figure 3.1. The proton production starts by removing the electrons from hydrogen gas using an electric field, then the protons are accelerated in the LINAC 2 to an energy of 50 MeV and then accelerated to 1.4 GeV in the Booster. Afterwards, they are injected in the Proton Synchrotron (PS) and accelerated up to 26 GeV. They are accelerated furthermore in the Super Proton Synchrotron (SPS) up to 450 GeV and injected in the LHC ring. Finally, in the LHC ring, they reach an energy up to 6.5 TeV.

The lead ions are produced starting from a solid lead sample, which is heated up to a temperature of 500 ^{o}C to vaporize the atoms. Afterwards, the lead vapor, similarly to the hydrogen case, is ionized by an electron current removing a few electrons from the atoms. The ions are accelerated first through a linear accelerator (LINAC3) and afterward accumulated and accelerated to 72 MeV per nucleon in the Low Energy Ion Ring (LEIR), where all remaining electrons are removed in successive steps. The vaporization, and the passage through LINAC3, and LEIR are processes uniquely done for ions. The following steps are analogous to the protons case. The ions are

---

[1] The highest center-of-mass-energy of the LHC is $\sqrt{s} = 13$ TeV for pp collisions, while for Pb–Pb collisions is $\sqrt{s_{NN}} = 5.02$ TeV. The beam energy for ions can be calculated in terms of the energy of the proton beam ($E_{\mathrm{p}} = \frac{E_{\mathrm{b}}}{Z}$) as $\sqrt{s_{NN}} = 2E_{\mathrm{p}}\sqrt{\frac{Z_1 Z_2}{A_1 A_2}}$, where $Z_{1,2}$ are the atomic number and $A_{1,2}$ are the nuclear mass number of the two colliding nuclei. The term $\frac{Z_1 Z_2}{A_1 A_2}$ determines the acceleration capability because while the uncharged neutrons are unaffected by the electromagnetic fields they remain bound in the nucleus [86].

injected in the PS, SPS and finally injected in the LHC with an energy per nucleon of 450 $Z/A = 177$ GeV. Once injected in the LHC the beams are accelerated up to the desired energy before colliding. The beams collide at four different interaction points (IP), where the main LHC experiments are located.

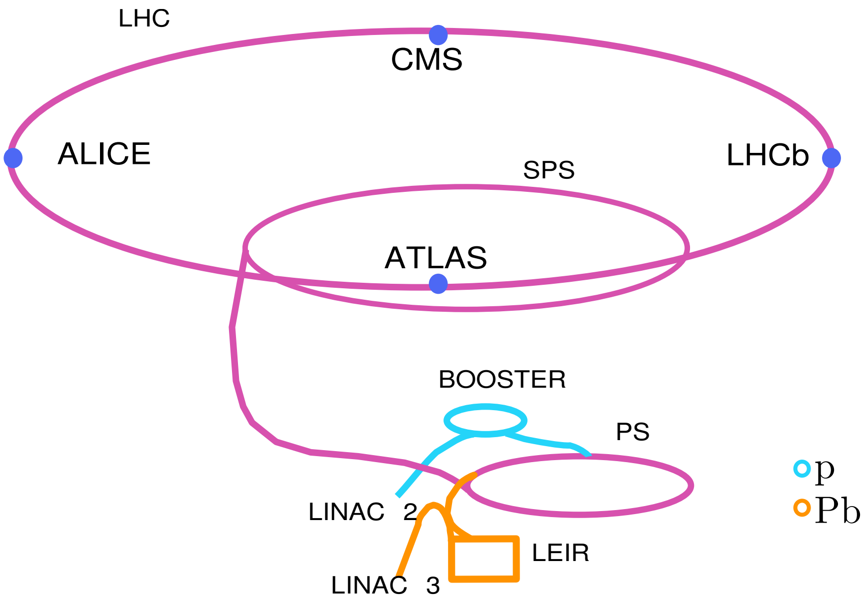

Figure 3.1: CERN accelerator chain. The different injection and acceleration chain for protons are ions are indicated with different colors. The steps after the injection in SPS is analogous for both. Details on the acceleration process are explained in the text.

The two largest experiments: A Toroidal LHC Apparatus (ATLAS) [87] and the Compact Muon Solenoid (CMS) [88] are considered as multi-purpose experiments which study a broad range of particle physics topics, including high precision measurements of the standard model and searches for physics beyond the standard model. On 4th of July 2012 the ATLAS and CMS collaborations announced the observation of a new particle, with a significance of seven sigmas. The properties of the particle discovered appear to be consistent with the Standard Model Higgs boson, making this discovery one of the most important in particle physics in the latest years [89, 90]. The Large Hadron Collider beauty experiment (LHCb) [91] focuses on flavor physics with a specific interest in indirect evidence of CP violation and rare decays of beauty and charm hadrons.

ALICE [92] was designed for the study of heavy-ion collisions. ALICE is optimized for the study of very high particle densities produced during heavy-ion collisions. It has high granularity and it is designed to measure charged particle multiplicity up to $\mathrm{dN_{ch}/dy} \approx 8000$. As the analysis presented here is performed with the ALICE detector, more detailed information is provided in Section 3.2

3.2 ALICE detector

The ALICE detector (Figure 3.2) is composed of several detectors subsystems. They can be separated, according to their location, in different categories: central barrel detectors, the muon spectrometer, and the forward detectors.

The central barrel covers mid-rapidity ($|\eta| < 0.9$) over the full azimuth and consists of: an Inner tracking system (ITS), a Time Projection Chamber (TPC) as the main tracking device of the experiment, a Time Of Flight (TOF) detector. All detectors in the central barrel are operated inside the L3 solenoidal magnet which generates a magnetic field of up to 0.5 T. A Cosmic Ray DEtector (ACORDE) is used to trigger on cosmic rays and is located at the top of the L3 magnet. The central barrel also has detector covering smaller rapidity regions *e.g.*, the High Momentum Particle Identification Detector (HMPID), a Transition Radiation Detector (TRD), a Photon Spectrometer (PHOS) and an ElectroMagnetic CALorimeter (EMCAL).

The Muon Spectrometer covers the pseudo-rapidity region $-4.0 < |\eta| < -2.4$ and is mainly focused on the measurement of quarkonia, heavy-flavor muons, light-flavor mesons and gauge bosons via their muon decay. The detectors located at forward rapidity like the Photon Multiplicity Detector (PMD) and the Forward Multiplicity Detector (FMD) are dedicated to the measurement of photons and charged particle multiplicities at large rapidity ($|\eta| \approx 3$), respectively. T0 provides the starting time of the interactions. The centrality in Pb–Pb collisions is measured with both the V0 and the Zero Degree Calorimeter (ZDC) (see Section 3.5). Besides, the V0 is also used for triggering and for the determination of the event plane in Pb–Pb collisions.

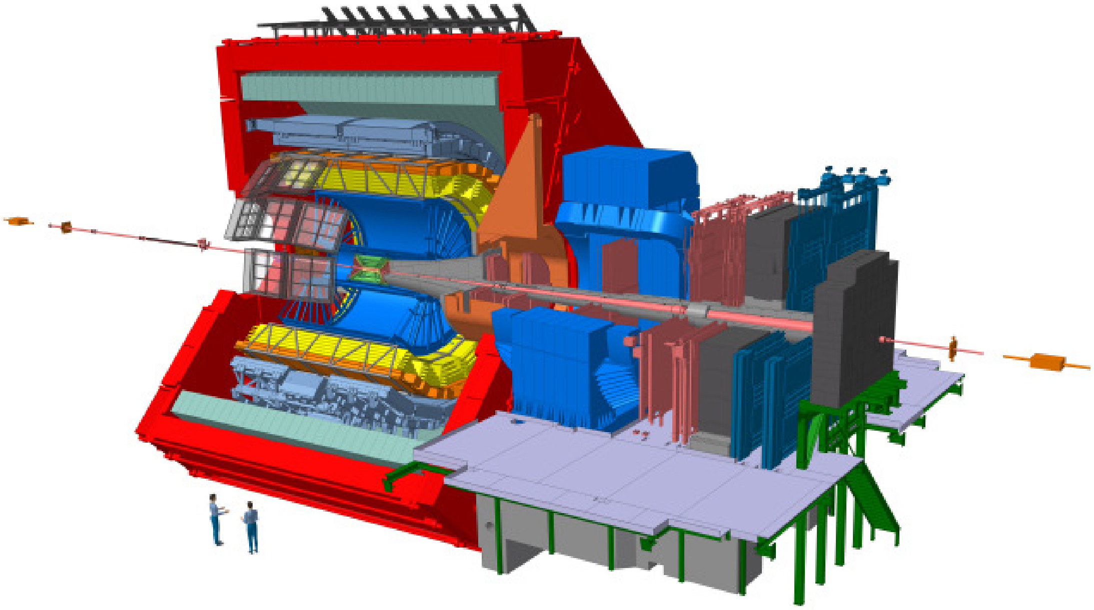

Figure 3.2: ALICE detector schematic view. Figure taken from [93].

ALICE coordinate system

The global ALICE coordinate system [94] is a right-handed orthogonal Cartesian system with the origin located at the LHC beam interaction point. The z-axis is parallel to the LHC beam axis pointing to the opposite side of the muon arm (A-side), the negative side corresponds to the C side. The y-axis is vertical and points upwards, while the horizontal x-axis points to the center of the LHC.

VZERO

VZERO [95] is a detector consisting of two circular arrays of scintillators, V0A and V0C, located asymmetrically on either side of the nominal ALICE interaction point. V0A is located at 330 cm from the interaction point on the opposite side to the muon spectrometer while V0C is located at 90 cm from the interaction point in front of the hadron absorber. Each of the V0 arrays is composed of 32 counters distributed in four rings in the radial direction. The pseudo-rapidity regions $2.8 < \eta < 5.1$ and $-3.7 < \eta < -1.7$ are covered by the V0A and the V0C respectively.

One of the main functions of the V0 detector is to provide the MB trigger (see Section 1.4) in all collision systems pp, p-Pb and Pb–Pb. The ALICE MB trigger requires a coincidence between both V0 detectors. In addition, the centrality of the collisions can be determined based on the the measured event multiplicity. The centrality selection is explained in Section 3.5.

Another important function of the V0 is the background rejection. Background in the collision comes from interactions between the beams and the residual gas within the beam pipe or interactions between the beam halo and components of the accelerator such as collimators. The particles produced by the beam-beam interaction can be distinguished from the particles produced by the beam-gas or beam-halo background using the relative arrival time of particles at both V0 detectors.

In addition, the V0 provides the integrated luminosity, which can be evaluated via

$$L_{\text{int}} = \frac{N_{\text{V0AND}}}{\sigma_{\text{V0AND}}} \tag{3.1}$$

where N_{V0AND} corresponds to the number of minimum-bias triggered events and the cross section σ_{V0AND} is extracted via the van der Meer scan analysis [2].

Inner Tracking System: ITS

The ITS [97] is the detector located closest to the beam axis. Its main purposes are the primary vertex reconstruction with a resolution $> 100\ \mu$m, tracking and particle identification (PID). The ITS consists of 6 cylindrical layers as shown in Figure 3.3. The ITS layers cover the pseudo-rapidity range $|\eta| < 0.9$ for vertexes located within $z = \pm 60$ mm with respect to the nominal interaction point [98]. The first layer has a more extended pseudo-rapidity coverage ($|\eta| < 1.98$) due to its proximity to the beam pipe ($r = 39$ mm). The first two layers are Silicon Pixel Detectors (SPD); these two layers achieve great precision in the determination of distance of closest approach to the primary vertex for charged particles. The two middle layers are Silicon Drift Detectors (SDD), and the two outermost layers are Silicon Strip Detectors. These latter four layers also measure the specific energy loss ($\mathrm{d}E/\mathrm{d}x$) of charged particles in the silicon.

The ITS measurement of the $\mathrm{d}E/\mathrm{d}x$ allows to identify particles in the low momentum region ($p \lesssim 0.7$ GeV/c). The energy loss fluctuation effects are reduced by applying a truncated mean method in order to estimate the $\mathrm{d}E/\mathrm{d}x$ value. The expected energy loss in the ITS is calculated using a hybrid parametrization of the Bethe-Bloch function [97] .

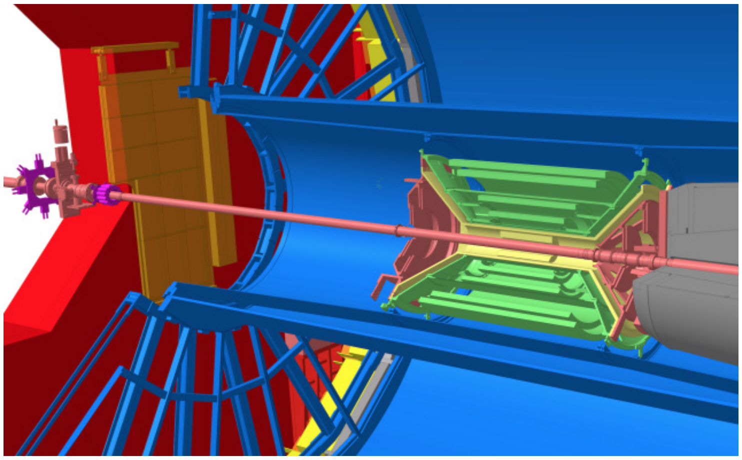

Figure 3.3: Schematic design of the ITS layers. Figure taken from [93].

Time Projection Chamber: TPC

The TPC [99] is the main tracking and PID detector of the central barrel, covering an azimuthal angle of 2π and $|\eta| < 0.9$ [3]. The TPC (see Figure 3.4) is a cylindrical detector with an inner radius of about 85 cm, an outer radius

---

[2] The van der Meer method was pioneered by Simon van der Meer [96] to measure luminosity in CERN's Intersecting Storage Ring. The technique has also been used by the LHC experiments and consists in scanning the beams across each other. The size and the shape of the interaction region are measured by recording their relative interaction rates as a function of the transverse beam separation, which allows determining the head-on rate.

[3] The pseudo-rapidity coverage corresponds to tracks with full radial length. However, the TPC can cover up to $|\eta| < 1.5$ for tracks with 1/3 of the full radial length.

of about 247 cm and an overall length along the beam direction of 500 cm.

During LHC Run1 the TPC was filled in with two different gas mixtures: in 2009 and 2010 Ne-CO_2-N_2 (90/10/5) was used and Ne-CO_2 (90-10) from 2011 on.

For the LHC Run 2 in 2015 the TPC gas mixture was changed to to Ar-CO_2 (88-12) in order to improve the operational stability, which turned out to be excellent, even at high luminosities. However, in LHC Run 2, local space charge distortions up to a few centimeters were observed. This magnitude exceeded the extrapolation from neon to argon by a factor 10 to 20 [100]. A brief discussion on these distortions and the correction procedure will be presented in Section 3.4.

If a charged particle crosses the TPC volume, it ionizes gas atoms and molecules along its trajectory and consequently deposits a specific amount of energy ($\mathrm{d}E/\mathrm{d}x$) in the gas of the TPC. The amount of energy loss depends on the velocity ($\beta\gamma = p/m$) of the particle, where β is the velocity and γ is the Lorentz factor. The field cage, with a central high voltage (100 kV) electrode located at $z = 0$, defines a uniform electric field (see Figure 3.4) parallel to the beam axis. The electric field make the released electrons drift from the creation point towards the endplates on either side of the TPC with a maximum drift time of 94 μs [101].

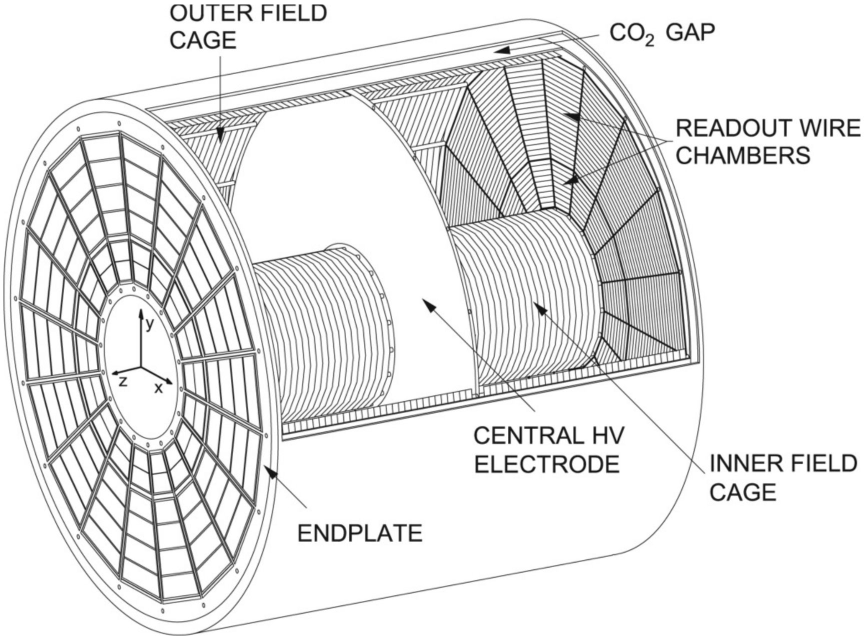

Figure 3.4: Schematic layout of the Time Projection Chamber. Figure taken from [102].

The TPC end-plates are each segmented into 18 trapezoidal sectors and equipped with multi-wire proportional chambers with cathode-pad readout. Each sector is segmented radially in two chambers: an Inner Read-Out Chamber (IROC) and an Outer Read-Out Chamber (OROC) with varying pad sizes, optimized for the radial dependence of the track density.

The TPC allows the tridimensional reconstruction of the tracks produced by the incident charged particles. The pads provide the reconstruction of the coordinates (x, y) via the distribution of the induced signal. The position of the particle in the z direction is obtained with the measurement of the time (Δt) that takes to the electron to reach the readout planes. The drift velocity of the electrons (v_e) in the gas is calibrated. The z-coordinate is then calculated with $z = v_e \Delta t$. Such three dimensional signal is called a cluster.

Particle Identification with the TPC

The identification of charged particles crossing the TPC can be performed due to the simultaneous measurements of the particles momentum and its specific energy loss by ionization ($\mathrm{d}E/\mathrm{d}x$). The momentum and the charge sign are calculated from the particle trajectory inside the magnetic field. The $\mathrm{d}E/\mathrm{d}x$ is estimated from the charge measurements along the charged particle trajectory. There are a total of 159 pad rows radially and dE/dx is measured independently in each of them, via the maximal charge of the corresponding clusters.

A truncated mean method of the maximal total charge distribution associated with the clusters of a track is applied. The average truncated mean energy loss (TPC-dE/dx) values can be parametrized with a Bethe-Bloch-like curve used previously in the ALEPH experiment [4], in the following way:

$$f(\beta\gamma) = \frac{P_1}{\beta^{P_4}}\left(P_2 - \beta^{P_4} - \ln(P_3 + \frac{1}{(\beta\gamma)^{P_5}})\right). \tag{3.2}$$

Here the parameters P_i depend on the data sample used and are provided centrally by the ALICE experiment.

Figure 3.5 shows the TPC-dE/dx as a function of the momentum for all charged particles. The solid lines represent the Bethe-Bloch parametrization for the different species: electrons, pions, kaons, protons, deuterium, tritium and ^{3}He.

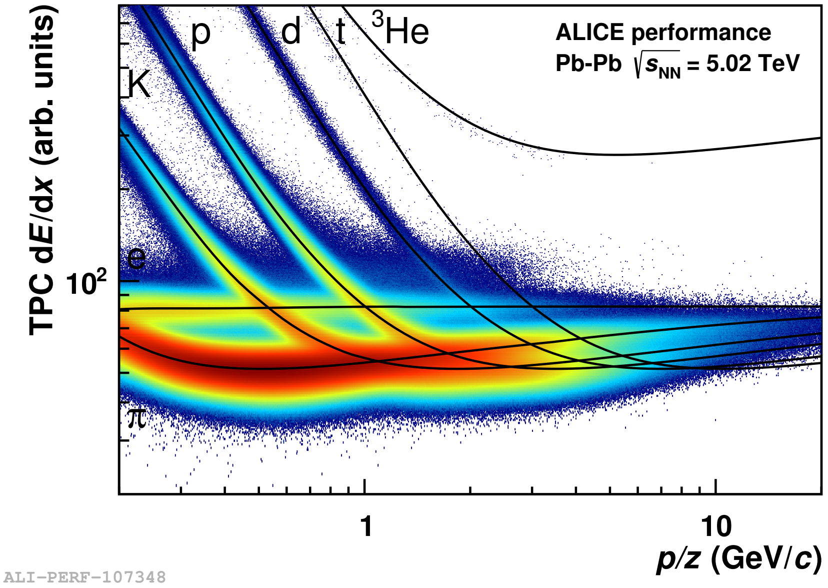

Figure 3.5: TPC-dE/dx distribution as a function of momentum for charged particles in Pb-Pb collisions at $\sqrt{s_{NN}} = 5.02$ TeV. The solid lines correspond to the calculated value of the Bethe-Bloch parametrization. Figure taken from [103].

Transition Radiation Detector: TRD

The TRD is used for electron identification in the central pseudo-rapidity region ($|\eta| < 0.84$) and also provides a trigger on high p_T electrons and jets. The TRD [104] consists of 522 chambers arranged in six layers located between the TPC and the TOF detectors at a radial distance from 2.90 m to 3.68 m from the beam axis. Each chamber consists of ≈ 5.0 cm of a radiator followed by a drift region of 3.0 cm and MWPC filled with Xe-CO$_2$. The electrons are distinguished from other charged particles due to the transition radiation produced by the first ones. A schematic example of an electron and a pion passing through the TRD chamber is shown in Figure 3.6.

---

[4] ALEPH was one of the experiments in the Large Electron Positron collider (LEP) that ran at CERN during the period 1989-2000.

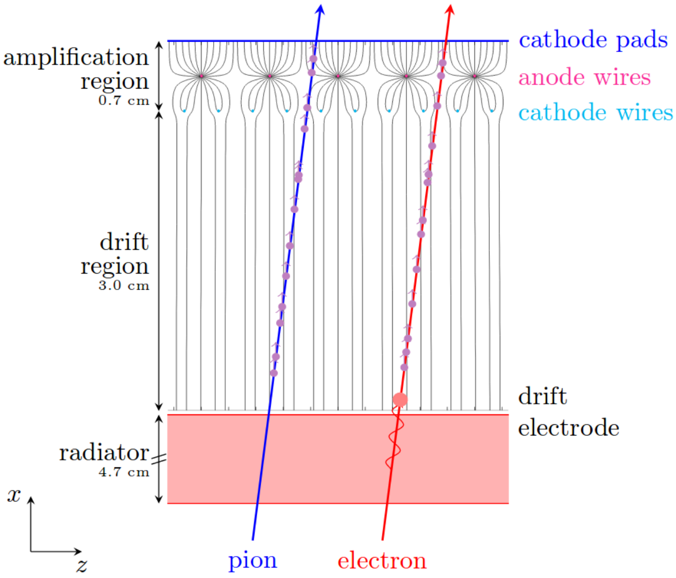

Figure 3.6: Schematic of TRD chamber with a pion and one electron track. The transition radiation produced by the electron deposits energy in the drift region indicated as a red point in the figure. Figure taken from [104].

Time Of Flight: TOF

The TOF [105] detector has a fundamental role for the PID of electrons, pions, kaons and protons in ALICE. It covers the central region of pseudo-rapidity ($|\eta| < 0.9$) and a full azimuthal angle of 2π. The TOF detector is mounted on a cylindrical structure with an inner radius of 370 cm and an external radius of 399 cm, and the barrel length is around 745 cm. The TOF detector is composed of 18 azimuthal sectors; each sector is divided into five modules along the beam direction. The TOF detector provides the information on the particle identity by measuring its velocity ($\beta = v/c$) of the particles. Figure 3.7 shows the velocity as a function of the momentum of the particles. The effective separation can be extended up to 2.5 GeV/c for pions and kaons and up to 5 GeV/c for protons. The overall time resolution in Pb–Pb collisions (0-70% centrality) is 80 ps for pions with a momentum of 1 GeV/c.

Zero Degree Calorimeter: ZDC

The ZDC [106] components are located at a distance $z = \pm 116$ m from the nominal interaction point, along the beam line. The ZDC detectors measure the energy deposited by particles (spectators) reaching the device in order to characterize the collisions and to estimate the centrality of the collision (see Section 3.5). Due to the dipole and quadrupole magnets of the LHC, protons and neutrons are detected separately. The neutrons move at zero degrees relative to the beam axis and are detected by the neutron calorimeters (ZN), while protons are detected by two protons calorimeters (ZP) displaced from the LHC beam pipe. Complementary electromagnetic calorimeters (ZEM) are located at $z = \pm 7$ m and are also used to tag hadronic interactions. Details of the measurements during LHC Run 1 can be found in [107].

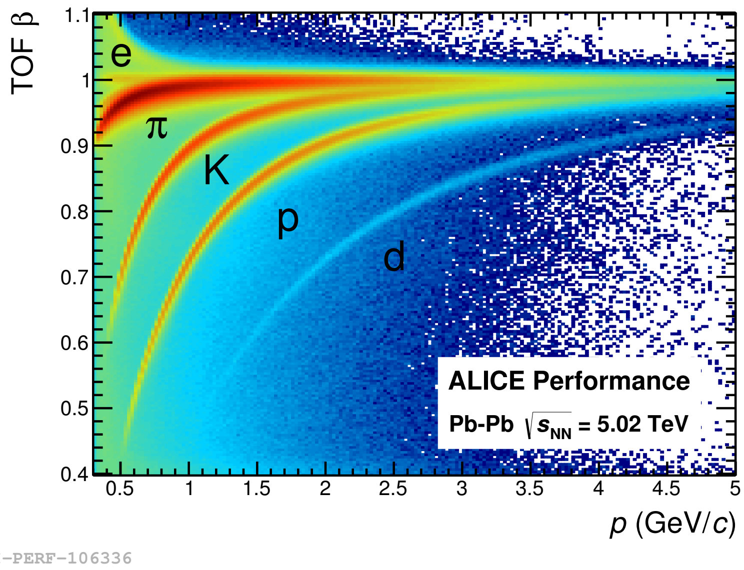

Figure 3.7: Velocity distribution measured by the TOF detector as a function of momentum for charged particles in Pb–Pb collisions at $\sqrt{s_{\mathrm{NN}}} = 5.02$ TeV. Figure taken from [103].

3.3 The ALICE environment framework: Aliroot

Aliroot is the analysis-framework used in the ALICE collaboration and is based on ROOT [108]. ROOT is a framework based in C++, developed for data analysis. ROOT provides a large set of software tools to perform different kinds of data analysis. Aliroot contains several functionalities in order to perform simulations, reconstruct and analyze the data. In case of simulations, different event generators (*e.g.* Pythia [109], HIJING [110, 111]) are used in order to produce the particles. The generators provide all the kinematics and particle identification information. The interactions between the particles and the detector are described by the transport codes such as GEANT3 [109] and GEANT4 [112].

HIJING

HIJING [110, 111] (Heavy-Ion Jet Interaction Generator) is a Monte Carlo event generator used to study hadron production in high energy nucleus-nucleus collisions. HIJING is a combined two-component model: the mini jet's production is based on pQCD calculations, while the soft interactions in the non-perturbative regime are based on the Lund string model [113]. HIJING assumes that a nucleus-nucleus collision can be decomposed into binary nucleon-nucleon collisions involving the wounded nucleons. HIJING also incorporates the nuclear modification of the parton distribution functions [114] (gluon shadowing) and jet quenching via final state jet-medium interactions. HIJING simulated events are used in this work to compute reconstruction efficiencies (see Section 4.6).

GEANT

GEANT 3 [109] (GEometry ANd Tracking) is a transport code, which describes the passage of particles through mater. The software involves the detector geometry, material, size and location. In addition, GEANT simulates the transport of particles through the detectors and all physics phenomena such as electromagnetic, hadronic and optical processes. All detector conditions (e.g. the polarity of the magnetic field) and materials are included in the simulations. GEANT is implemented in the Aliroot framework. The detector response and particles trajectories are stored as data, providing visualization of the detectors and tracks. The MC simulations used in this work were transported with GEANT 3. GEANT 4 [112] is as well available and detailed studies performed in ALICE show no differences between the two versions concerning the analysis presented here.

3.4 Track reconstruction in the central barrel

The track reconstruction in ALICE is performed using the Kalman filter approach [115], which is a robust method for statistical estimations and predictions. The Kalman Filter can be used for both track finding and track fitting simultaneously, and also provides a natural way to find extrapolation of a track from one measuring layer to another.

The reconstruction starts with the cluster finding [5] in all the central barrel detectors. A sketch with the reconstruction steps is shown in Figure 3.8. The first step consists in finding the preliminary primary vertex with the two SPD layers. The preliminary primary event vertex is defined as the point where the largest number of tracklets [6] converge. If no point is found (mainly in low multiplicity events), a one-dimensional search in the z distribution of the points of closest approach of tracklets to the nominal beam axis is performed.

Afterward, starting at the outer radius of the TPC, where the density of clusters is lower, track seeds are built with two TPC clusters and the preliminary vertex point. Then three clusters and no constraint on the vertex are used. The seeds are propagated inwards, updating at each step with the nearest cluster, to the inner wall of the TPC. Clusters can be reused by different seeds, which could lead to reconstruction of the same track several times. The algorithm searches for tracks with a fraction of shared clusters exceeding a limit between 25 and 50% [116], rejecting the worse of the two, based on several parameters like the number of clusters, momentum and cluster density. A minimum of 20 TPC clusters and more than half of the clusters expected for a given track are required in order to accept the track. Preliminary particle identification is performed using specific energy loss in the TPC gas. The accepted track candidates are found and then propagated to the outermost ITS-layer (ITSout). The seeds are extended to the innermost point of the ITS (ITSin), updated at each ITS layer. Finally, the TPC tracks are assigned to the ITS. The ITS stand-alone reconstruction is applied to the rest of ITS clusters, that did not match any track, in order to recover the tracks that were not reconstructed in the TPC due to the dead zones between the TPC sectors or the momentum cut-off [7]. Once the ITS reconstruction is complete, the tracks are extrapolated to their point of closest approach to the preliminary primary vertex.

The tracking is restarted from the point of closest approach to the primary vertex back to the outer layers of the ITS, and then repeated towards the outer wall of the TPC (TPCout). During this process, the tracks are refitted by the Kalman filter using the cluster information at each step. For the tracks labeled by the ITS tracker as potentially primary, several particle mass-dependent time-of-flight hypotheses are calculated. These hypotheses are useful for the particle identification method with TOF detector. When the track reconstruction reaches the outer wall of the TPC again, the precision of the track parameters is sufficient to propagate the track to the TRD and match it with a TRD tracklet [8] in each of the six TRD layers. The same procedure is then performed with the TOF clusters. The track is then propagated to other detectors like EMCAL, HMPID. Only the TPC and ITS detector information are used to update the track kinematics. The information from the detectors is stored in the track object to use it for PID.

The last step is a refit (TPC and ITS refit) procedure backward to the point of closest approach to the preliminary primary vertex. The event primary vertex is newly determined using the global reconstructed tracks with higher precision than with the SPD tracklets alone.

Finally, a search for photon conversions and secondary vertexes from decays of strange hadrons like K^0_S is performed to conclude the central barrel tracking. Details on the procedure can be found in [116]. The reconstructed tracks, the PID information from the detectors and particle decays are stored for each event. Such objects are known as Event Summary Data (ESDs). The ESDs contain all the information necessary for the analysis.

---

[5] *Cluster*: This is a set of adjacent (in space or in time) digits that were presumably generated by the same particle crossing the sensitive element of the detector.

[6] *Tracklets*: Lines defined by the link between two clusters in the different SPD layers.

[7] The cutoff corresponds to ≈ 200 MeV/c for pions and ≈ 400 MeV/c for protons.

[8] Track segment within a TRD layer.

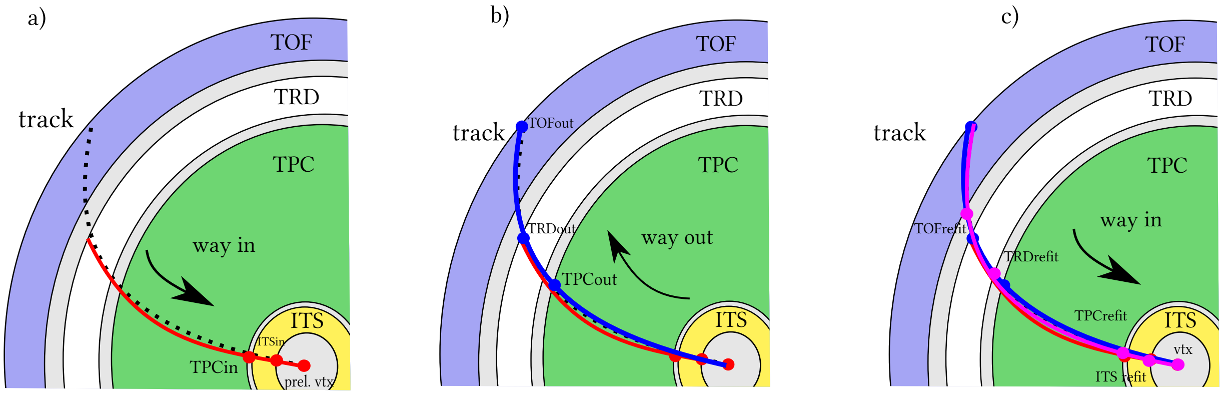

Figure 3.8: Kalman Filter reconstruction steps: *a*) After the cluster reconstruction in each detector, track candidates are obtained starting at the outer radius of the TPC. *b*) Matching of the track-candidate obtained with ITS-TPC to TRD and TOF detectors. *c*) Final Kalman filter step (ITS-TPC refit) inwards to the event primary vertex. More details are given in the text.

Summary concerning the TPC distortions during LHC Run 2

In this section, a summary concerning the space point distortions is presented. Details concerning the distortions measurement, calibration and corrections can be found in Ref. [100].

As mentioned in Section 3.2, the TPC gas mixture was changed to Ar-CO_2 (88-12) for the start of LHC Run 2 in 2015. Due to the gas properties of the Ar and Ne mixture present in the drift volume of the TPC, minor spatial distortions due to primary ionization and ion mobility can be observed. However, during LHC Run 2, the spatial distortions reach up to several centimeters (see Figure 3.9). This represents 10-20 times more compared to the distortions of millimeters observed during LHC Run 1. The distortions are caused by the space charge at the sector boundaries of some of the IROCs in the TPC. In order to correct the distortions observed in the TPC, the tracking information of the ITS, and TRD detectors is used. The ITS and TRD tracking information is not affected by the space charges.

The procedure to correct for the distortions consists in comparing the measured TPC clusters with the expected position from tracks matched to ITS in the inner radius and to TRD on the outer radius (see Figure 3.9). A Kalman filter procedure is used to propagate the points backward from TRD to ITS using only the information from these two detectors (red dots). Then, the tracks are extrapolated from larger and smaller radial position to the radial position of each TPC pad-row, and the weighted average of their position (green dots) is considered to be the position of the true (non-distorted) track at the pad-row. The residuals in the TPC sector Y ($\delta y = \Delta Y - \Delta X \tan(\phi)$) and Z ($\delta z = \Delta Z - \Delta X \tan(\lambda)$) [9] coordinates between the reference point and the measured TPC clusters (blue dots) are stored. During the reconstruction, the coordinates of every TPC cluster is corrected according to these parameterized maps. The parametrized maps are used to correct each TPC cluster, the average distortions corrections are shown in Figure 3.10, where the distance of closest approach to the primary vertex for TPC tracks is shown. The blue points correspond to the uncorrected distributions, while the red points show the distribution after the correction is applied.

---

[9] ϕ corresponds to the angle between the track direction and the pad row, while λ represents the dip angle.

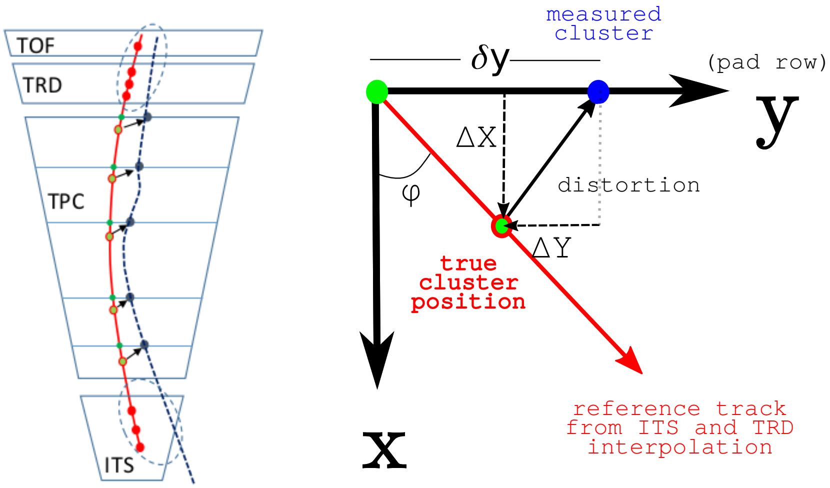

Figure 3.9: TPC sector coordinate frame, y-axis parallel to the pad rows and z-axis along the beamline. ITS, TRD and TOF clusters (red) with the corresponding expected track on the TPC. TPC measured clusters (blue). Figure adapted from [100].

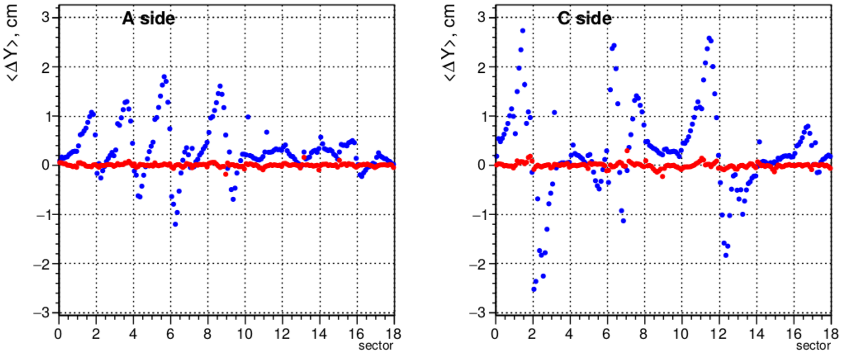

Figure 3.10: Mean distance of closest approach for TPC tracks with $p_T > 2$ GeV/c as a function of the track azimuthal position (TPC sectors).Distributions obtained with Pb–Pb data taken at an interaction rate of 4.5 kHz. Distortions before correction are shown in blue. The corrected points are shown in red. Figure taken from from [100].

3.5 Centrality determination

A brief introduction to the centrality and relevant variables in heavy-ion collisions *e.g.* the impact parameter (b), the number of participants ($N_{\rm part}$) and the number of binary collisions ($N_{\rm coll}$), were presented in Section 1.4. This section explains the method to determine the centrality in ALICE, since the impact parameter (b) of heavy-ion collisions can not be directly measured. More details can be found in Refs. [117, 118]. The centrality percentile estimation in ALICE is based on different methods. The main estimator is based on the VZERO detector information. The method based in measuring the energy deposited into the ZERO Degree Calorimeters (ZDC) is used as a cross-check.

The centrality (c) (see Eq. 3.3) is expressed as the percentile of the hadronic cross section corresponding to a particle multiplicity measured by the V0 detectors above a given threshold (N_{ch}^{THR}) or an energy deposited in the ZDC detectors (E_{ZDC}^{THR}) below a given value in the ZDC energy distribution (dE'_{ZDC}),

$$c \approx \frac{1}{\sigma_{AA}} \int_{N_{ch}^{thr}}^{\infty} \frac{\mathrm{d}\sigma}{\mathrm{d}N'_{ch}} \approx \frac{1}{\sigma_{AA}} \int_{0}^{E_{ZDC}^{THR}} \frac{\mathrm{d}\sigma}{\mathrm{d}E'_{ZDC}} \mathrm{d}E'_{ZDC}. \tag{3.3}$$

The method used to compute the centrality relies on fitting the summed amplitude of the V0 detectors with a Monte Carlo Glauber model. The fit is restricted to the region where the contamination due to electromagnetic processes is negligible [10] allowing to measure centralities up to 90%. The most central collisions (centrality $\approx 0\%$) are considered as the ones with small impact parameter, while the most peripheral collisions (centrality $\approx 90\%$) correspond to collisions with large impact parameter.

To produce the multiplicity distribution, the Monte Carlo Glauber model is coupled to a simple model for particle production. More details can be found in [117, 121]. The model parametrizes the number of emitting sources particles as $f \cdot N_{\mathrm{part}} + (1-f) \cdot N_{\mathrm{coll}}$. This is motivated by the two component models where the nucleus-nucleus collisions are decomposed into soft and hard interactions. The soft interactions produce a particle multiplicity proportional to N_{part}, while the hard interactions produce a particle multiplicity proportional to N_{coll}. The emitting sources produce particles according to a Negative Binomial Distribution (NBD).

The Non-Binomial-Distribution obtained from the simulation is fitted to the V0 amplitude obtained from data as shown in Figure 3.11. The fit describes the data distribution down to the corresponding 90% of the hadronic cross section. The Glauber model parameters such as the mean number of participants ($\langle N_{\mathrm{part}} \rangle$), the mean number of binary collisions ($\langle N_{\mathrm{coll}} \rangle$) and the mean nuclear overlap function ($\langle T_{PbPb} \rangle$) for the centrality classes are obtained by selecting the same regions in the simulation.

The nuclear overlap function, T_{AA}, represents the effective nucleon luminosity of the collisions and is calculated as $T_{PbPb} = N_{coll}/\sigma_{\mathrm{NN}}^{\mathrm{inel}}$, where $\sigma_{\mathrm{NN}}^{\mathrm{inel}}$ represents the inelastic cross section. The $\sigma_{\mathrm{NN}}^{\mathrm{inel}}$ is obtained by interpolation of pp measurements at different centers-of-mass energies and cosmic rays measurements. The value used corresponds is $\sigma_{\mathrm{NN}}^{\mathrm{inel}} = 67.6 \pm 0.6$ mb [118]. Table 3.1 contains a summary of all the values, including their systematic uncertainties. The systematic uncertainties are obtained by varying the Glauber model parameters, such as the value of $\sigma_{\mathrm{NN}}^{\mathrm{inel}}$, and the parameters of the nuclear density profile [117]. The fit is repeated for all the variations.

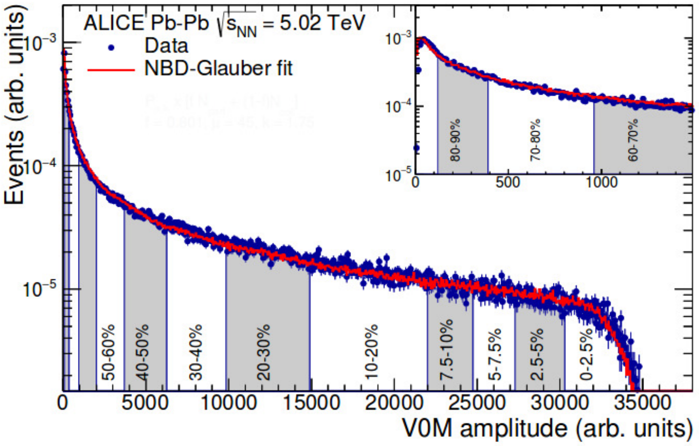

Figure 3.11: Multiplicity distribution obtained with the V0 detectors fitted with the NBD-Glauber model. The NBD-Glauber fit is shown in red and describes the data up to centralities of 90%. Figure taken from [118].

---

[10] At LHC energies, the heavy ions moving at relativistic velocity generate electromagnetic fields, leading to large cross sections for electromagnetic processes like photon-photon or photon-nucleon interactions. However, the contamination due to electromagnetic induced reactions is only observed at small multiplicities [117]. The contribution of electromagnetic background is estimated using the QED [119] and STARLIGHT [120] simulations and is found to be negligible for collisions more central than 90%.

Centrality and Glauber model variables				
Centrality (%)	$\langle N_{\mathrm{coll}} \rangle$	syst	$\langle T_{\mathrm{AA}} \rangle$ (mb^{-1})	syst (mb^{-1})
0-10	1636	170	23.4	0.78
10-20	1001	97	14.3	0.46
20-40	472.8	41	6.754	0.22
40-60	136.3	9.9	1.949	0.0081
60-90	20.83	1.2	0.2976	0.0018
0-90	435.8	4.1	6.22	0.2
0-20	1318	130	18.8	0.61
40-90	78.62	9.97	1.123	0.083

Table 3.1: Geometrical properties of Pb–Pb collisions at $\sqrt{s_{\mathrm{NN}}} = 5.02$ TeV for the different measured centralities. Values are taken from [118].

4

Measurement of inclusive J/ψ production

In the current chapter, the procedure to measure inclusive J/ψ production with the ALICE detector is described. The event selection is detailed in Section 4.1. The procedure to extract the raw J/ψ yield is explained through Sections 4.2 to 4.5. The corrections applied are listed in Section 4.6. The analysis procedure in Pb–Pb and pp collisions is similar. This chapter contains all the information related to the measurement in Pb–Pb collisions, the information concerning the measurement in pp collisions can be consulted in Appendix A. The comparison between the measurement in pp collisions and the interpolation procedure is discussed in Section 4.7. The observables measured in this analysis are presented in Section 4.8.

4.1 Data sample and event selection

The data sample used for the analysis consists of Pb–Pb and pp collisions recorded by the ALICE detector during the year 2015. The trigger condition used to select the events corresponds to V0-AND. It is defined as the ALICE minimum-bias (MB) trigger and requires the coincidence of hits in both V0A and V0C detectors. The MB trigger cross-section is measured with a van der Meer scan [122] and corresponds to $\sigma_{\rm vdM}({\rm V0}) = 4.74 \pm 0.13$ b. The full Pb–Pb data sample corresponds to an integrated luminosity of about 15 μb^{-1}. The pp data sample accounts for 100 million MB triggered events.

In addition to the MB trigger request, the event selection requires having a reconstructed primary vertex based on global tracks with at least one of them contributing to the primary vertex. To guarantee the same geometrical acceptance for all the tracks, only events with a primary vertex reconstructed within a 10 cm distance from the nominal interaction point in the z axis ($Z_{\rm vtx}$) are used for this analysis.

4.1.1 Pile-up rejection

Due to the Pb–Pb interaction rate during LHC Run 2 (0.2 and 7.8 kHz), an additional quality check on the events is performed. The data sample taken below 4.0 kHz is considered as low interaction rate, while the data sample taken above 4.0 kHz is considered as high interaction rate. Due to the TPC drift time of about 94 μs, it can occur that pile-up [1] tracks from other interactions are present in the data.

Multiplicity correlations with faster detectors have been studied in order to find possible outliers/pile-up events. Figure 4.1 shows the correlation between the multiplicity measured by the V0 detector and the number of tracks in the TPC for low interaction rate data (Left) and high interaction rate data (Right). The events for which the measured multiplicity values exhibit values outside the expectations from low interaction rate are most probably

---

[1] Several collisions recorded as one single event is considered pile-up.

affected by pile-up tracks. These outliers are observed in TPC tracks due to the long TPC drift time. The events with outlier number of TPC tracks are removed, based on a function fitted to the correlation observed in the low interaction rate runs (see Eq. 4.1) where the amount of outlier events is negligible. The amount of rejected events in the high interaction rate runs due to this selection represents 20% of the total statistics.

$$y = 1.2 \times 10^{-5}x^2 + 2.5x - 2200 \tag{4.1}$$

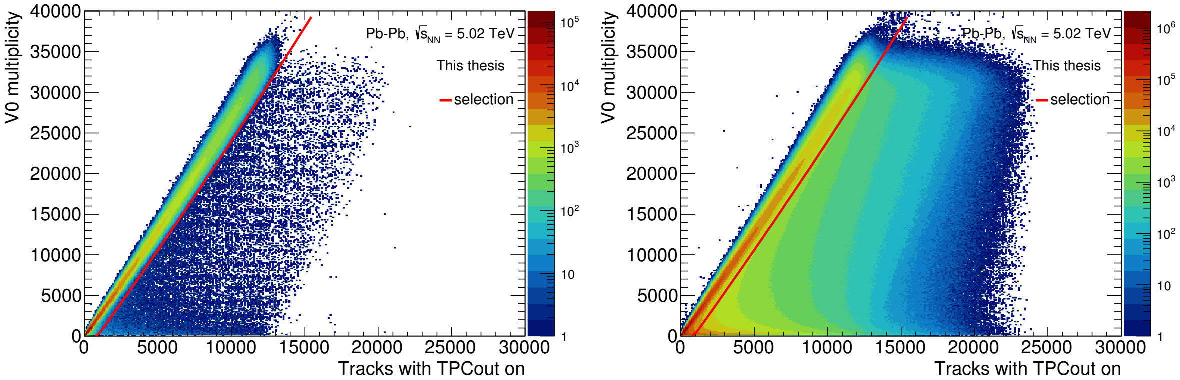

Figure 4.1: Correlation of multiplicity measured with the V0 and TPC detectors. Low interaction rate data (Left). High interaction rate data (Right).

The centrality distribution for the events after the selection explained above is shown in Figure 4.2. The total amount of analyzed events corresponds to approximately 70 million.

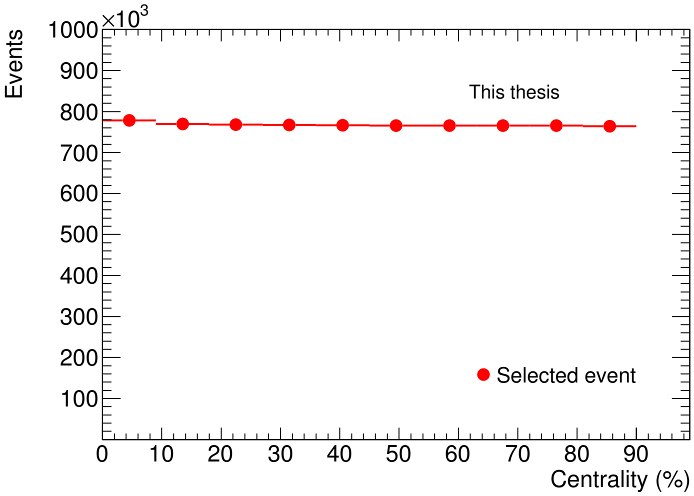

Figure 4.2: Centrality distribution of the analyzed events.

4.2 J/ψ signal reconstruction

The J/ψ decay channel ($J/\psi \rightarrow e^+e^-$) with a branching ratio equal to 5.971 ± 0.032% [8] is shown in Figure 4.3. The J/ψ signal is observed as a peak in the invariant mass distribution calculated from the electron-positron pairs [2]. The invariant mass spectrum is calculated using all possible combinations of electron pairs as:

---

[2] From now on, the reference to electrons will imply both: electron and positron, unless otherwise specified.

$$m_{12}^2 = m_1^2 + m_2^2 + 2(E_1E_2 - p_1p_2\cos\theta_{12}), \tag{4.2}$$

where θ_{12} is the angle between the electrons. The momentum and the energy of the electrons are $p_{1,2}$ and $E_{1,2}$ respectively.

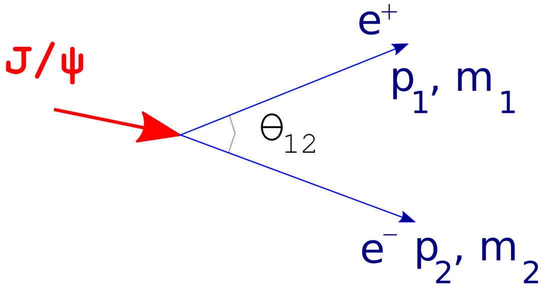

Figure 4.3: Sketch of a J/ψ di-electron decay.

4.3 Track selection

The criteria applied to select electron candidates of J/ψ decays are explained in this section. The selection takes into account the track quality level, the kinematics, and the particle identification.

4.3.1 Track quality selection

The tracks used in the analysis have to fulfill certain requirements listed in the following, in order to ensure a good reconstruction quality.

- **TPC requirements:** A track is required to have at least 70 out of 159 clusters in the TPC. The value of $TPC\chi^2/n_{cls}$ obtained in the momentum fit is required to be less than 2.5. The standard value employed in ALICE corresponds to 4, however the selection of this value is used to improve the quality and p_{T} resolution of the tracks used, mitigating effects due to the TPC distortions (see Section 3.4). A successful TPC refit and a minimum of 6 TPC segments are also required. A TPC segment is defined as an interval of 20 consecutive rows, with a track having a maximum of eight segments. A segment from a given track is assumed to be active if at least 5 clusters are found in its 20 rows [123]. As the maximum of TPC clusters possible is 159, the 8th segment can only have 19 clusters. The TPC segments requirement ensures a uniform distribution of clusters along the track. The TPC shared clusters correspond to clusters shared among more than one track. A maximum fraction of shared clusters equal to 0.3 is requested to reject fake or multiple reconstructed tracks.
- **ITS requirements:** A successful ITS refit is required for all the reconstructed tracks. That implies a minimum of two clusters out of the six possible in the silicon layers of the ITS. A $\chi^2_{ITS}/n_{cls} < 10$ and a maximum fraction of ITS shared clusters of 0.4 are required. The χ^2_{ITS}/n_{cls} selection rejects tracks originating from displaced vertexes. The fraction of shared clusters in the ITS, defined as the number of shared clusters divided by the total number of ITS clusters is used to reduce secondary tracks, particularly from photon conversions. An additional hit in any of the two innermost layers of the ITS (*SPD any*) is required.
- **Impact parameter:** A selection on the transverse (DCA_{XY}) and longitudinal (DCA_Z) distance-of-closest-approach to the primary vertex is applied for all the tracks. The selection is loose to include contributions from non-prompt J/ψ decays which have an average large decay time (see Section 2.3). The track selection is restricted to $|DCA_{XY}| < 3.0$ cm and $|DCA_Z| < 1.0$ cm.
- **Kink daughters rejection** is applied.

4.3.2 Kinematic selection

A pseudorapidity selection, $|\eta| < 0.9$, on the electron candidates of J/ψ decays is also applied. This selection is determined from the coverage of the ALICE detectors in the central barrel. Selecting the pseudo-rapidity of the electron candidates of a J/ψ decay restricts the rapidity of the J/ψ to a maximal value $|y_{\mathrm{J}/\psi}| = 0.9$. The pseudorapidity selection of electron candidates of J/ψ decays in $|\eta| < 0.8$ and $|\eta| < 0.85$ was also studied [3], since the TPC provides the highest tracking efficiency in the region $|\eta| < 0.8$. As no dependence is observed and the J/ψ analysis is limited in statistics, the full acceptance coverage is used for this analysis.

A selection of electrons candidates of J/ψ decays with $p_{\mathrm{T}} > 1$ GeV/c is applied [4]. Due to the large mass of the J/ψ, the momentum transferred to each electron is relatively large, and the J/ψ signal lost due to the momentum selection applied on the electron legs is small. As shown in Figure 3.5 several particle species cross the electron band in the low momentum region. The selection of electrons above 1 GeV/c allows excluding kaons and protons, reducing the amount of combinatorial background in the invariant mass distribution. Further removal of hadrons using particle identification is explained in the following.

4.3.3 Particle identification selection

The particle identification (PID) strategy is based on the specific energy loss measured by the TPC (see Section 3.2). The selection is based on the number of TPC sigmas ($n\sigma_{TPC}$). The $n\sigma_{TPC}$, for the particle species i, is defined as:

$$n\sigma_{\mathrm{TPC,i}} = \frac{dE/dx_{\mathrm{meas}} - \langle dE/dx_{\mathrm{exp,i}}(\beta\gamma, p_{in}, N_{clsPID}, \eta)\rangle}{\sigma_i(\beta\gamma, p_{in}, N_{clsPID}, \eta)} \tag{4.3}$$

where the term $\mathrm{d}E/\mathrm{d}x_{\mathrm{meas}}$ corresponds to the specific energy loss measured by the TPC. The second term $\mathrm{d}E/\mathrm{d}x_{\mathrm{exp},i}$ corresponds to the expected energy for the particle species i parameterized as a function of the parameters $\beta\gamma$ at the inner wall of the TPC, and the number of TPC clusters with PID information (N_{clsPID}) [5] and the η of the track [124]. The resolution is defined as: $\sigma \equiv \mathrm{dE/dx_{exp}} \cdot \sqrt{1 + \Delta_{\mathrm{cls}}/\mathrm{N_{clsPID}}}$, where Δ_{cls} corresponds to the PID resolution per single PID cluster including the dependencies mentioned before. The average resolution in the most central events (0-5%) corresponds to 6.5% [116]

TPC Nσ_e calibration

In an ideal case the $n\sigma_{\mathrm{TPC},i}$ distributions are Gaussian with a mean equal to zero and a width equal to one. However, it is found that the mean and width of the $n\sigma_{\mathrm{TPC},e}$ distribution varies with η and centrality. These variations are due to detector effects *e.g.* high occupancy in the TPC in central Pb–Pb collisions. As the signal extraction relies on a good electron identification, a calibration of the TPC-PID information is performed in order to correct these dependencies.

The calibration is performed using a pure sample of electrons from reconstructed photon conversions. The photon conversions are selected using their $V0$ decay topology ($\gamma \rightarrow e^+e^-$). The distributions of $n\sigma_{\mathrm{TPC,e}}$ obtained from the photon conversions are fitted with a Gaussian as a function of centrality and η. The parameters obtained from this fit are used to center the $n\sigma_{\mathrm{TPC,e}}$ at zero and set the width to one in 2-dimensional (η and centrality) maps. The correction maps are obtained from [125].

Electron identification

Electrons candidates of J/ψ decays are selected requiring the tracks to be within 3σ from the expected values of $|n\sigma_{\mathrm{TPC,e}}| < 3$. In addition, only tracks with an expected $n\sigma_{\mathrm{TPC,p}}$ and $n\sigma_{\mathrm{TPC},\pi}$ larger than 3.5 ($n\sigma_{\mathrm{TPC,p},\pi} > 3.5$)

---

[3] In these cases the pair acceptance is restricted in the maximal rapidity of the J/ψ $|y_{\mathrm{J}/\psi}|$ <0.8 and $|y_{\mathrm{J}/\psi}| < 0.85$, respectively.

[4] Note that the distribution shown in Figure 3.5 displays the dependence of the specific energy loss as a function of momentum and not p_{T}. As $|p| = p_T \cosh\eta$, the maximum deviation for track within $|\eta| < 0.9$ implies a factor 1.35

[5] Note that some TPC clusters may be excluded from the computation of the $\mathrm{d}E/\mathrm{d}x$, *e.g.* TPC clusters at the sector boundaries, since the calibration is not as precise as for TPC clusters away from the sector boundaries.

are taken into account for the analysis. These exclusions reduce the hadron contamination of the sample. Due to the small abundance of deuterons among the selected tracks, the contamination is neglected.

Figure 4.4 shows the electrons candidates of J/ψ decays selected as a function of the momentum on the inner wall of the TPC. The effect of requiring $n\sigma_{\mathrm{TPC,p}} > 3.5$ can be identified as the curve in momentum region below 2 GeV/c, while the effect of requiring $n\sigma_{\mathrm{TPC},\pi} > 3.5$ is observed in the high momentum region above 3 GeV/c.

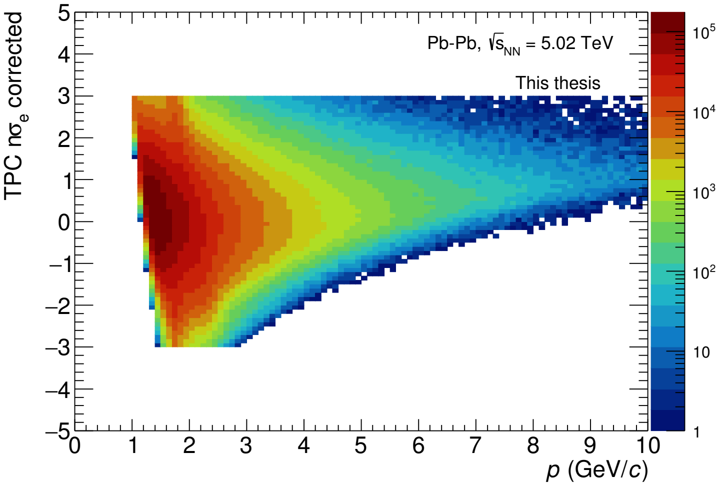

Figure 4.4: The $n\sigma_{TPC,e}$ as a function of momentum at the inner wall of the TPC (p). The $n\sigma_{TPC,e}$ is already corrected applying the calibration maps.

An additional selection is applied in tracks which form a pair compatible with an invariant mass below 50 MeV/c^2, rejecting electrons from photon conversions.

4.4 J/ψ signal extraction

The invariant mass distribution obtained with the unlike-sign (ULS) pairs of electrons after applying the selection criteria described in Section 4.3.1 is shown in Figure 4.5. The figure shows the invariant mass spectrum for the 6 different centrality classes used for the p_{T} integrated analysis: 0-10%, 10-20%, 20-40%, 40-60%, 60-90% and the sum 0-90%. The invariant mass spectrum is dominated by uncorrelated background consisting of random combination of electrons. Additional components such as electrons from open charm, open beauty hadron decays, and unidentified hadrons contribute to the background. The low invariant mass region is composed of electrons originating from Dalitz decays (π^0, ρ, η). The precise knowledge of charm and beauty quark production in Pb–Pb collisions is currently limited and a precise estimation of the different sources composing the background cannot be taken from MC simulations. Additionally, electrons produced by different photon conversions included in the background may not be perfectly described due to inaccuracies in the full detector simulation.

An accurate description of the background is essential to subtract it from the ULS distribution, which contains both the signal and background distributions. Two different techniques are commonly used in heavy-ion collisions to describe the background the *like-sign pair method* [126] and the *event mixing method* [126, 127]. Despite the unknown composition of the background,it is well described by two different methods used in this analysis. Both methods were used to estimate the background and extract the J/ψ raw signal. The procedure is explained in the following.

4.4.1 Like-sign method

The combinatorial background can be estimated using the dielectron like-sign (LS) pairs, *i.e* pairs with the same charge, either positive (N^{++}) or negative (N^{--}). The LS pairs are added either using the arithmetic mean or the

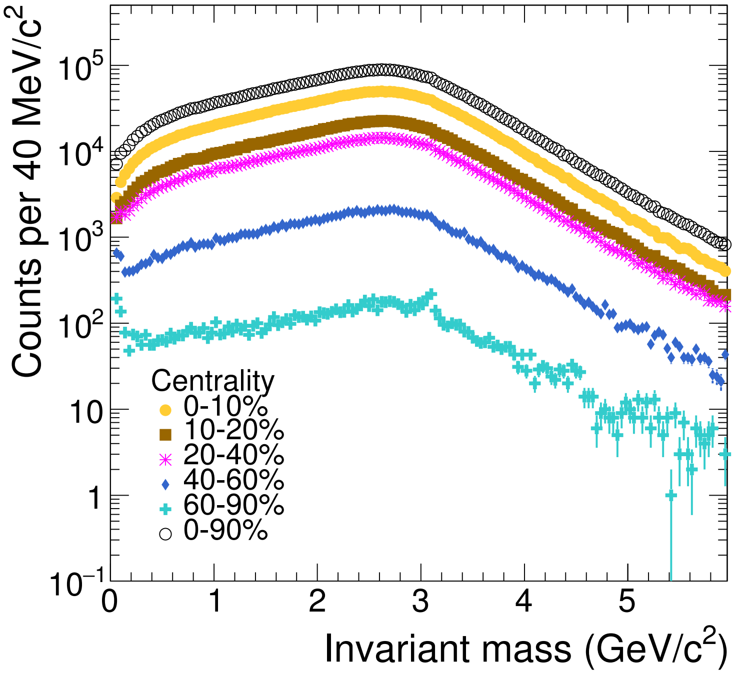

Figure 4.5: Invariant mass calculated with the unlike-sign electron pairs for different centrality classes.

geometric mean as shown in Eq. 4.4.

$$N_{LS,arith} = R \cdot (N^{++} + N^{--}), \tag{4.4a}$$

$$N_{LS,geom} = R \cdot (\sqrt{N^+N^+ \cdot N^-N^-}). \tag{4.4b}$$

An additional correction factor (R) is applied to account for possible asymmetries due to a detector acceptance bias related to the charge of the particle. The R factor is defined as:

$$R(m) = \frac{N_{+-}(m)}{\sqrt{N_{++}(m)N_{--}(m)}}, \tag{4.5}$$

and can be computed with the event mixing method described in the Section 4.4.2. The R factor obtained as a function of the invariant mass is shown in Figure 4.6. It can be observed that the R factor value is equal to unity for masses above 1 GeV/c^2. Since the R factor is compatible with unity in the region around the J/ψ mass, no R factor correction is applied in this analysis.

The yield extraction using the LS method with the geometric and arithmetic mean are performed in five centrality classes as shown in Figures 4.7 and 4.8, respectively. The Figures show the different invariant mass distributions and the signal extraction for the different centrality classes used for the $p_{\rm T}$ integrated analysis. The top panels show the ULS distribution and the background description with the LS method. The LS method describes the background satisfactorily and no scaling is needed. The bottom panels show the signal after background subtraction. The raw J/ψ signal ($N_{{\rm J}/\psi}$) is extracted by bin counting in the mass region (2.92 - 3.16 GeV/c^2) indicated by the green lines in the figure, similarly to previous ALICE measurements (Refs. [31, 83, 84, 128–130]). The total number of J/ψ's is shown in the bottom panel together with the signal over background (S/B) and the significance, defined as $\mathrm{S}/\sqrt{\mathrm{S}+2\mathrm{B}}$. The same panels show the shape of the J/ψ signal shape obtained in Monte Carlo simulations normalized to the integral in the mass region (2.92, 3.16) GeV/c^2 is shown with a continuous black line. The $\chi^2/d.o.f.$ between the normalized shape expected from MC and the data distributions is obtained in the full mass window [2.0, 3.7] GeV/c^2. A good agreement with the data is observed with values of $\chi^2/d.o.f.$ close to unity in all cases. The J/ψ signal shape shows a significant tail towards lower masses produced by energy loss of the electrons

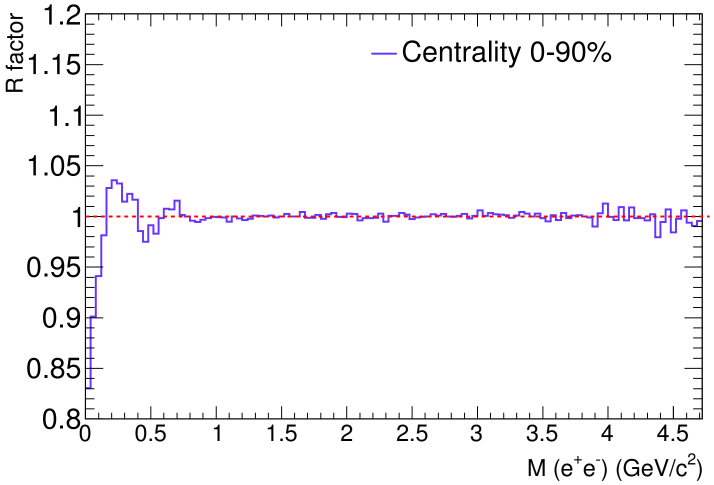

Figure 4.6: R factor correction as a function of the invariant mass.

in the material via bremsstrahlung and the radiative decay channel J/$\psi \rightarrow e^+e^-\gamma$ where the produced soft photon is not reconstructed. Additional discussion on the signal shape can be found in Section 4.6.2. A negligible difference is observed when using the geometric and arithmetic mean for the signal extraction in the LS method, the values are summarized in Table 4.1.

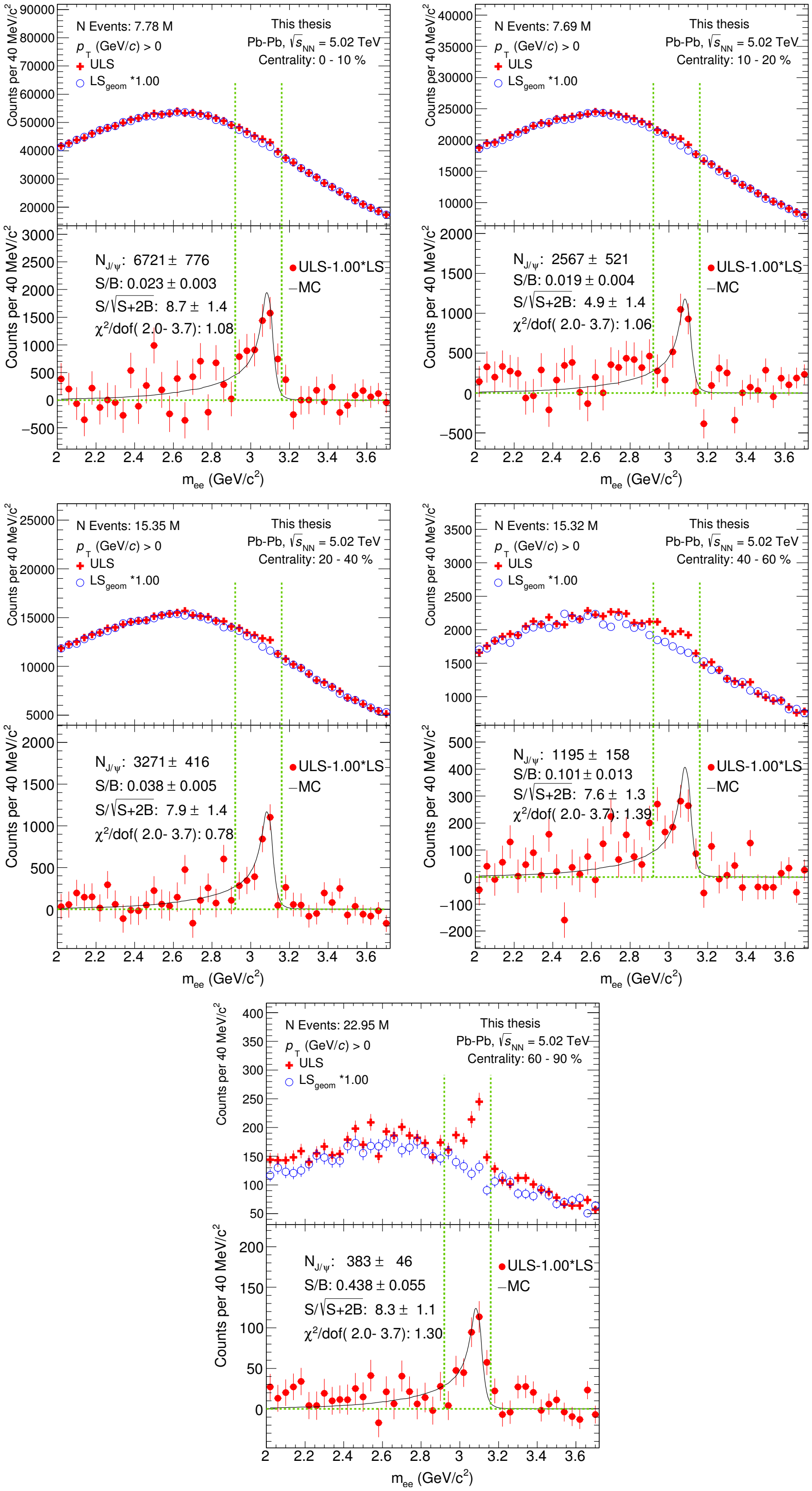

Figure 4.7: Signal extraction performed with the like-sign (LS$_{\mathrm{geom}}$) geometric method for five different centrality classes. Top left: 0-10 %, top right: 10-20 %, middle left: 20-40 %, middle right: 40-60 %, bottom: 60-90 %.

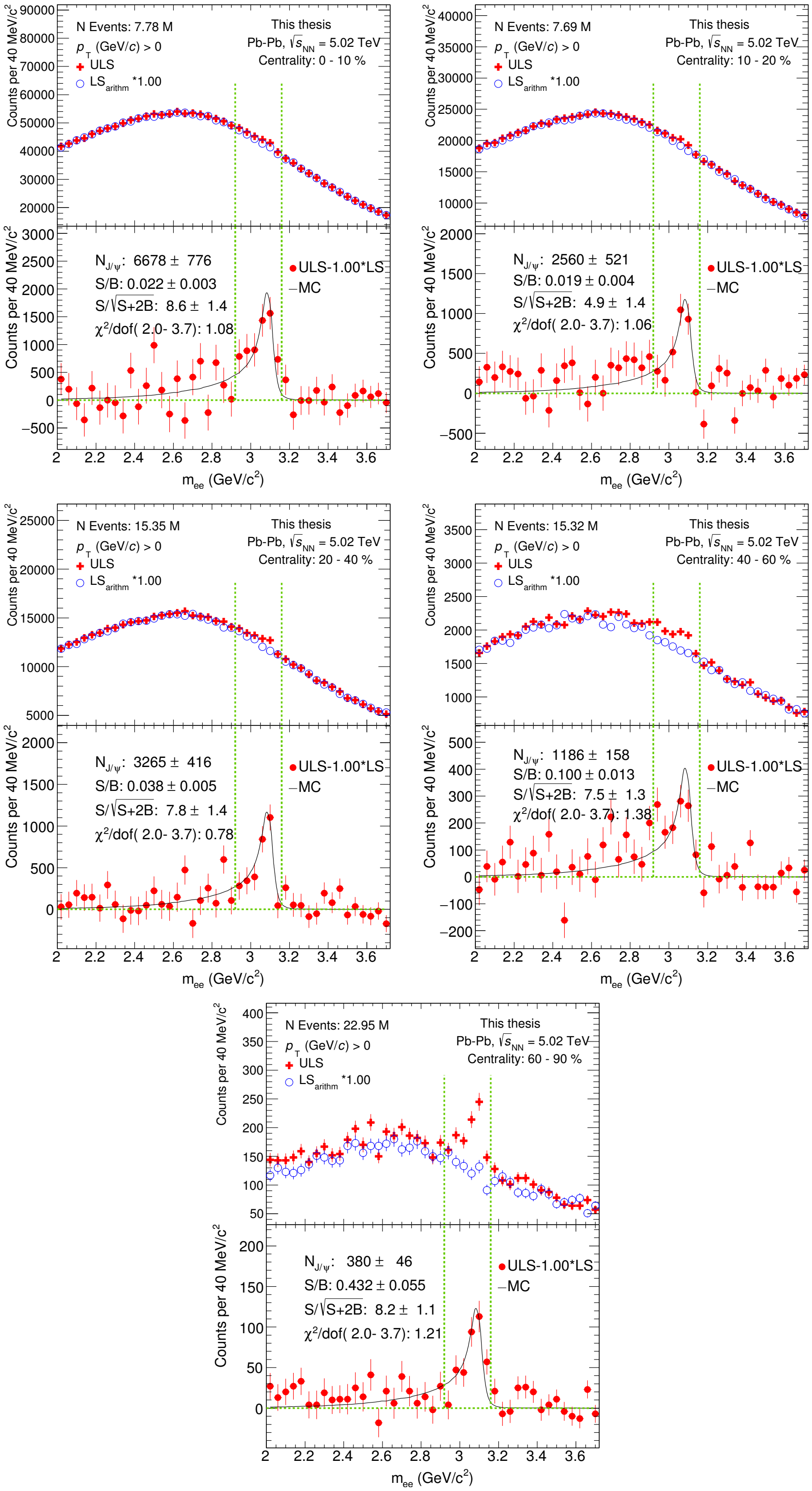

Figure 4.8: Signal extraction performed with the like-sign (LS$_{\text{arithm}}$) arithmetic method for five different centrality classes. Top left: 0-10 %, top right: 10-20 %, middle left: 20-40 %, middle right: 40-60 %, bottom: 60-90 %.

4.4.2 Event mixing method

The event mixing (EM) method consists in selecting two particles originating from two different events to calculate the invariant mass distribution. For a satisfactory background description with the event mixing method, the events selected must have similar global properties *e.g.* acceptance and multiplicity. In the presence of flow, they have to be rotated into a common reaction plane [126]. In order to ensure the similarity of the events used for the mixing, a classification based on the centrality, the longitudinal position of the primary vertex (z_{Vtx}), and the event plane angle (Ψ_2^{EP}) (see Section 1.4) are used. The different classes in z_{Vtx} account for acceptance effects, the different centralities account for track density and due to the presence of elliptic flow in heavy-ion collisions, the Ψ_2^{EP} obtained with the V0 detector is used. The event plane angle groups the events according to the orientation of the second harmonic collision symmetry plane. The statistical precision of the EM method depends on the number of events used for mixing. However, the sum of the events is not normalized. Usually, the normalization is estimated from the unlike-sign distribution, scaling the mixed event distribution in the region where the correlated signal is assumed to be negligible [126].

The different event mixing categories used for this work are:

- Centrality (%):$\{0, 5, 10, 20, 30, 40, 50, 60, 70, 80, 90\}$
- z_{Vtx} position (cm): $\{-10, -7, -4, -2, 0, 2, 4, 7, 10\}$
- Event plane angle Ψ_2^{EP} (8 bins): $[-\pi/2, \pi/2]$

Figure 4.9 shows the different invariant mass distributions and the signal extraction for the five centrality classes used for p_{T} integrated analysis. The top panels show the ULS distribution and the background description by the EM method. The EM method is scaled to match the total integral of the invariant mass entries in the region [2.0, 2.5] GeV/c^2 and [3.2, 3.7] GeV/c^2. The mass region [2.5 - 3.2] GeV/c^2 is excluded since it contains the J/ψ mass peak. The criteria to select the mass window is based first on the low mass region used for the scaling, where down to 2.0 GeV/c^2 a minimum amount of correlated pairs are present. The selection region selected is symmetric with the same size selected in the high mass region. The presence of the ψ(2S) ($\mathrm{M}_{\psi(2S)} \approx 3.7$ GeV/c^2) is safely neglected, since the expectations of di-electron pairs from the ψ(2S) are reduced by a factor 50-100 based in expectations with the observed ALICE results at forward rapidity [131]. The signal is extracted by bin counting in the region ($2.92 < m_{\mathrm{e^-e^+}} < 3.16$GeV/$c^2$) indicated within the green dashed lines. Further variations of the region used to scale the background and the signal extraction region were performed as systematic uncertainties; the procedure will be discussed in Section 5.1. The $\chi^2/d.o.f.$ between the normalized shape expected from MC and the data distributions is obtained in the full mass window [2.0, 3.7] GeV/c^2. A good agreement with the data is observed with values close to unity in all cases. The significance of the J/ψ signal in the different centralities show reasonable values $S/\sqrt{S+B} > 7$.

The number of J/ψ's and the significance obtained with the different signal extraction methods are summarized in Table 4.1. A good agreement on the J/ψ yield between the two methods can be observed, indicating that the contribution to the J/ψ signal from correlated sources is small. Due to the larger statistical uncertainties of the LS method due to the statistical uncertainty on the background, and was used as a cross-check of the measurement. The EM method is used as the standard method for the signal extraction and the determination of the final result. The possible contribution of correlated dielectron pairs after the mixed event background subtraction is included in the systematic uncertainty due to the signal extraction, where several variations on the signal extraction range and the mass scaling region of the event mixing method are used for the signal extraction. This procedure is explained in Section 5.1.

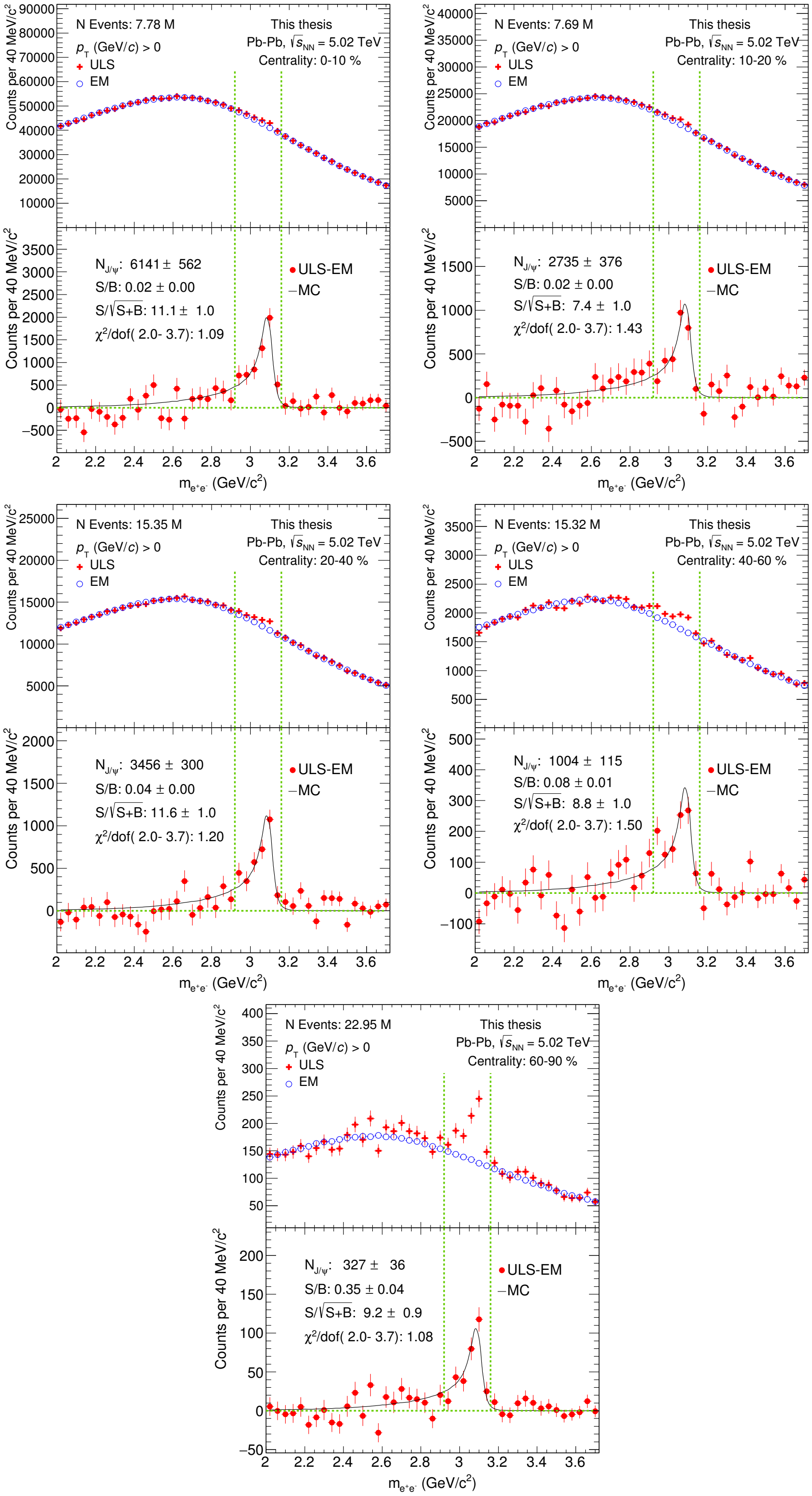

Figure 4.9: Signal extraction performed with the event mixing method for five different centrality classes. Top left: 0-10 %, top right: 10-20 %, middle left: 20-40 %, middle right: 40-60 %, bottom: 60-90 %.

Summary of the signal extraction methods						
Centrality	**LS Method**				**EM method**	
	Arithmetic mean		Geometric mean			
(%)	$N_{J/\psi}$	Significance	$N_{J/\psi}$	Significance	$N_{J/\psi}$	Significance
0-10	6678 ± 776	8.6 ± 1.4	6721 ± 776	8.7 ± 1.4	6141 ± 562	11.1 ± 1.0
10-20	2560 ± 521	4.9 ± 1.4	2657 ± 521	4.9 ± 1.4	2735 ± 376	7.4 ± 1.0
20-40	3265 ± 416	7.8 ± 1.4	3271 ± 416	7.9 ± 1.4	3456 ± 300	11.6 ± 1.0
40-60	1186 ± 158	7.5 ± 1.3	1195 ± 158	7.6 ± 1.3	1004 ± 115	8.8 ± 1.0
60-90	380 ± 46	8.2 ± 1.1	383 ± 46	8.3 ± 1.1	327 ± 36	9.2 ± 0.9

Table 4.1: Summary of the raw number of J/ψ and significance obtained with the LS (arithmetic and geometric) and EM methods in the different centrality classes.

4.5 Signal extraction in p_{T} intervals

Due to the limited statistics, the p_{T}-differential signal extraction requires to use larger centrality classes, in order to obtain reasonable significance values on the J/ψ signal extraction. The centrality classes $0-20\%$, 20-40%, 40-90% and the sum 0-90% allow having enough statistics to extract the J/ψ signal with a significance $(S/\sqrt{S+B}) > 4$. The signal extraction is performed in four different p_{T} intervals: $0.15-1.5$, $1.5-3.0$, $3.0-5.0$, $5.0-10.0$ GeV/c. The minimum p_{T} requirement of 150 MeV/c allows to exclude the potential J/ψ coherent photoproduction component introduced in Section 2.7. The signal extraction in the p_{T} region below 150 MeV/c in the most peripheral events (40-90%) is also performed. This p_{T} interval in the case of the most central events is not computed due to the low significance of the signal in those 2 cases. Figures 4.10 to 4.13 show the p_{T}-dependence of the signal extraction performed in the different centralities. Analogous to the previous section, the bottom panels contain the J/ψ raw yield, the S/B and the significance values after the EM background is subtracted in each p_{T} interval.

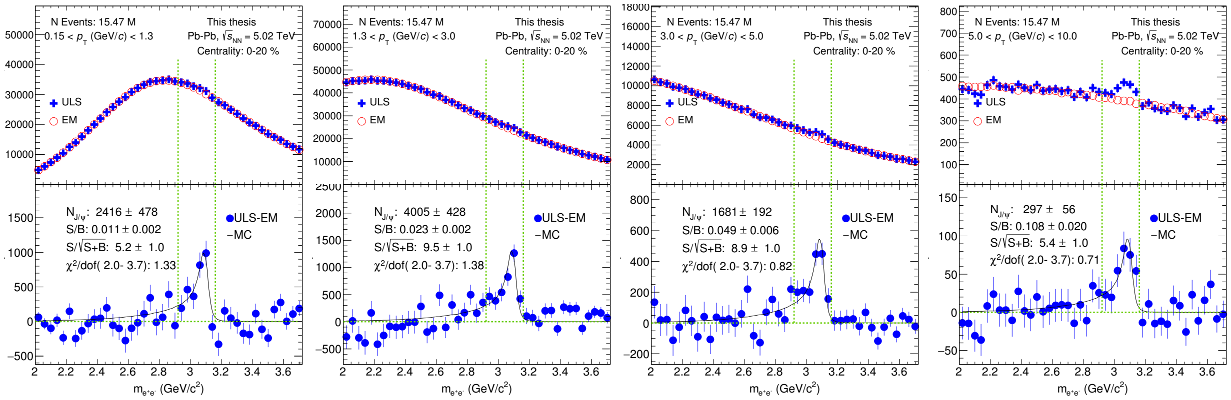

Figure 4.10: Signal extraction performed with the event-mixing method for the four different p_{T} intervals in the centrality class 0-20%. The p_{T} interval is indicated in each panel.

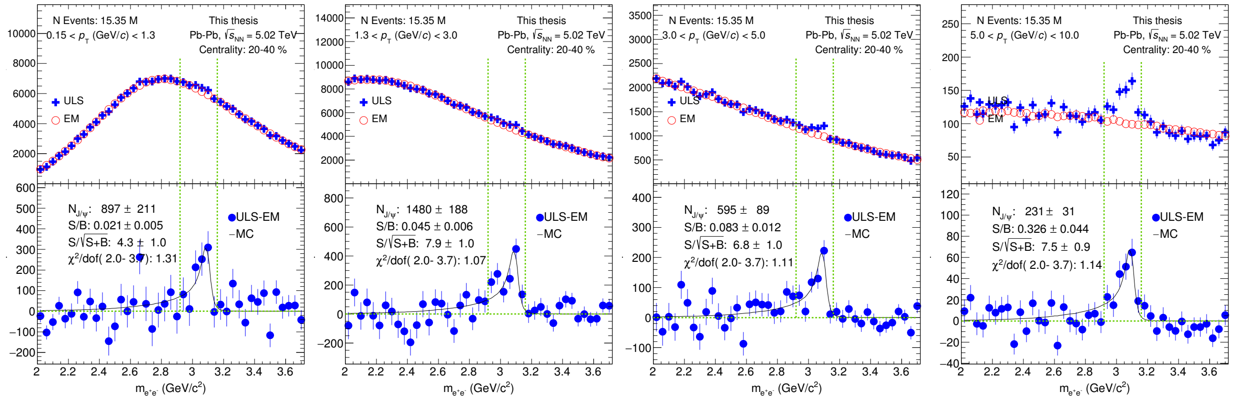

Figure 4.11: Signal extraction performed with the event-mixing method for the four different p_{T} intervals in the centrality class 20-40%. The p_{T} interval is indicated in each panel.

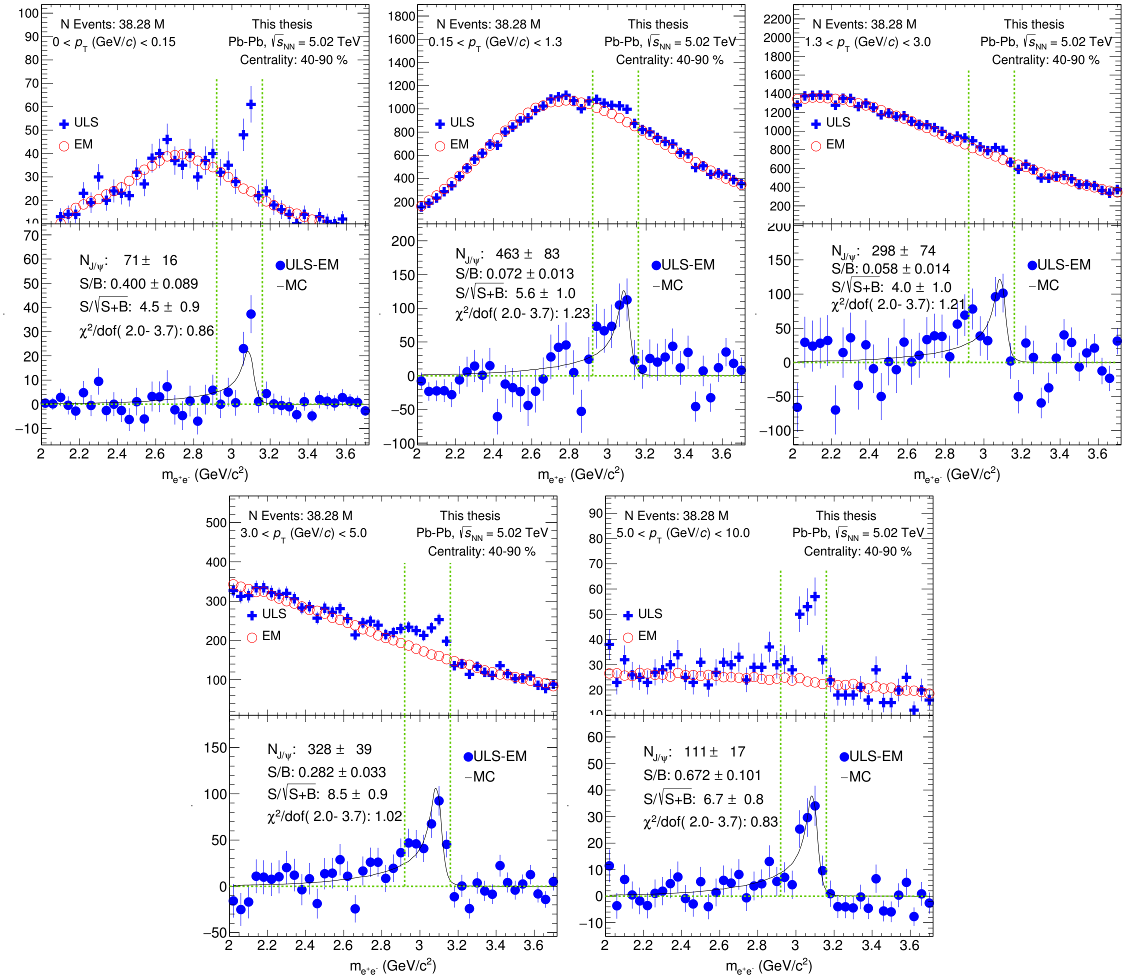

Figure 4.12: Signal extraction performed with the event-mixing method for the five different p_{T} intervals in the centrality class 40-90%. The p_{T} interval is indicated in each panel.

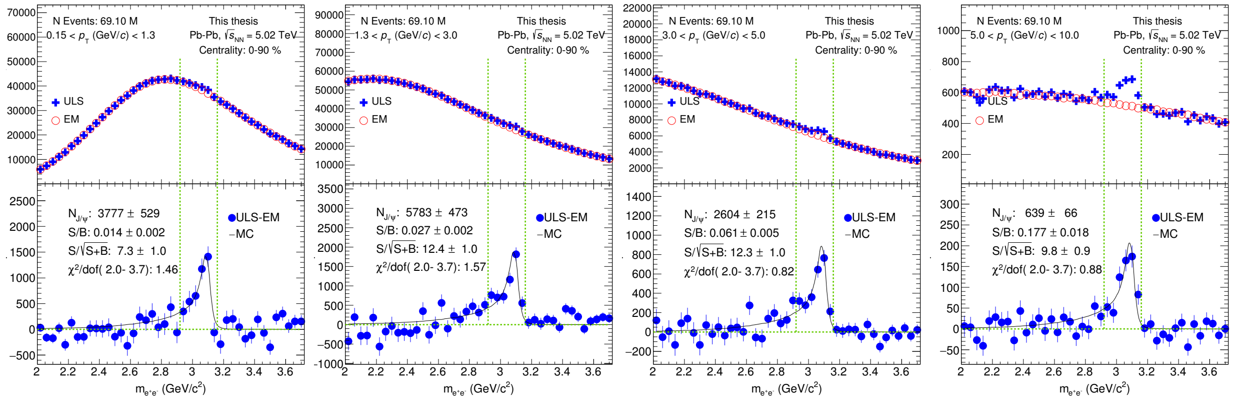

Figure 4.13: Signal extraction performed with the event-mixing method for the four different p_T intervals in the centrality class 0-90%. The p_T interval is indicated in each panel.

4.6 Monte Carlo sample

The Monte Carlo (MC) sample used consists of 1.5 million of events produced with HIJING as MC generator (see Section 3.3). The MC signals generated are treated similarly to data by the offline framework, using the same detector setup and configuration as the one in data. That allows evaluating the corrections at the same running conditions.

Due to the scarcity of J/ψ production in HIJING, the MC simulation must be enriched with J/ψ signals to have enough statistics to compute the J/ψ reconstruction efficiency (This will be shown in Section 4.6.2). The simulated events are created as a combination of 1 HIJING event + 10 J/ψ injected signals per event. The MC simulation produces 70% of the total number of events with a prompt J/ψ, generated according to a p_{T} spectrum of inclusive J/ψ based on EKS98 [132]. The other 30 % of events are produced as 1 HIJING event + 1 $b\bar{b}$-pair generated with Pythia Perugia0 tune [133]. Both b-quarks decay channels produce a J/ψ. Additionally, as PYTHIA does not include the radiative decays of J/ψ (J/$\psi \rightarrow e^+e^-\gamma$), the decay is handled using EvtGen [134] instead of Pythia and the final state radiation is described with PHOTOS [135]. The inclusion of the radiative decays is important in the efficiency calculation. This is further explained in Section 4.6.2. When computing the $Acc. \times Eff.$, the J/ψ production is assumed to be unpolarized and no extra systematic uncertainty is considered due to a possible polarization. In Pb–Pb collisions, the J/ψ production from charm quarks in the medium is expected to be unpolarized [83].

The z_{vtx} distribution of all triggered events with a reconstructed primary vertex after the event selection is shown in Figure 4.14. The distribution is well described by the Monte Carlo simulation and the vertex reconstruction efficiency is independent of the vertex position in the selected region $|z_{\mathrm{vtx}}| < 10$ cm.

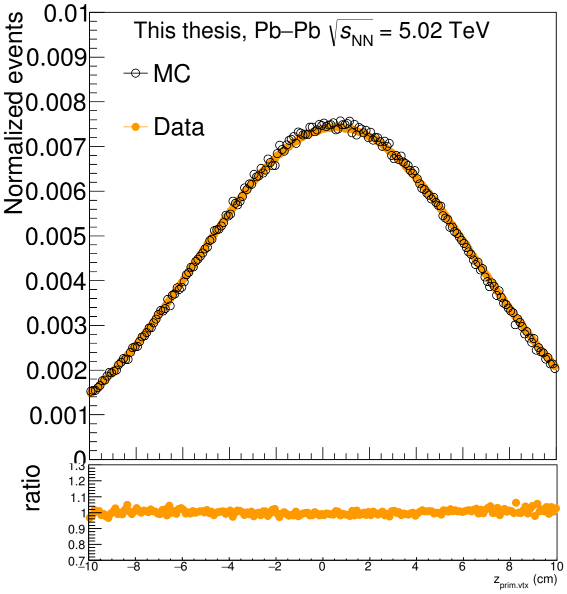

Figure 4.14: Primary event vertex distribution in data and Monte Carlo in the region $|Z_{\mathrm{vtx}}| < 10$ cm. The bottom panel shows the ratio.

4.6.1 Monte Carlo description of the track variables

The distributions of the variables used in the track quality selection criteria listed in Section 4.3.1 for data are compared to Monte Carlo in Figure 4.15. The comparison is performed for unidentified tracks after applying the same track selection criteria described in Sec 4.3.1. The filled color region corresponds to the tracks after the selection is applied. Although the distributions are not perfectly described in all the region, the fraction of accepted tracks (indicated in the top of each panel) is in agreement between data and MC. Possible differences on the measurement arising from this variations are studied in the systematic studies described in Section 5.2.

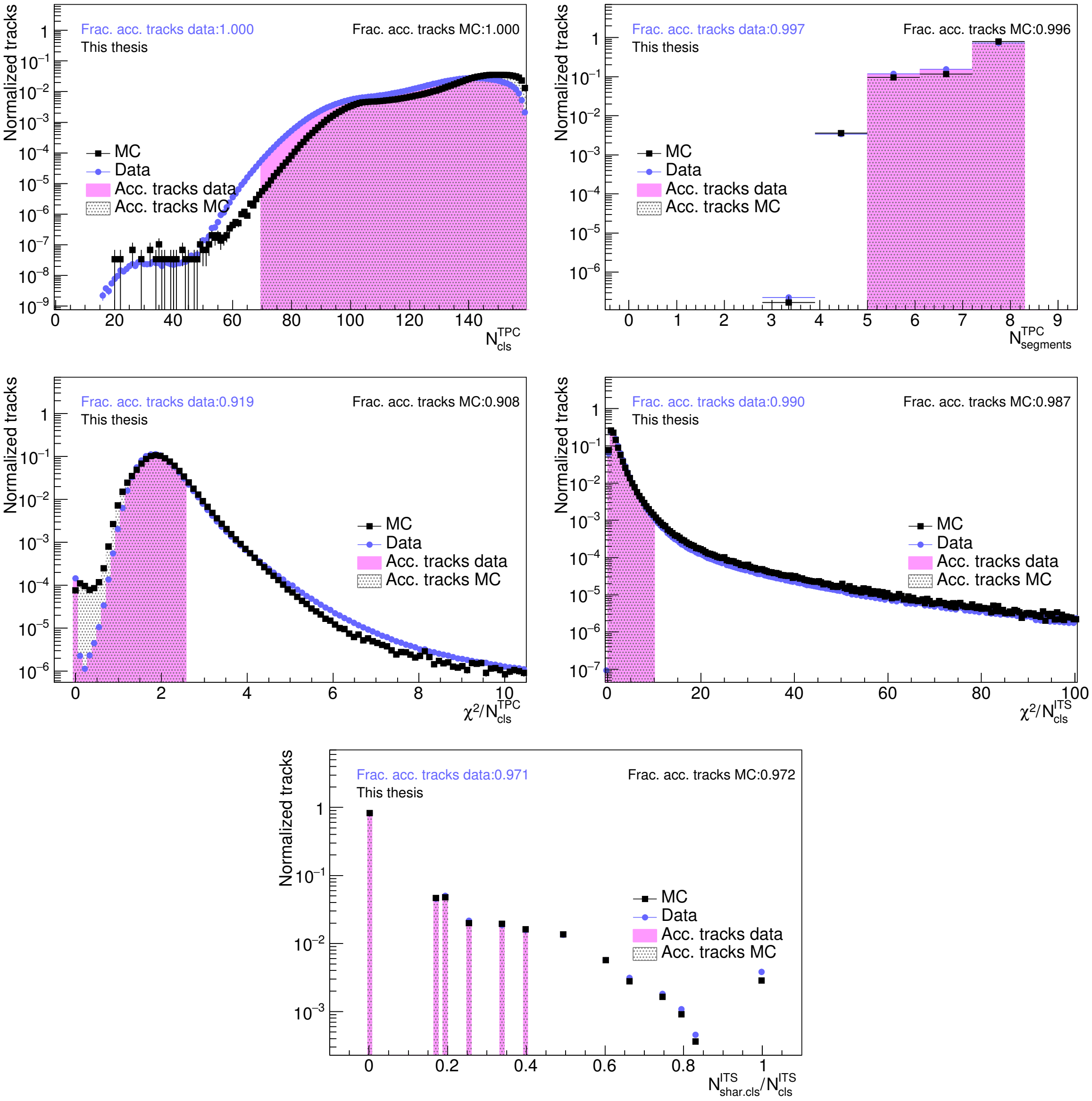

Figure 4.15: Fraction of accepted tracks for data (in purple) compared to the MC reconstructed tracks (black). The filled areas represent the fraction of tracks selected after the track cuts are applied. The fraction of accepted tracks in the selection region is shown at the top of each panel.

4.6.2 Efficiency calculation

The raw J/ψ yield ($N_{J/\psi,\mathrm{raw}}$) obtained after the signal extraction corresponds to a partial amount of the total J/ψ yield produced in the collisions. The $N_{J/\psi,\mathrm{raw}}$ is affected by the several effects like detector acceptance, track and PID selection, dead detector zones, noisy channels in the detector, etc. Therefore the MC sample is used to evaluate the efficiency. The factor to obtain the corrected J/ψ yield ($N_{J/\psi,\mathrm{corr}}$), corresponds to the acceptance times efficiency ($Acc. \times Eff.$)

$$N_{J/\psi,\mathrm{corr}} = \frac{N_{J/\psi,\mathrm{raw}}}{Acc. \times Eff.}. \tag{4.6}$$

The $Acc. \times Eff.$ is computed from MC simulations and is defined as:

$$Acc. \times Eff. = \frac{N_{J/\psi\,\mathrm{rec}}}{N_{J/\psi,\mathrm{gen}}}, \tag{4.7}$$

with $N_{J/\psi\,\mathrm{rec}}$ and $N_{J/\psi,\mathrm{gen}}$ representing the number of reconstructed and generated J/ψ's in the same acceptance region.

The J/ψ p_T and y distributions used as input for the efficiency calculations are shown in Figure 4.16. As the rapidity distribution in the region $|y| < 0.9$ is almost flat, and no rapidity dependence is expected in the central rapidity region $|y| < 0.9$ [83, 136] no further correction was considered. On the other hand, the prompt J/ψ production shows a p_T distribution with an atypical behavior: the p_T region below 500 MeV/c, and above 6 GeV/c shows a flat trend. The MC production is generated with a modified p_T spectra to have sufficient statistics to perform efficiency calculations in both p_T regions [6]. Due to the input p_T distributions used in the enhanced J/ψ production, a re-weighting procedure using real measured p_T distributions has to be used to recover a distribution similar to the real ones. This will be explained in Section 4.6.3.

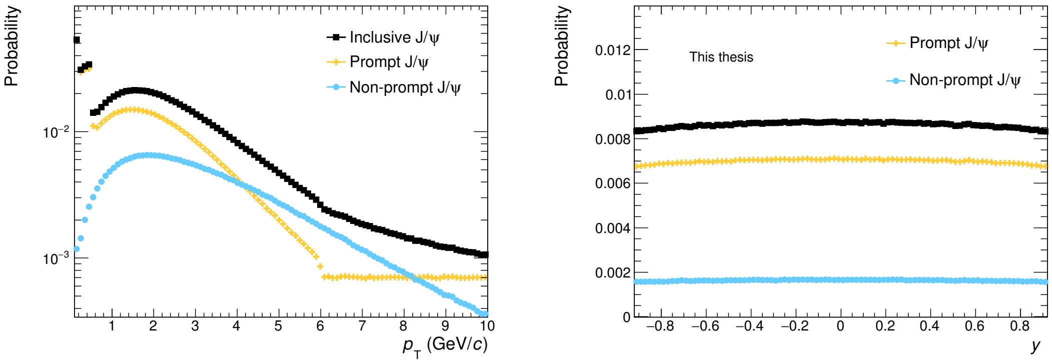

Figure 4.16: MC input shape for the prompt (blue) and non-prompt (yellow) J/ψ components. Left: Transverse momentum distributions. Right: Rapidity distributions.

The $Acc. \times Eff.$ can be separated according to the subsequent selection steps as:

$$\begin{aligned} Acc. \times Eff. &= \frac{N_{J/\psi\,\mathrm{gen,\,kin}}}{N_{J/\psi\,\mathrm{gen}}} \cdot \frac{N_{J/\psi\,\mathrm{rec,\,track}}}{N_{J/\psi\,\mathrm{gen,\,kin}}} \cdot \frac{N_{J/\psi\,\mathrm{rec,\,track+PID}}}{N_{J/\psi\,\mathrm{rec,\,track}}} \cdot \frac{N_{J/\psi\,\mathrm{rec,\,track+PID+mass\,window}}}{N_{J/\psi\,\mathrm{rec,\,track+PID}}} \\ &= Eff_\mathrm{kin} \cdot Eff_\mathrm{tracking} \cdot Eff_\mathrm{PID} \cdot Eff_\mathrm{mass\,window} \end{aligned}$$

where $N_{J/\psi\,\mathrm{gen,\,kin}}$ represents the J/ψ yield after the kinematics selection; $N_{J/\psi\,\mathrm{rec,\,track}}$ the tracking selection; $N_{J/\psi\,\mathrm{rec,\,track+PID}}$ the PID selection; and $N_{J/\psi\,\mathrm{rec,\,track+PID+mass\,window}}$ the mass window where the signal is extracted after applying the tracking and PID selection. The corresponding selections are explained in Section 4.3.1. The values for the components of the efficiency from Eq. 4.8 are shown in Figure 4.18.

Geometrical acceptance + kinematics

The TPC mainly determines the geometrical acceptance. Figure 4.18 (Left) shows the y dependence of the kinematic selection in blue markers. The distributions show a maximum at zero and decrease for larger rapidity due to the

---

[6] At very low p_T, an enhancement of the J/ψ was already observed by ALICE in peripheral collisions at forward-rapidity at lower energies (see Section 2.7). Due to the increase of statistics during LHC Run 2, this measurement is also possible at mid-rapidity and therefore enough statistics is needed in this p_T region to compute efficiencies. The measurement of the very low p_T J/ψ is outside the scope of the work presented here. More details on this measurement will be discussed in Chapter 5.

kinematic selection applied on the single electron legs. Figure 4.18 (right) shows the p_{T} dependence of the kinematic selection in blue markers. The decrease towards 2 GeV/c is produced by the minimum p_{T} requirement on the single electron track. The opening angle between the electron candidates of a J/ψ decay decreases with increasing the p_{T} of the J/ψ. Therefore, both electrons are produced approximately in the same direction increasing the probability of reconstructing both tracks.

Tracking efficiency

In addition to the pure kinematic selection, the electrons produced in the J/ψ decay have to pass the track selection described in Section 4.3.1. The tracking efficiency (Eff_{tracking}) is calculated as the ratio between produced J/ψ and reconstructed J/ψ passing the track selection. The tracking efficiency is shown in pink markers in Figure 4.18.

Particle identification efficiency

The particle identification efficiency (Eff_{PID}) is calculated as the ratio between J/ψ's after the PID selection and the reconstructed J/ψ's after the track selection is applied. Figure 4.18 shows the y and p_{T} dependence of the PID efficiency in orange. The p_{T} dependence of the Eff_{PID} is characterized by the $n\sigma_{\mathrm{TPC},\pi}$ and $n\sigma_{\mathrm{TPC,p}}$ exclusion selection. The dE/dx of the protons and electrons as a function of p, crosses at $\approx$ 1 GeV/c (see Figure 3.5), the exclusion selection creates the decrease of the efficiency in this p_{T} region. The decrease observed at p_{T} above 5 GeV/c is due to the pion rejection, where the dE/dx between the pions and the electrons is similar.

Mass window efficiency

Figure 4.17 shows the J/ψ invariant mass distribution for the radiative and the non-radiative decays. The mass exhibits a shift toward lower masses with respect to the J/ψ mass due to the energy loss of the electrons in the material. The shift towards lower masses is more pronounced in the case of the non-radiative production, due to the neglected contribution of the emitted soft photon. The two different J/ψ productions produce slightly different *Acc.* × Eff. [137]. However the fraction of non-radiative decays is described by PHOTOS [135] based on precise QED calculations [7]. The signal is extracted in the region [2.92 - 3.16] GeV/c^2, as explained in 4.4 and the fraction of the total J/ψ reconstructed in this mass window corresponds to 64% of the total J/ψ reconstructed after applying the track selection. Different mass window regions used to extract the J/ψ signal are considered as possible source of systematic uncertainties (see Section 5.1).

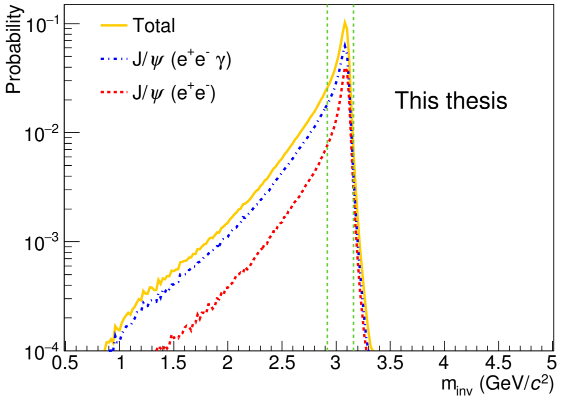

Figure 4.17: Invariant mass distribution for the radiative and the non-radiative decays, normalized to the total J/ψ production. The green lines indicate the mass region where the signal is extracted.

---

[7] The energy cut-off for photo production used in the photos simulation is $E_{\gamma} > 10^{-7}$ MeV.

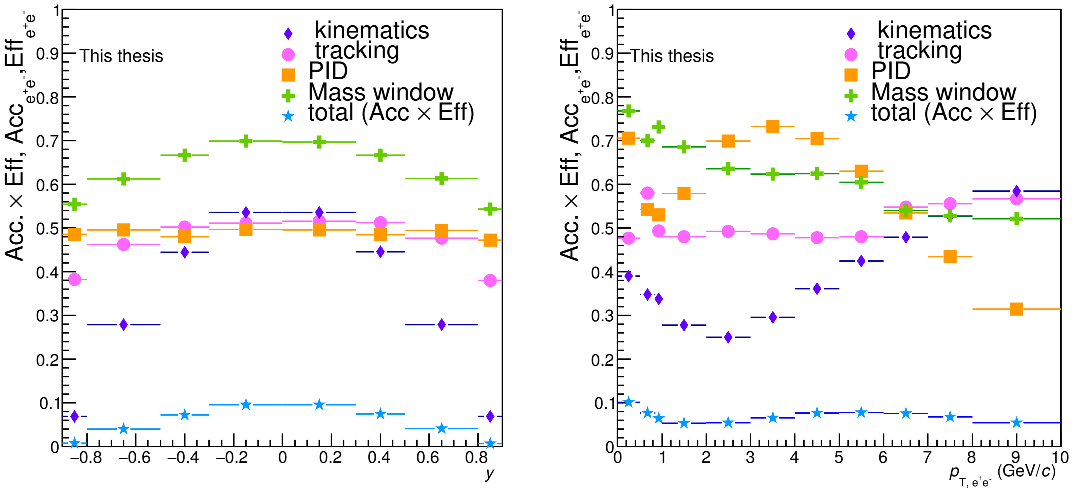

Figure 4.18: Inclusive J/ψ $Acc. \times Eff.$ components. Left: y dependence. Right: p_{T} dependence.

4.6.3 Efficiency re-weighting

The p_{T} distributions used for the $Acc. \times Eff.$ calculation are re-weighted with a real measurement to recover the real p_{T} distribution shape. As the distribution at mid-rapidity is not measured with sufficient precision, the ALICE J/ψ measurement at forward rapidity ($2.5 < y < 4.0$) is used [138]. The spectra are fitted with the function from Eq. 4.8 taking into account the statistical and systematic uncertainties. This function reproduce the transverse momentum of the the inclusive J/ψ production for different available experimental data [139, 140]. The corresponding fits are shown in Figure 4.19.

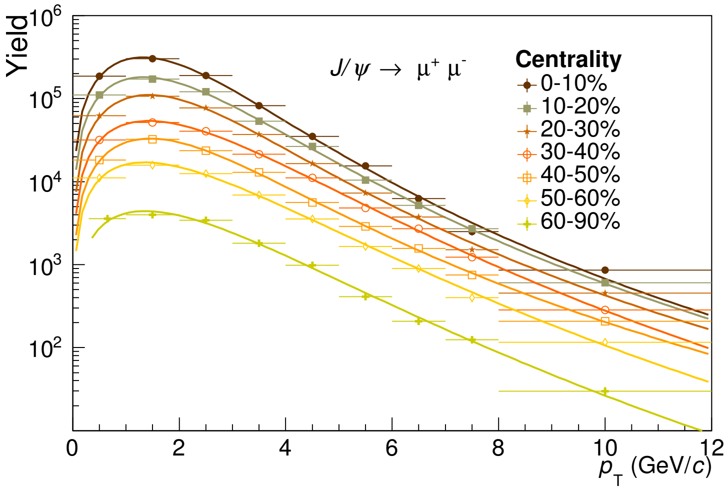

Figure 4.19: Fit to the ALICE inclusive J/ψ yield measurement at forward rapidity.

$$f(p_T) = C \cdot \frac{p_T}{(1 + (p_T/p_0)^2)^n} \tag{4.8}$$

The efficiencies are computed in the centrality bins: 0−10%, 10−20%, 20−40%, 40−60%, 60−90%, and the $Acc. \times Eff.$ is weighted in each p_{T} bin with the value of the measurement. The $Acc. \times Eff.$ values after the re-weight are shown in Figure 4.20.

As the efficiency has to be computed in the same centrality classes as for those used to extract the raw J/ψ yield, an additional re-weighting by the number of $\langle N_{coll}\rangle$ (see Section 3.5) in each centrality class is applied, in the following way:

$$Eff_{20-40\%} = \frac{Eff_{20-30\%} \times \langle N_{coll20-30\%}\rangle + Eff_{30-40\%} \times \langle N_{coll30-40\%}\rangle}{\langle N_{coll20-30\%}\rangle + \langle N_{coll30-40\%}\rangle}, \tag{4.9}$$

$$Eff_{40-60\%} = \frac{Eff_{40-50\%} \times \langle N_{coll40-50\%}\rangle + Eff_{50-60\%} \times \langle N_{coll50-60\%}\rangle}{\langle N_{coll40-50\%}\rangle + \langle N_{coll50-60\%}\rangle}. \tag{4.10}$$

The efficiency correction applied as a function of transverse momentum is shown in Figure 4.20 (Right). The *Acc.* × $Eff.$ integrated over p_{T} after the re-weight procedure is shown in Figure 4.21 for different centralities, the dependence efficiency with centrality is due to the $TPC\chi^2/n_{cls}$ selection which affects more the central events.

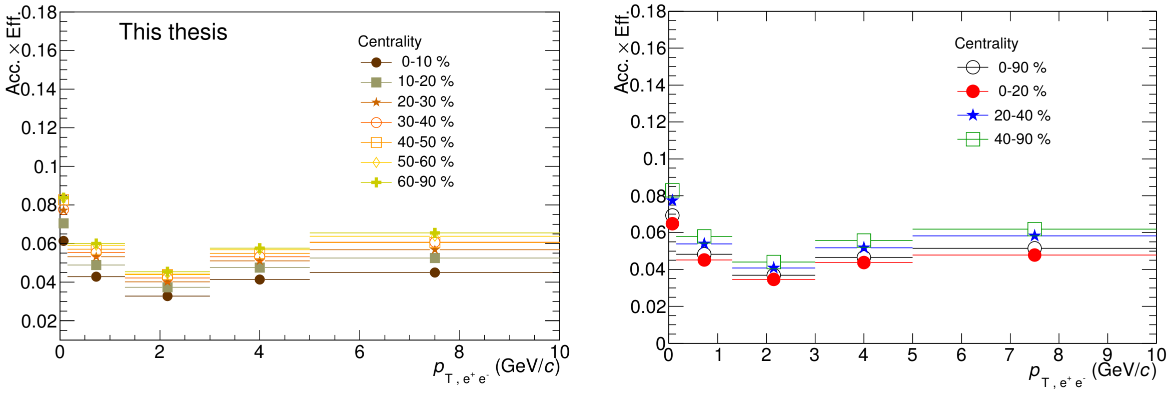

Figure 4.20: Left: J/ψ *Acc.*×$Eff.$ computed same centrality classes as the fit to the forward rapidity measurement as a function of transverse momentum. Right: *Acc.* × $Eff.$ as a function of transverse momentum in the four centrality bins used for the measurement of the J/ψ production as a function of transverse momentum.

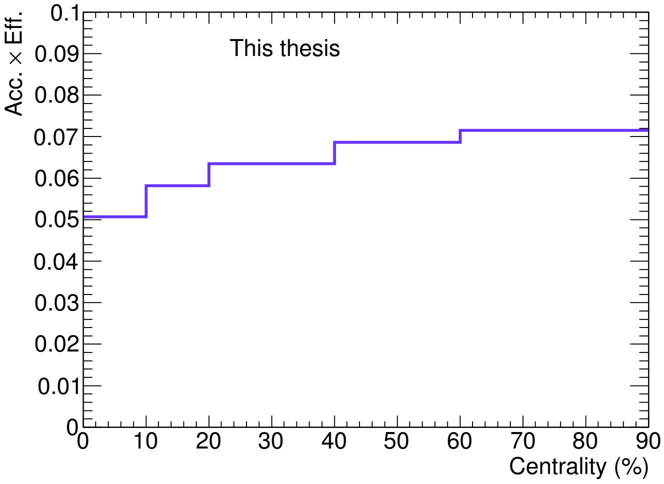

Figure 4.21: J/ψ *Acc.* × $Eff.$ integrated over p_{T} for the different centrality classes.

4.7 pp reference

The J/ψ cross-section in pp collisions at $\sqrt{s} = 5.02$ TeV $p_{\rm T}$-integrated ($d\sigma^{\rm pp}_{J/\psi}/dy$) and $p_{\rm T}$-differential ($d^2\sigma^{pp}_{J/\psi}/dydp_{\rm T}$) are needed to compute the nuclear modification factor of the J/ψ. The statistics on the data sample of pp collisions are limited and already the measurement of the $\mathrm{d}N_{\mathrm{J}/\psi}/\mathrm{d}y$ is challenging. This can be observed in Figure 4.22, where 142±14 J/ψ's are reconstructed. The measurement of the J/ψ cross-section in pp collisions at $\sqrt{s} = 5.02$ TeV is detailed in Appendix A. In addition to the measurement different interpolations procedures to obtain $\mathrm{d}N_{\mathrm{J}/\psi}/\mathrm{d}y$ and $\mathrm{d}^2N_{J/\psi}/\mathrm{d}y\mathrm{d}p_T$ are detailed in Sections 4.7.1 and 4.7.3, respectively. The comparison of the values obtained with the measurement and the interpolation are discussed in Section 4.7.2.

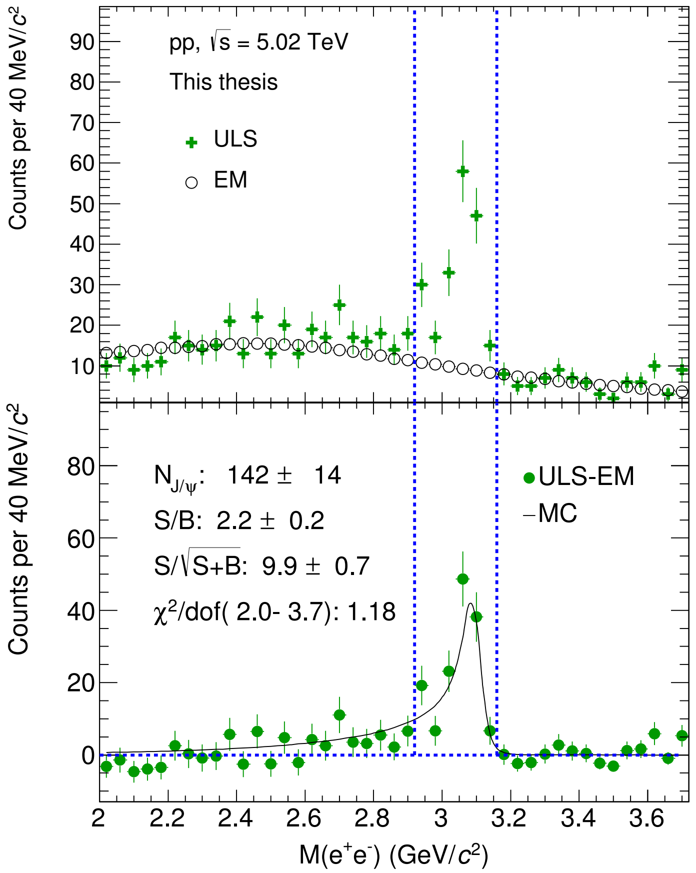

Figure 4.22: *Top*: Invariant mass distribution obtained in pp collisions. *Bottom*: Signal after background subtraction, the MC shape is indicated with the solid line.

4.7.1 $p_{\rm T}$-integrated J/ψ cross-section (Interpolation)

The $p_{\rm T}$-integrated J/ψ cross-section ($d\sigma^{\rm pp}_{J/\psi}/dy$) in pp collisions at $\sqrt{s} = 5.02$ TeV is obtained by an interpolation procedure detailed in Ref. [141]. The procedure is based on different inclusive J/ψ production measurements in pp and p$\bar{\rm p}$ collisions at different energies. The different measurements at mid-rapidity and the corresponding $d\sigma^{\rm pp}_{\mathrm{J}/\psi}/dy$, and J/$\psi$ mean transverse momentum ($\langle p_T\rangle$) are summarized in Table 4.2. Figure 4.23 (Top) shows the different measurements of CDF in p$\bar{\rm p}$ at $\sqrt{s} = 1.96$ TeV [36] and PHENIX in pp collisions at $\sqrt{s} = 0.2$ TeV [142] and ALICE measurements in pp collisions at $\sqrt{s} = 2.76$ TeV [143] and 7 TeV [128].

The interpolation procedure consists of fitting the $\sqrt{s}$-dependence of the inclusive J/ψ production cross-section with different functions. The interpolation is derived as the average of the three different functional assumptions

Compilation of J/ψ measurements at mid-rapidity					
Experiment	$\sqrt{s}$ (TeV)	y	$\mathrm{d}\sigma^{\mathrm{pp}}_{J/\psi}/\mathrm{d}y$ (μb)	$\langle p_T \rangle$ (GeV/c)	Ref.
PHENIX	0.20	$\lvert y \rvert < 0.35$	0.79 ± 0.05	1.78 ± 0.07	[142]
CDF	1.96	$\lvert y \rvert < 0.60$	3.40 ± 0.30	2.47 ± 0.07	[36]
ALICE	2.76	$\lvert y \rvert < 0.90$	4.25 ± 0.52	2.60 ± 0.04	[143]
	7.00	$\lvert y \rvert < 0.90$	6.90 ± 1.18	2.91 ± 0.31	[128]

Table 4.2: Collection of inclusive J/ψ cross-sections and $\langle p_T \rangle$ in pp and p$\bar{\mathrm{p}}$ by different experiments at different center-of-mass energies.

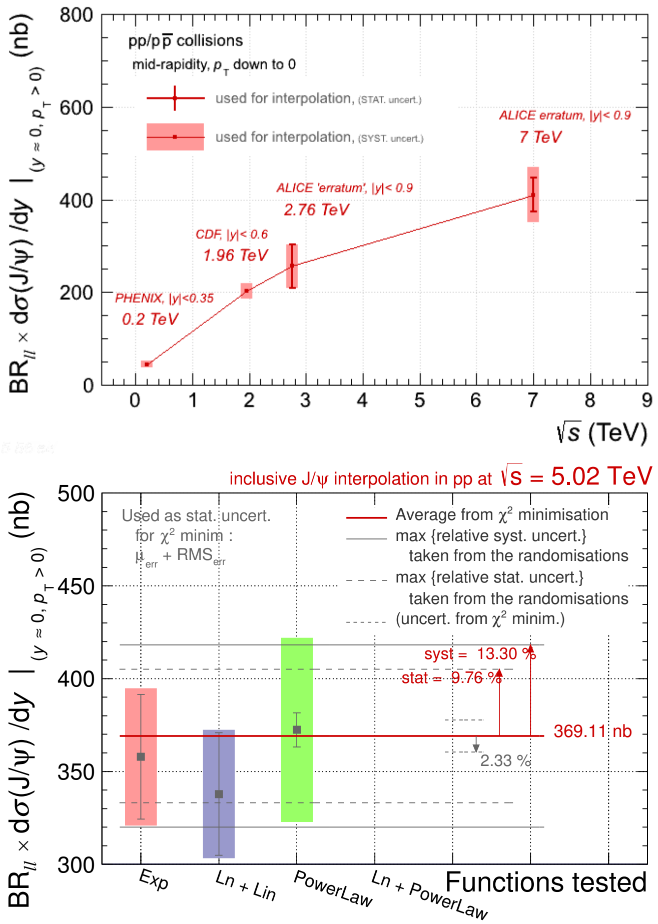

Figure 4.23: *Top*: Experimental data used for the interpolation of the J/ψ cross-section in pp collisions at $\sqrt{s}$ = 5.02 TeV. *Bottom*: Result of the interpolation procedure using different fits. The average of the three different functional assumptions is shown in the ref line. Figures taken from [144].

for the $\sqrt{s}$ dependence as shown in Figure 4.23 (bottom). The uncertainty in the interpolation is obtained from the quadratic sum of the statistical and systematic uncertainties. Details on the procedure can be found in Ref. [141]. The value used corresponds to $d\sigma^{pp}_{J/\psi}/dy = 6.16 \pm 1.03\ \mu$b, with a B.R. corresponding to $5.971 \pm 0.0032\%$ [8].

4.7.2 Inclusive J/ψ production cross-section comparison

The measurement presented in this work (see Appendix A) represents a first attempt to obtain the $d\sigma^{pp}_{J/\psi}/dy$ at $\sqrt{s} = 5.02$ TeV and shows the importance of collecting a large pp data sample at $\sqrt{s} = 5.02$ TeV. At the time of the writing of this thesis, ALICE possesses a data sample of pp collisions at $\sqrt{s} = 5.02$ TeV with approximately 1300 million events taken at the end of the year 2017. This represents about ten times more statistics than the pp measurement presented here and will represent a major improvement on the R_{AA} uncertainties. Due to time restrictions, the analysis of the pp 2017 data sample is not included in this work.

The measurement of $\mathrm{d}\sigma^{\mathrm{pp}}_{\mathrm{J}/\psi}/\mathrm{d}y = 6.80 \pm 0.67(\mathrm{stat.}) \pm 0.53(\mathrm{syst})$ in pp collisions at $\sqrt{s} = 5.02$ TeV was obtained in this work. The result is compatible within uncertainties with the value obtained with the interpolation procedure, providing an improvement of approximately 4% in the global uncertainty. However, when considering the $\mathrm{d}\sigma^{pp}_{J/\psi}/\mathrm{d}y$ obtained at $\sqrt{s} = 7.0$ TeV (see Table 4.2) and the energy scaling expected, the mean value in the measurement at $\sqrt{s} = 5.02$ TeV seems to be in the upper limit. Therefore, the interpolation result was used instead of the measurement in the R_{AA} calculation presented in the following chapters.

4.7.3 p_{T}-differential J/ψ cross-section

An interpolation procedure is used in order to obtain the p_{T}-differential J/ψ cross-section in the same p_{T} intervals needed to compute the R_{AA}. The procedure is described in Ref. [145] and is based on the phenomenological approach studied in Ref. [139]. The J/ψ cross-section is obtained by fitting a universal function:

$$\frac{\langle p_T \rangle}{d\sigma^{pp}_{J/\psi}/dy} \frac{d^2\sigma^{pp}_{J/\psi}}{dy dp_T} = \frac{2(n-1) \cdot B^2 p_T/\langle p_T \rangle}{(1 + B^2 \cdot (p_T/\langle p_T \rangle)^2)^n} \tag{4.11}$$

in terms of the $\langle p_T \rangle$, the values of $d\sigma^{pp}_{J/\psi}/dy$ and the function $B = \Gamma(3/2)\Gamma(n-3/1)/\Gamma(n-1)$ defined in terms of the Γ function. New and updated inclusive J/ψ measurements in pp collisions at $\sqrt{s} = 5.02$, 7.0, 8.0 and 13.0 TeV at forward rapidity published by ALICE in Ref. [146] were also included in the universal fit function.

The $\langle p_T \rangle$ dependence is obtained from interpolating the measurements at mid-rapidity with different functions shown in Figure 4.24.

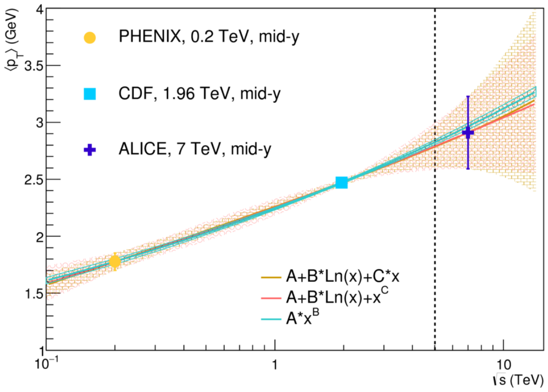

Figure 4.24: Energy dependence of the $\langle p_T \rangle$ interpolation for different inclusive J/ψ production measurements at mid-rapidity in pp and p$\bar{\mathrm{p}}$ collisions. The vertical line indicates the center-of-mass energy corresponding to 5.02 TeV.

The $\mathrm{d}^2\sigma^{\mathrm{pp}}_{\mathrm{J}/\psi}/\mathrm{d}y\mathrm{d}p_{\mathrm{T}}$ is obtained using the values of the $\langle p_T \rangle$ and $\mathrm{d}\sigma^{\mathrm{pp}}_{J/\psi}/\mathrm{d}y$ together with the universal function from Eq. 4.11. The fit to the universal function of the different measurements is shown in Figure 4.25 (Left). The uncorrelated p_{T}-dependent systematic uncertainties on the $\mathrm{d}^2\sigma^{\mathrm{pp}}_{\mathrm{J}/\psi}/\mathrm{d}y\mathrm{d}p_{\mathrm{T}}$ are computed by fitting the ratio $|data - fit|/|data + fit|$ with all the experimental inclusive J/ψ spectra $\mathrm{d}^2\sigma^{\mathrm{pp}}_{\mathrm{J}/\psi}/\mathrm{d}y\mathrm{d}p_{\mathrm{T}}$ and the different interpolation functions transformed accordingly into $\mathrm{d}^2\sigma^{\mathrm{pp}}_{\mathrm{J}/\psi}/\mathrm{d}y\mathrm{d}p_{\mathrm{T}}$ using the values of $\langle p_{\mathrm{T}}\rangle$ and $\mathrm{d}\sigma^{\mathrm{pp}}_{\mathrm{J}/\psi}/\mathrm{d}y$ from Table 4.2. The different measurements and the universal fit scaled to the different energies with the corresponding calculated uncertainties are shown in Figure 4.25 (Right).

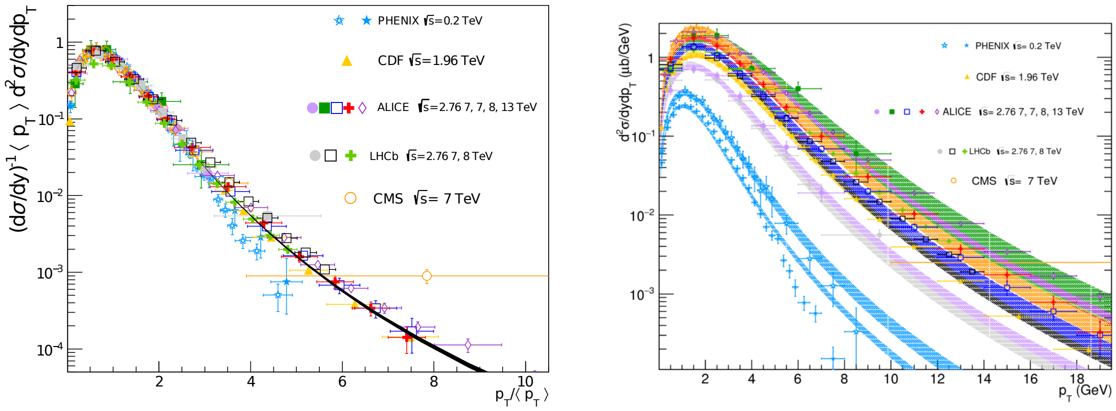

Figure 4.25: *Left*: Simultaneous universal fit to the different scaled data as a function of the $p_T/\langle p_T\rangle$. *Right*: Universal fits compared to the experimental data.

The values of the $\mathrm{d}^2\sigma^{\mathrm{pp}}_{\mathrm{J}/\psi}/\mathrm{d}y\mathrm{d}p_{\mathrm{T}}$ and the different systematic uncertainties arising from the interpolation procedure are summarized in Table 4.3. Including the new ALICE data leads to modifications below 2% in the lowest p_{T} intervals with respect to the interpolation reported in Ref. [145].

Numerical values of the pp cross-section					
p_{T} (GeV/c)	$\mathrm{d}^2\sigma^{\mathrm{pp}}_{\mathrm{J}/\psi}\mathrm{d}y\mathrm{d}p_{\mathrm{T}}$	Systematic uncertainties			
		Cor. (abs. val.)	Unc. (abs. val.)	Cor. (%)	Unc. (%)
0.0< p_{T} < 0.15	0.128	0.021	0.009	16.66	6.2
0.15< p_{T} < 1.30	1.064	0.176	0.066	16.66	6.2
1.3< p_{T} < 3.00	1.597	0.265	0.073	16.66	4.6
3.0< p_{T} < 5.00	0.776	0.129	0.040	16.66	5.2
5.0< p_{T} < 10.00	0.126	0.021	0.015	16.66	11.8

Table 4.3: Values of the inclusive J/ψ production cross-section in pp collisions at $\sqrt{s}$ = 5.02 TeV obtained with the interpolation procedure including the systematic uncertainties.

4.8 Observables

In this section the observables obtained after correcting the J/ψ yield are presented. Using the procedure described in the previous sections the corrected p_{T}-integrated J/ψ yield can be computed as:

$$\frac{\mathrm{d}N_{\mathrm{J}/\psi}}{\mathrm{d}y} = \frac{1}{N_{\mathrm{ev}}}\frac{N_{\mathrm{J}/\psi}}{\cdot\Delta y\cdot B.R._{\mathrm{J}/\psi\rightarrow ee}\cdot Acc.\times Eff(cent)}. \tag{4.12}$$

Analogously, the p_{T}-differential inclusive J/ψ yield is computed as:

$$\frac{\mathrm{d}^2N_{\mathrm{J}/\psi}}{\mathrm{d}y\mathrm{d}p_{\mathrm{T}}} = \frac{1}{N_{\mathrm{ev}}}\frac{\mathrm{N}_{\mathrm{J}/\psi}}{\Delta p_{\mathrm{T}}\cdot\Delta y\cdot B.R._{\mathrm{J}/\psi\rightarrow ee}\cdot Acc.\times Eff(cent,p_{\mathrm{T}})}, \tag{4.13}$$

where $N_{\mathrm{J}/\psi}$ denotes the number of raw J/ψ yield obtained with the signal extraction in the different centrality classes. The term $Acc.\times Eff.$ represents the acceptance times efficiency in the same centrality class, and the factors Δp_{T} and Δy represent the width of the p_{T} and rapidity intervals, respectively. The $B.R._{J/\psi \rightarrow ee}$ represents the J/ψ branching ratio to electrons and N_{ev} the number of events.

The nuclear modification factor for the inclusive J/ψ production p_{T} integrated and p_{T}-differential are computed as:

$$R_{AA} = \frac{\mathrm{d}N_{J/\psi}/\mathrm{d}y}{\langle T_{AA} \rangle \mathrm{d}\sigma^{\mathrm{pp}}_{J/\psi}/\mathrm{d}y}, \tag{4.14a}$$

$$R_{AA} = \frac{\mathrm{d}^2 N_{J/\psi}/\mathrm{d}y\mathrm{d}p_{\mathrm{T}}}{\langle T_{AA} \rangle \mathrm{d}^2\sigma^{\mathrm{pp}}_{J/\psi}/\mathrm{d}y\mathrm{d}p_{\mathrm{T}}}, \tag{4.14b}$$

where the corrected yields have been defined in Eqs. 4.12 and 4.13, the nuclear overlap function $\langle T_{AA} \rangle$ is obtained from the centrality estimation (see Table 3.1) and the terms $\mathrm{d}\sigma^{pp}_{J/\psi}/\mathrm{d}y$ and $\mathrm{d}^2\sigma^{pp}_{J/\psi}/\mathrm{d}y\mathrm{d}p_{\mathrm{T}}$ represent the cross-section in pp collisions p_{T} integrated and as function of p_{T} respectively. The measurement of the observables defined in Eqs. 4.12 , 4.13 and 4.14 will be discussed in the following chapters.

5

Systematic uncertainties estimation

This chapter presents the different sources of systematic uncertainties on the inclusive J/ψ production measurement. The systematic uncertainties arising from the signal extraction method are presented in Section 5.1, the systematic uncertainties due to track and PID selections are presented in Section 5.2 and Section 5.3, respectively. A discussion on the sources mentioned is discussed in Section 5.4. Additionally, the systematic uncertainties estimation due to the input MC p_{T} spectra shape is presented in Section 5.5. The values of the systematic uncertainties due to the nuclear overlap factor and the summary of the different systematic uncertainties on the different observables are presented in Sections 5.6 and 5.7.

The track, PID and signal extraction selections in this analysis have been selected in a process based on optimizing the significance and the statistical uncertainty on the raw number of J/ψ's obtained after the signal extraction. As the analysis suffers from relatively large statistical uncertainties and a low signal over background, the optimization may involuntarily favor a signal fluctuation leading towards higher yields. To avoid this effect on the final result, the different selections are varied and a final corrected yield is computed for each variation. The mean value of all the variations is reported as the final result and the mean of the statistical uncertainties is assigned as the statistical uncertainty of the final result. The selection described in the previous chapter is denominated *standard* in the following of the chapter.

Other commonly used approaches based on optimizing the selection in Monte Carlo simulations is not possible due to inadequate description of the background in the dielectron channel mainly because of the differences in the physics between data and the Monte Carlo models. Optimization of the selection criteria based on a partial data sample is also avoided due to the already high statistical uncertainty in the analysis. A recent approach initialized in Ref. [147] indicates that machine learning methods can be employed as a useful and powerful tool. However, further developing and detailed studies are needed before being considered. For this analysis the variation of the result with the different selections with respect to the standard was studied.

5.1 Signal extraction

The systematic uncertainties arising from the signal extraction procedure (see Section 4.4) are evaluated varying two of the main parameters of the signal extraction method *i.e.* the mass window where the signal is extracted and the background scaling region. The mass window used to extract the signal is varied from the standard in different ranges. The value of the $Acc \times Eff$ is also computed for each of the cases, as the $Eff_{\text{mass window}}$ is also modified due to the integration region of the signal. The different regions used to scale the event mixing background to match the unlike-sign pairs distribution are also varied from the standard values in four different ranges. The different scaling regions and mass windows evaluated are listed in Table 5.1. The effect on the inclusive J/ψ yield due to the variations on the signal extraction will be presented in Section 5.3.1.

Signal extraction parameters		
Parameter	**Standard value ($\mathbf{GeV}/c^2$)**	**Variation ($\mathbf{GeV}/c^2$)**
Background scaling region	[2.0 - 2.5, 3.2 - 3.7]	[1.8 - 2.5, 3.2 - 3.9] [1.7 - 2.5, 3.2 - 4.0] [1.9 - 2.5, 3.2 - 3.8] [2.1 - 2.5, 3.2 - 3.6]
Signal counting mass window	[2.92 - 3.16]	[2.80 - 3.16] [2.92 - 3.12] [2.88 - 3.20] [2.92 - 3.16] [2.88 - 3.16] [2.84 - 3.12] [2.88 - 3.12]

Table 5.1: Standard values and variations for the mass window and background scaling region used to evaluate the systematic uncertainties related to the signal extraction.

5.2 Track selection

The systematic uncertainties arising from the track selection criteria are due to the residual discrepancy between the MC used to determine the total reconstruction efficiency and data. This is estimated by varying the track selection to a tighter and a looser value with respect to the standard value chosen in the analysis. The variation is performed within reasonable limits in order not to be affected by reduced statistics and not to deteriorate the performance of the measurement using regions where considerable differences between MC and data appear. Each variation is evaluated at the data level, extracting the raw number of J/ψ and calculating the corresponding value of the $Acc. \times Eff.$ The list of different track variations and the standard value is shown in Table 5.2. Loosening the TPCχ^2/cluster selection, which quantify the quality of the tracks is not evaluated because an optimal track resolution is needed for the event mixing method. Therefore, only a tighter variation is used in this case. The TPC$_{\mathrm{ncls.shared}}$ is only removed as a systematic variation due to the low fraction of rejected tracks by this variable. The effect on the inclusive J/ψ corrected yield due to the track variations will be presented in Section 5.3.1.

Track selection variations			
Variable	**Standard selection value**	**Loose variation**	**Tight variation**
$p_{\mathrm{T}\ e^{\pm}}$ (GeV/c)	> 1.0	> 0.9	> 1.1
$\lvert\eta_{e^{\pm}}\rvert$	< 0.9	-	< 0.8, 0.85
TPCχ^2/cluster	< 2.5	n.a	< 2.0
TPC segments	> 6	> 5	> 7
TPC clusters	> 70	>60	> 80
ITS χ^2/cluster	< 10	<15	< 5
Frac. ITS$_{shr.cls}$	< 0.4	<0.66	< 0.3
TPC$_{\mathrm{ncls.shared}}$	< 0.3	without	-

Table 5.2: Standard values and variations for track selection criteria used to evaluate the systematic uncertainties.

5.3 Particle identification

The systematic uncertainties due to the particle identification selection are evaluated with the variation of the electron and hadron selections in terms of the $n\sigma_{\mathrm{TPC,i}}$ values. In the following, $n\sigma_{\mathrm{TPC,i}}$ will be renamed as $n\sigma_i$ as it is implicit that the TPC is the detector used for the particle identification in all cases. The hadron selection is varied by 0.5σ to a tighter and to a looser value with respect to the standard value chosen in the analysis. An asymmetric selection in the case of the electron inclusion is also inspected in order to remove further pions in the negative nσ_e region. The list of different PID selections and the standard value is shown in Table 5.3. The inspection of both pion and proton exclusion variation together was also inspected as an extreme case. The effect on the inclusive J/ψ yield due to the PID variations will be presented in Section 5.3.1 together with the track and signal extraction selection variations.

PID selection variations		
nσ	**Standard selection value**	**Variation**
electron inclusion	-3<n$\sigma_e < 3$	-2<n$\sigma_e < 2$ -2<n$\sigma_e < 3$
pion exclusion	n$\sigma_\pi > 3.5$	n$\sigma_\pi > 3.0$ n$\sigma_\pi > 4.0$
proton exclusion	n$\sigma_p > 3.5$	n$\sigma_p > 3.0$ n$\sigma_p > 4.0$
pion+ proton exclusion	n$\sigma_\pi > 3.5 +$ n$\sigma_p > 3.5$	n$\sigma_\pi > 3.0 +$ n$\sigma_p > 3.0$ n$\sigma_\pi > 4.0 +$ n$\sigma_p > 4.0$

Table 5.3: Standard values and variations for the PID selection criteria used to evaluate the systematic uncertainties.

5.3.1 Systematic uncertainties for the p_{T}-integrated analysis

The p_{T}-integrated J/ψ corrected yield (d$N_{\mathrm{J}/\psi}$/dy) is computed according to Eq. 4.12 for each of the tracking, PID and signal extraction variations listed in Tables 5.1 to 5.3, respectively. The Figures 5.1 to 5.5 show the different inclusive J/ψ corrected yields obtained with each variation in the five centrality classes. The vertical lines indicate the separation between the track selection, PID selection, and signal extraction variations. The horizontal lines indicate the mean ($\langle$d$N_{\mathrm{J}/\psi}$/d$y\rangle$) of all the variations. As some of the variations considered may lead to a small signal to background ratio or significance, making the signal extraction difficult, the quality of the signal extraction procedure is monitored with the $\chi^2/d.o.f.$ between the normalized shape expected from MC and the data distributions (see Section 4.4) in the full mass window used in each case. All the variations are in agreement within statistical uncertainties. The mean is taken as the central value of the results to avoid any possible bias in the standard selection as explained at the beginning of this chapter.

The systematic uncertainties due to the tracking, particle identification, and signal extraction are not completely uncorrelated, since the evaluation of each variation relies on the signal extraction procedure and the $Acc. \times Eff.$ calculation. A conservative approach is adopted in this work taking the systematic uncertainties of each of these three contributions as uncorrelated and adding them in quadrature.

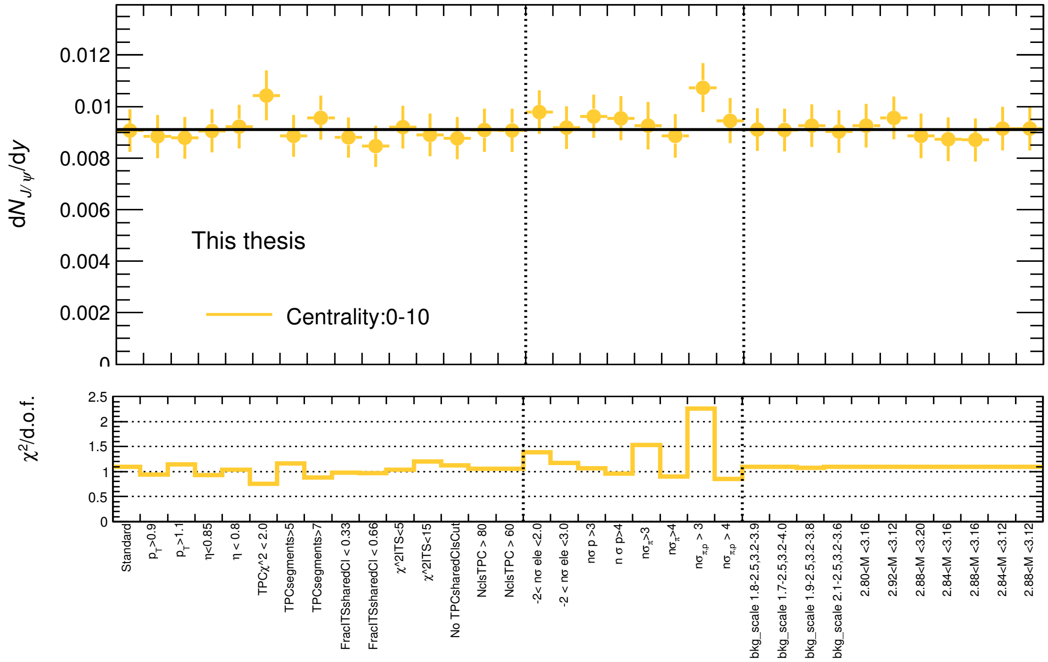

Figure 5.1: Corrected J/ψ yield calculated for each selection criteria variation in the centrality class $0-10\%$. The horizontal black line corresponds to the mean value of all the variations. The vertical lines divide the different selection criteria in tracking, PID and signal extraction.

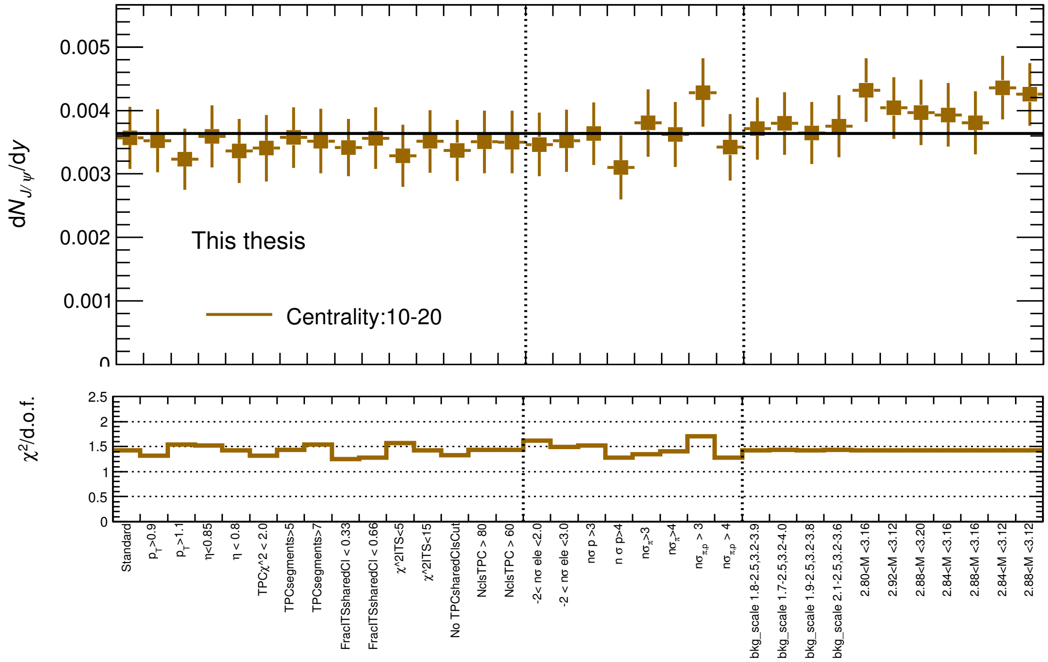

Figure 5.2: Corrected J/ψ yield calculated for each selection criteria variation in the centrality class $10-20\%$. The horizontal black line corresponds to the mean value of all the variations. The vertical lines divide the different selection criteria in tracking, PID and signal extraction.

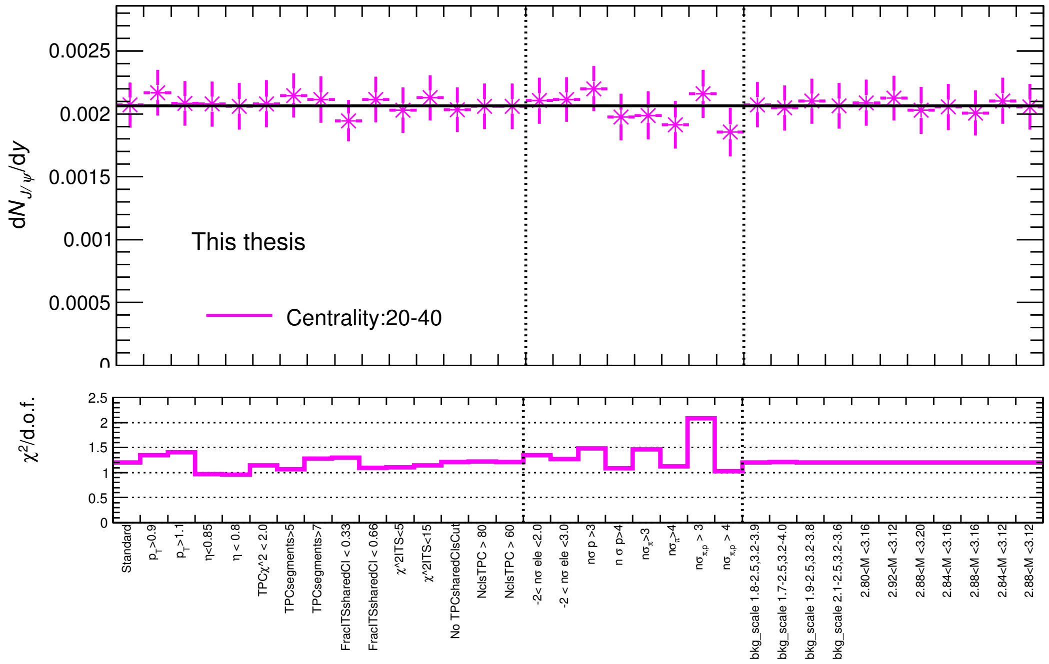

Figure 5.3: Corrected J/ψ yield calculated for each selection criteria variation in the centrality class $20-40\%$. The horizontal black line corresponds to the mean value of all the variations. The vertical lines divide the different selection criteria in tracking, PID and signal extraction.

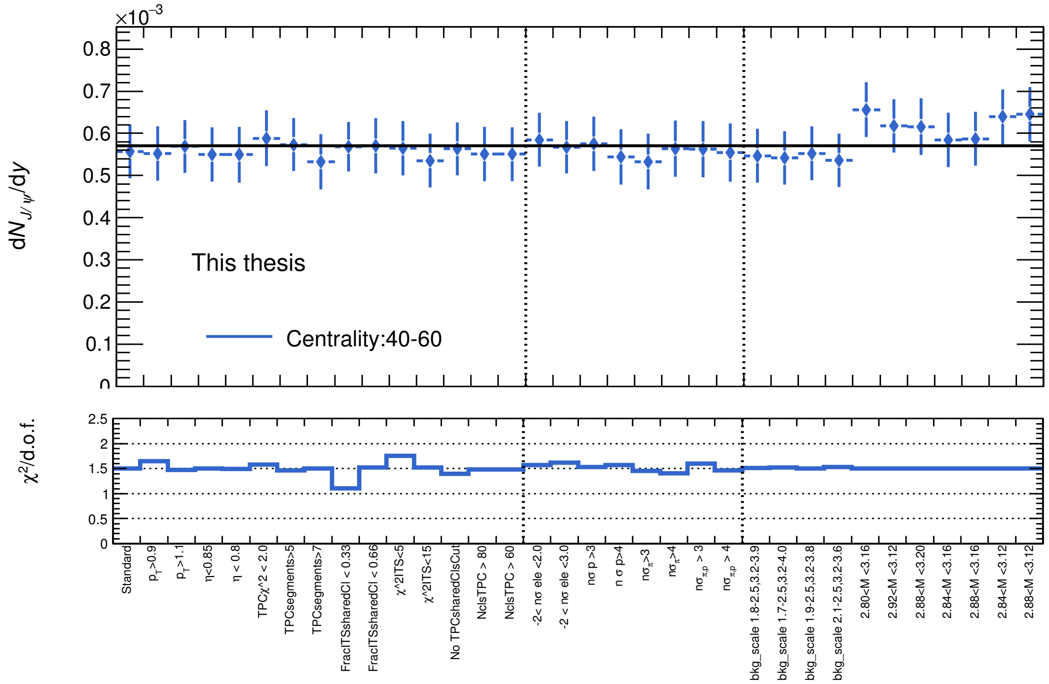

Figure 5.4: Corrected J/ψ yield calculated for each selection criteria variation in the centrality class $40-60\%$. The horizontal black line corresponds to the mean value of all the variations. The vertical lines divide the different selection criteria in tracking, PID and signal extraction.

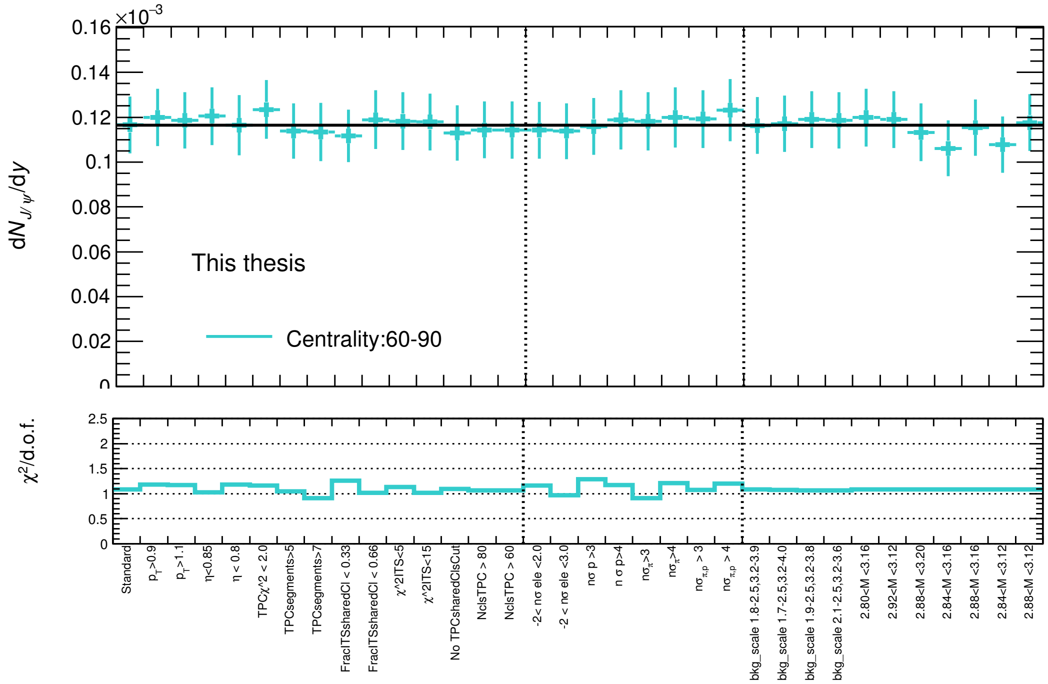

Figure 5.5: Corrected J/ψ yield calculated for each selection criteria variation in the centrality class $60-90\%$. The horizontal black line corresponds to the mean value of all the variations. The vertical lines divide the different selection criteria in tracking, PID and signal extraction.

5.3.2 Systematic uncertainties on the p_{T}-differential analysis

In the same way the p_{T}-differential J/ψ corrected yield ($\mathrm{d}^2N_{J/\psi}/\mathrm{d}y\mathrm{d}p_T$) is calculated according to Eq. 4.13 for each tracking, PID and signal extraction variation listed in Tables 5.1 to 5.3, respectively. The corrected J/ψ yields are measured in each p_{T} interval. Figures 5.6 to 5.9 show the variations corresponding to the J/ψ corrected yield in the different p_{T} intervals and centralities. The variations are in agreement within statistical uncertainties, and the mean is taken as the central value of the result.

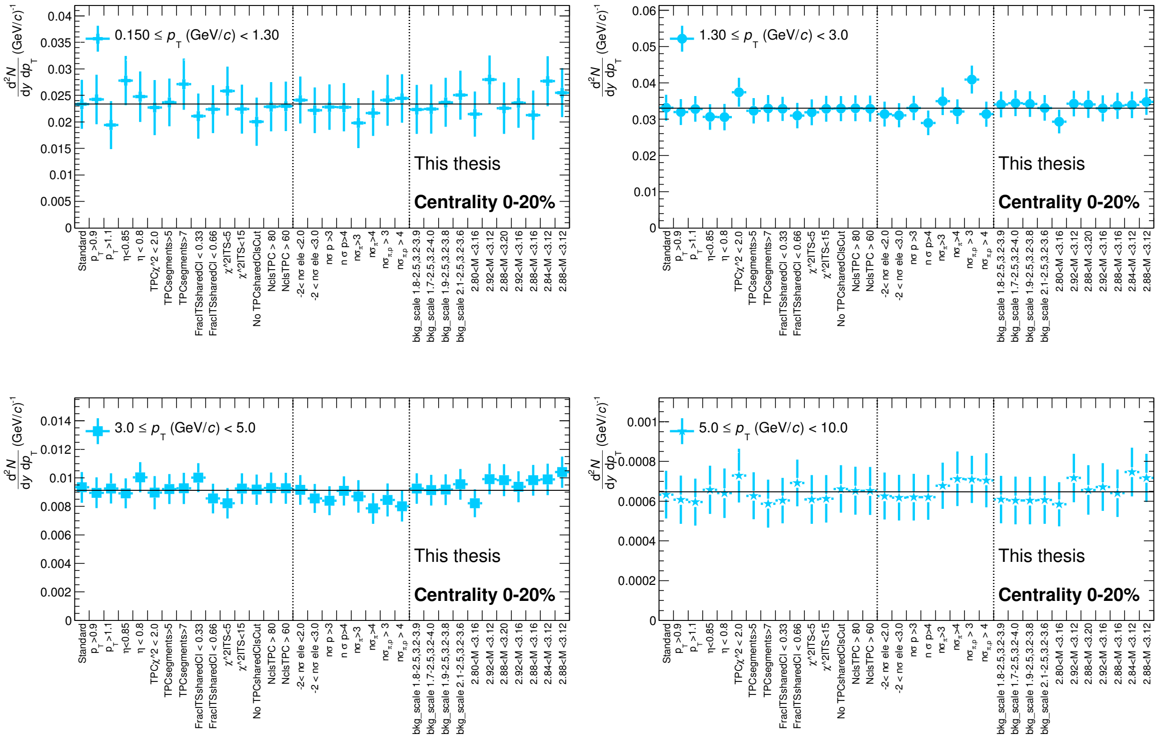

Figure 5.6: Corrected p_{T}-differential inclusive J/ψ yield obtained for each of the selection criteria variations in the centrality class $0-20\%$. Each panel corresponds to a different p_{T} bin. Discussion is given in the text.

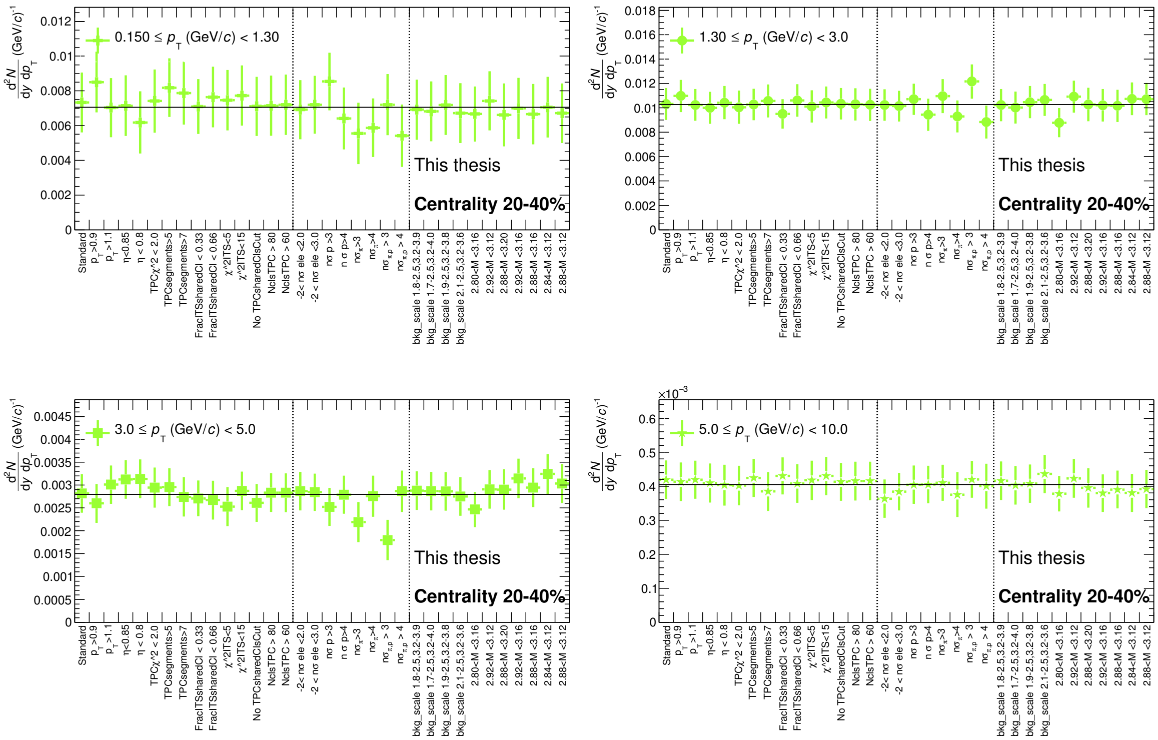

Figure 5.7: Corrected p_{T}-differential inclusive J/ψ yield obtained for each of the selection criteria variations in the centrality class $20-40\%$. Each panel corresponds to a different p_{T} bin. Discussion is given in the text.

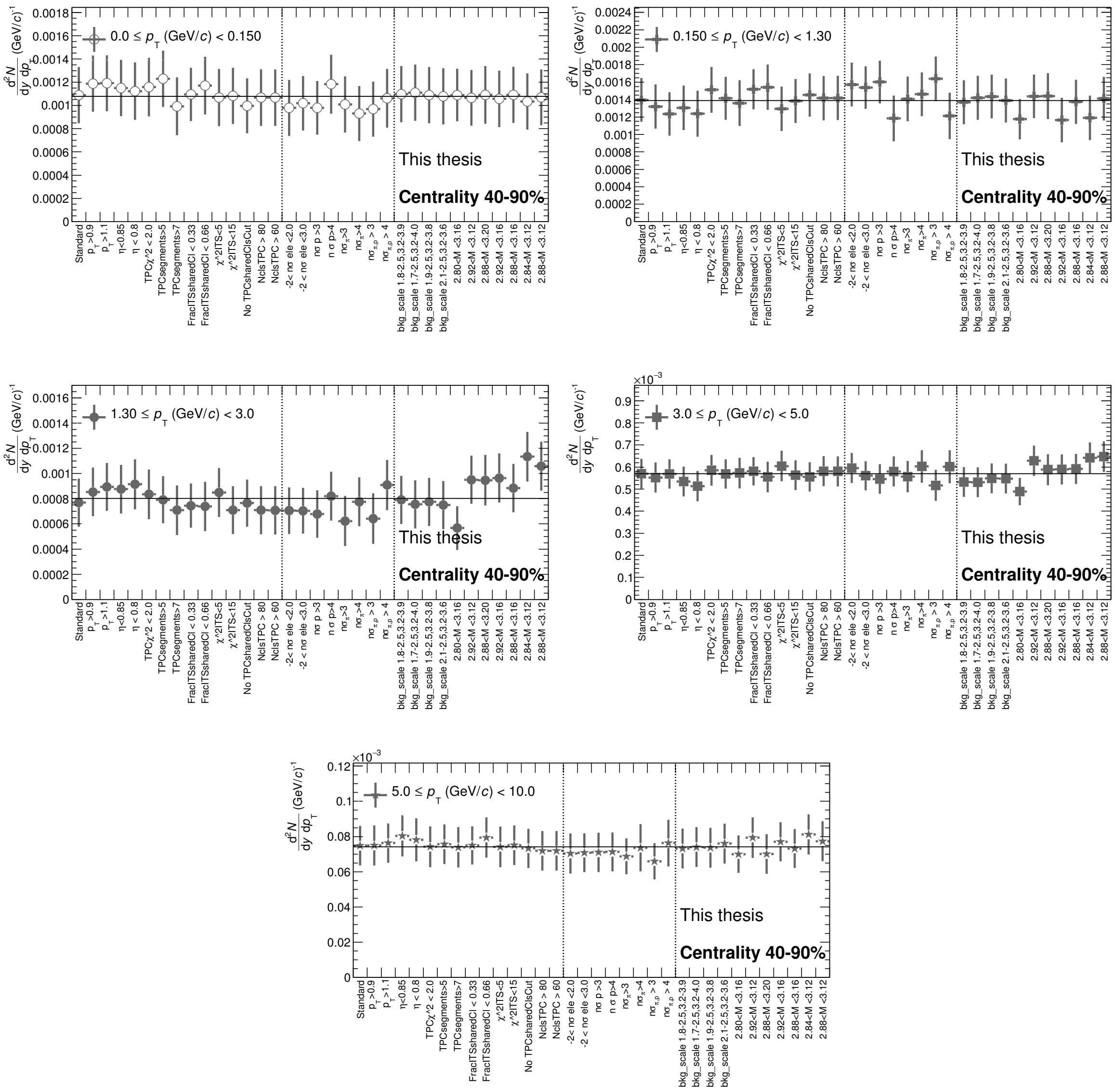

Figure 5.8: Corrected p_T-differential inclusive J/ψ yield obtained for each of the selection criteria variations in the centrality class $40-90\%$. Each panel corresponds to a different p_T bin. Discussion is given in the text.

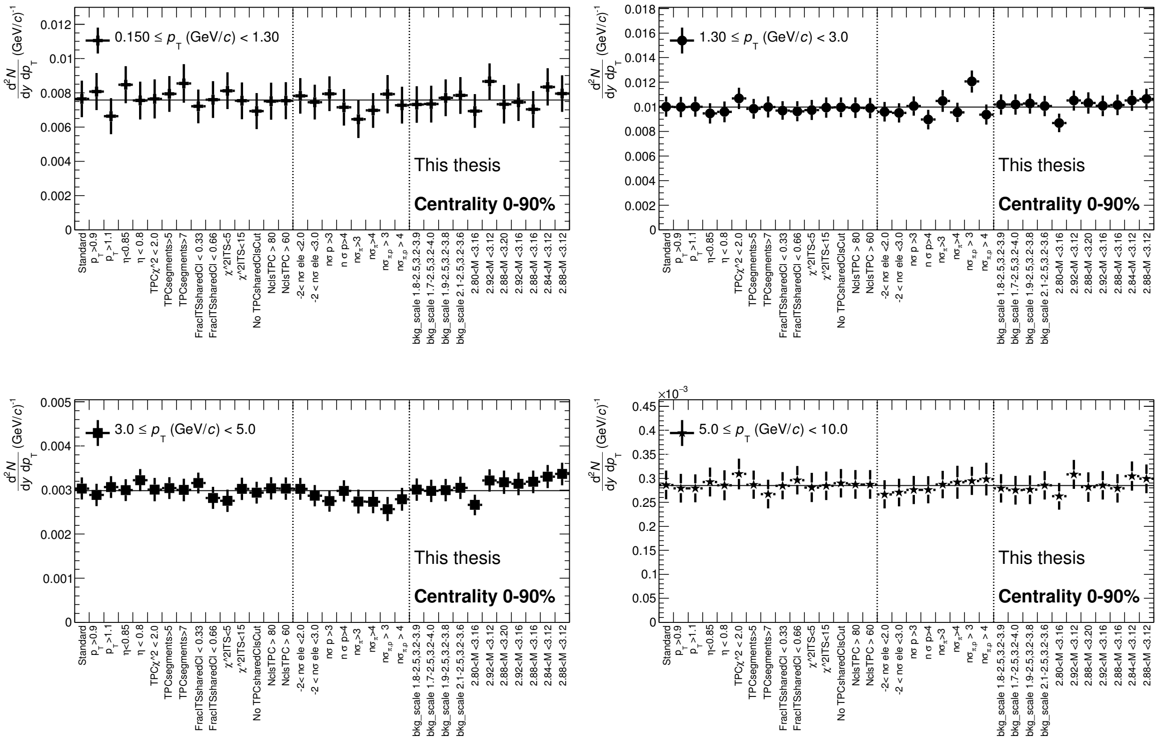

Figure 5.9: Corrected p_T-differential inclusive J/ψ yield obtained for each of the selection criteria variations in the centrality class $0-90\%$. Each panel corresponds to a different p_T bin. Discussion is given in the text.

5.4 Systematic uncertainties considerations

As the corrected inclusive J/ψ yield has relatively large statistical uncertainties of approximately $10-20\%$, some of the variations calculated in the previous section may not be necessarily considered as a systematic uncertainty, but a statistical fluctuation. The Barlow's criterion [148] is applied in order to avoid including statistical fluctuations in the estimation of the systematic uncertainties.

The difference between the mean value and each variation (i) is calculated as $\Delta_i = \frac{\mathrm{d}N_{\mathrm{J}/\psi,i}}{\mathrm{d}y} - \langle \frac{\mathrm{d}N_{\mathrm{J}/\psi}}{\mathrm{d}y} \rangle$ and $\frac{\mathrm{d}^2 N_{\mathrm{J}/\psi,i}}{\mathrm{d}y\mathrm{d}p_{\mathrm{T}}} - \langle \frac{\mathrm{d}^2 N_{\mathrm{J}/\psi}}{\mathrm{d}y\mathrm{d}p_{\mathrm{T}}} \rangle$. The systematic deviation ($\sigma_{\mathrm{dev,i}}$) is computed as follows:

$$\sigma_{\mathrm{dev,i}} = \sqrt{\sigma^2_{\mathrm{mean}} - \sigma^2_{\mathrm{i}}}. \tag{5.1}$$

where σ_{mean} and σ_{i} correspond to the statistical error on the mean and the statistical error of the variation i. Only variations satisfying $\Delta_i/\sigma_{\mathrm{dev,i}} > 1$ are taken into account in the systematic uncertainties. Figure 5.10 shows the systematic deviation values from the mean (in percentage values) for the different variations after the Barlow's criterion is applied. The percentage value RMS of each contribution is shown in the horizontal bands. The relative uncertainty of the contribution due to tracking, PID and signal extraction is summarized in Table 5.4 and 5.5 for the p_{T}-integrated and the p_{T}-dependent analysis, respectively.

The systematic uncertainties show slight centrality dependence for the tracking in the most central events. This is mainly dominated by the selection requirement on the TPC$\chi^2/n_{cls} < 2.5$. This variable has a strong centrality dependence, the selection increases the systematic uncertainty in the most central events due to the difference between data and MC.

Systematic uncertainties on the p_{T}-integrated J/ψ yield (%)					
Source	**Centrality** (%)				
	0-10	**10-20**	**20-40**	**40-60**	**60-90**
Track (Trk.)	6.7	2.7	3.2	2.3	3.4
PID	4.0	4.2	5.8	3.4	3.8
Signal extraction (S.E.)	3.8	6.0	2.0	6.7	4.3
Quadratic sum	8.7	7.8	6.9	7.9	6.7

Table 5.4: Systematic uncertainties due to tracking, PID, and signal extraction computed for the p_{T}-integrated inclusive J/ψ yield in different centralities. The total represents the quadratic sum of the different sources of systematic uncertainties.

Relative systematic uncertainties on the p_{T}-differential J/ψ yield (%)												
p_{T} **(GeV/c)**	**Centrality** (%)											
	0-20			**20-40**			**40-90**			**0-90**		
	Trk.	PID	S.E.	Trk.	PID	S.E.	Trk.	PID	S.E.	Trk.	PID	S.E.
$0.00 < p_{\mathrm{T}} < 0.15$	-	-	-	-	-	-	7.0	6.2	1.8	-	-	-
$0.15 < p_{\mathrm{T}} < 1.30$	12.4	8.1	10.8	9.1	16.2	3.7	12.1	7.8	8.7	9.0	6.3	5.2
$1.30 < p_{\mathrm{T}} < 3.00$	7.2	5.8	4.9	4.5	8.1	6.2	9.9	12.0	19.8	4.4	4.5	5.2
$3.00 < p_{\mathrm{T}} < 5.00$	5.9	3.5	6.2	6.9	9.9	7.2	4.9	3.7	8.4	4.3	1.8	6.5
$5.00 < p_{\mathrm{T}} < 10.0$	5.9	6.1	3.5	3.0	2.5	5.1	4.4	1.2	5.4	4.3	1.3	5.3

Table 5.5: Systematic uncertainties due to tracking, PID, and signal extraction computed for the p_{T}- differential inclusive J/ψ yield in different p_{T} intervals and centralities.

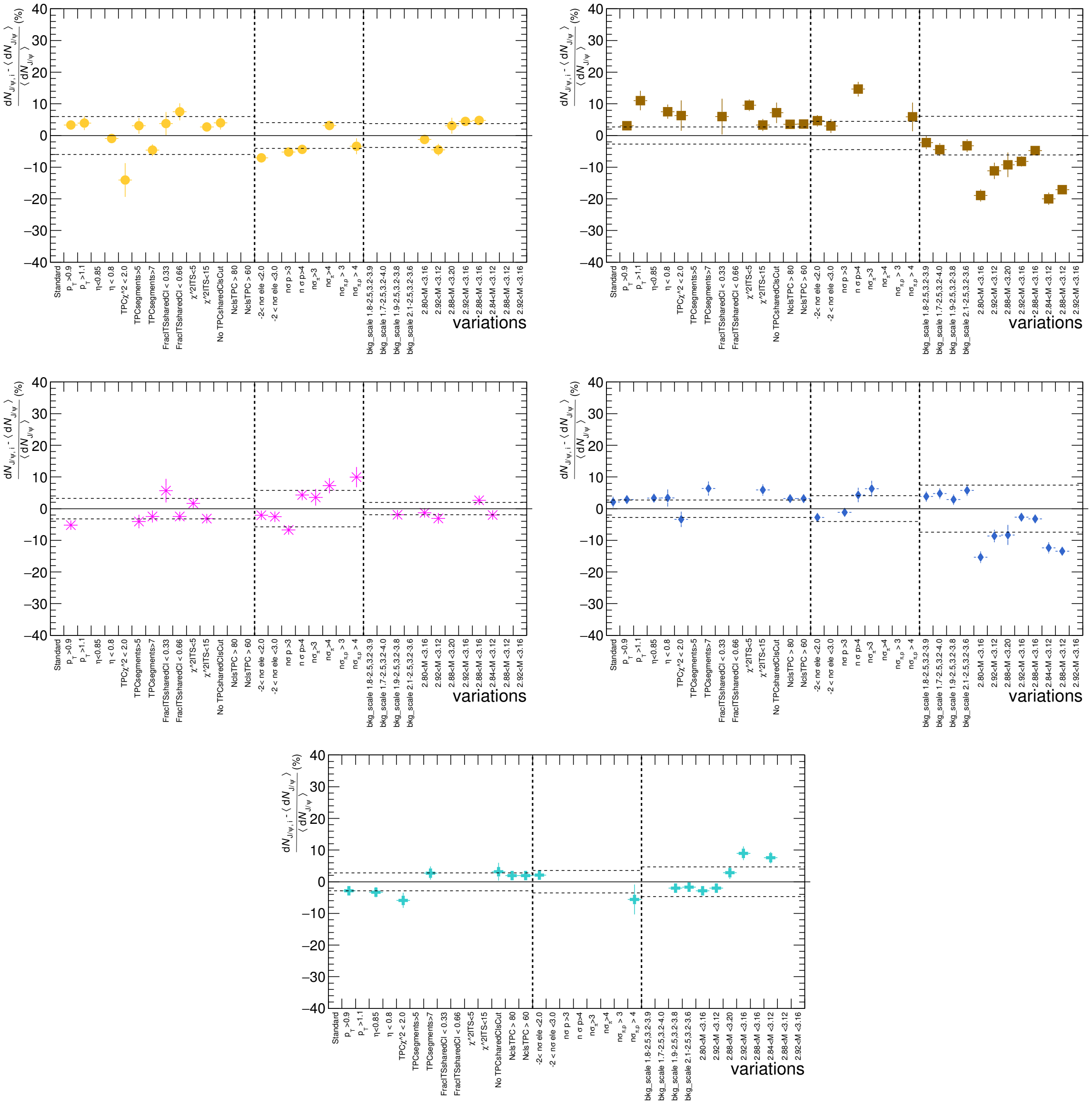

Figure 5.10: Difference with respect to the mean for each of the variations. Only the variation after applying Barlow's are shown. The corresponding RMS of each of contribution: tracking, PID and signal extraction is indicated with a band in the corresponding variations region.

5.5 Monte Carlo input kinematics

The value of the *Acc.* × $Eff.$ correction factor depends on the Monte Carlo generated J/ψ p_{T} spectrum. Since the spectrum is not currently measured with sufficient precision down to zero p_{T} in Pb–Pb collisions, a systematic uncertainty is assigned. This is evaluated applying the same re-weighting procedure to the input J/ψ p_{T} spectrum (see Section 4.6.3), varying the function used to re-weight within reasonable limits.

J/ψ spectrum fit

The J/ψ p_{T} spectrum used as input for the efficiency calculation is re-weighted with the fit of the J/ψ measurement at forward rapidity in the respective centrality class, as explained in Section 4.6.3. The default fit takes into account the statistical and systematic uncertainties. The parameters are simultaneously varied with a Gaussian probability centered at the default parameter value and with a width equal to the parameter uncertainty. The process is repeated 1000 times and the weighted acceptance times efficiency is computed with the new values of the fit parameters. An example for the most central collisions (0−10%) of all the possible variations of the fit to the J/ψ measurement at forward rapidity is shown in Figure 5.11 (Left). The corresponding efficiencies computed with the variations are shown in Figure 5.11 (Right). The maximum deviation observed over all the different centralities corresponds to 1% for the p_{T} integrated case, and 4% in the highest p_{T} bin in the most central events. The systematic uncertainties due to the input Monte Carlo p_{T} shape obtained are summarized in Table 5.6.

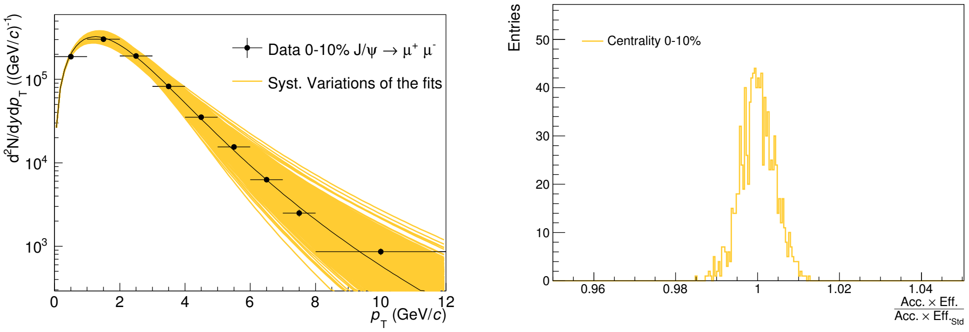

Figure 5.11: Left: Fit variations to the J/ψ spectrum measurement at forward rapidity in the centrality 0−10%. Right: Distribution of the ratio of the *Acc.* × *Eff.* obtained with each fit variation with respect to the efficiency with the default values.

Relative systematic uncertainties due to the MC input p_{T} shape (%)						
p_{T}-dependent					p_{T}-integrated	
p_{T} **(GeV/c)**	**0-20**	**20-40**	**40-90**	**0-90**	**Centrality (%)**	**Uncertainty (%)**
0.00< p_{T} < 0.15	-	-	2.0	-	0-10	1.0
0.15< p_{T} < 1.3	1.0	1.0	1.5	1.5	10-20	1.0
1.30< p_{T} < 3.0	1.0	1.0	1.0	1.0	20-40	1.0
3.0< p_{T} < 5.0	1.0	1.0	1.5	1.5	40-60	1.0
5.0< p_{T} < 10.0	4.0	1.0	2.0	2.0	60-90	1.0

Table 5.6: Relative systematic uncertainties due to MC input p_{T} spectrum.

Prompt and non-prompt J/ψ production

The Monte Carlo production includes prompt and non-prompt J/ψ injected signals (see Section 4.6.2), with different p_{T} distributions. The *Acc.* × *Eff.* is evaluated using the inclusive, prompt and non-prompt input distributions. The values are shown in Figure 5.12. Note that the re-weighting procedure is performed with the inclusive spectrum measurement at forward rapidity. To be entirely consistent, the re-weighting procedure should be applied using prompt and non-prompt measurements. However, as there is no measurement of the prompt and non-prompt production of J/ψ down to zero p_{T} available in Pb–Pb collisions and considering that the maximum effect is at the few percentage level, effects due to this separation are neglected. The uncertainty added for all the centralities due to the two effects explained in this section corresponds to 2%.

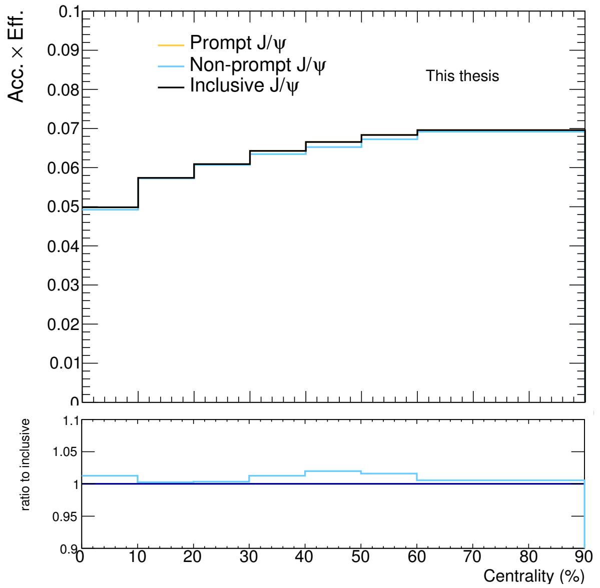

Figure 5.12: Values of $Acc. \times Eff.$ using the input shape of the prompt (blue) and non-prompt (yellow) J/ψ productions. The ratio of each productions with respect to the inclusive production (black) is shown in the lower panel.

5.6 Nuclear overlap factor $\langle T_{\mathrm{AA}} \rangle$

The systematic uncertainties on the nuclear overlap factor arise from the procedure to estimate the centrality (see Section 3.5). The systematic uncertainties are taken from Ref. [118]. The different uncertainties are shown in Table 3.1. The systematic uncertainties on the mean values are obtained by varying the parameters of the Glauber model independently within their estimated uncertainties [118].

5.7 Summary of systematic uncertainties

Systematic uncertainties on the p_{T}-integrated J/ψ R_{AA}

The total systematic uncertainty on the J/ψ R_{AA} (see Eq. 4.14a) is obtained adding the different uncorrelated sources listed in the following.

- The systematic uncertainty due to the tracking, PID, and signal extraction (summarized in Table 5.4),
- The systematic uncertainty due to the MC input,
- The systematic uncertainty on the nuclear overlap function ($\langle T_{\mathrm{AA}} \rangle$) varies from 3% in the most central to 6% in the most peripheral events (see Table 3.1), and is added to each centrality point.
- The uncertainty due to the J/ψ cross-section ($\mathrm{d}\sigma^{\mathrm{pp}}_{\mathrm{J}/\psi}/\mathrm{d}y$) in pp collisions obtained with the interpolation procedure.

The values are summarized in Table 5.7. The total systematic uncertainty is obtained by adding in quadrature all the different sources. The uncertainty due to the $\mathrm{d}\sigma^{\mathrm{pp}}_{\mathrm{J}/\psi}/\mathrm{d}y$ accounting for 16.66% is indicated separately in order to single out the uncertainty due to the pp reference.

Systematic uncertainties on the p_{T}-integrated J/ψ R_{AA} (%)					
Source	**Centrality**				
	0-10	**10-20**	**20-40**	**40-60**	**60-90**
Track/ PID / Signal Extraction	8.7	7.8	6.9	7.9	6.7
MC input	2.2				
T_{AA}	3.3	3.2	3.3	5.7	6.0
Total	9.5	8.7	7.9	9.9	9.2

Table 5.7: Summary of relative systematic uncertainties computed for the p_{T}-integrated inclusive J/ψ R_{AA} in Pb–Pb collisions in different centralities. The uncertainty due to the pp reference is considered in addition to the ones of the list.

Systematic uncertainties on the J/ψ p_{T} spectrum

The total systematic uncertainties on the J/ψ p_{T} spectrum (see Eq. 4.14a) is obtained adding the different uncorrelated sources listed in the following:

- The systematic uncertainty due to the tracking, PID, and signal extraction (summarized in Table 5.5),
- The systematic uncertainty due to the MC input shape (summarized in Table 5.6),
- The relative uncertainty due to the branching ratio corresponding to 0.5% [8].

The global uncorrelated uncertainty values of the inclusive J/ψ corrected yield as a function of p_{T} are summarized in Table 5.8.

Relative systematic uncertainties on the J/ψ p_{T} spectrum (%)				
p_{T} interval (GeV/c)	**Centrality (%)**			
	0-20	**20-40**	**40-90**	**0-90**
$0.00 < p_{\mathrm{T}} < 0.15$	-	-	9.7	-
$0.15 < p_{\mathrm{T}} < 1.30$	18.4	19.0	16.9	12.0
$1.30 < p_{\mathrm{T}} < 3.00$	10.5	11.2	25.2	8.4
$3.00 < p_{\mathrm{T}} < 5.00$	9.3	14.1	10.6	8.2
$5.00 < p_{\mathrm{T}} < 10.00$	12.2	6.7	7.3	7.2

Table 5.8: Total systematic uncertainties values in each p_{T} interval.

Systematic uncertainties on the p_{T}-differential J/ψ R_{AA}

The total systematic uncertainties on the J/ψ p_{T} spectrum (see Eq. 4.14a) is obtained adding the different uncorrelated sources listed in the following:

- The systematic uncertainty due to the tracking, PID, and signal extraction (summarized in Table 5.5),
- The systematic uncertainty due to MC input (summarized in Table 5.6).

A global correlated uncertainty for each centrality class is computed adding in quadrature the systematic uncertainty due to the $\langle T_{AA} \rangle$ (see Table 3.1) and the correlated systematic uncertainty due to the pp reference (see Table 4.3). This systematic global uncertainty is shared among all the p_{T} intervals and will be indicated in the boxes around unity in the results presented in the following chapter. The systematic uncertainties on the R_{AA} as a function of p_{T} do not include the branching ratio uncertainty due to its cancellation (see Eq. 4.14).

The final relative systematic uncertainties on the p_{T}-differential J/ψ R_{AA} are summarized in Table 5.9.

Systematic uncertainties on the p_{T}-dependent J/ψ R_{AA} (%)				
p_{T} **(GeV/c)**	**Uncertainties (%)**			
Centrality (%)	**0-20**	**20-40**	**40-90**	**0-90**
$0.0 < p_{\mathrm{T}} < 0.15$	-	-	10.1	-
$0.15 < p_{\mathrm{T}} < 1.3$	19.4	19.9	17.9	14.6
$1.3 < p_{\mathrm{T}} < 3.0$	11.5	12.1	25.7	9.4
$3.0 < p_{\mathrm{T}} < 5.0$	10.7	15.1	11.8	9.7
$5.0 < p_{\mathrm{T}} < 10.0$	16.4	13.5	13.8	13.8
Global Systematic Uncertainty	16.96	16.96	18.13	16.96

Table 5.9: Relative systematic uncertainties on the inclusive J/ψ R_{AA} obtained in each centrality and p_{T} interval.

6

Results

In this chapter the results on the inclusive J/ψ production are presented. The inclusive J/ψ R_{AA} as a function of centrality is presented and compared to models and previous measurements in Section 6.1. The transverse momentum dependence of the inclusive J/ψ production is shown in Section 6.2. The inclusive J/ψ R_{AA} as a function of transverse momentum and comparisons to models are discussed in Section 6.3. The observation of the J/ψ production at very low transverse momentum in peripheral collisions is presented in Section 6.4. Finally a summary of the results is presented in Section 6.5.

6.1 Inclusive J/ψ R_{AA} as a function centrality

The inclusive J/ψ R_{AA} in the rapidity range $|y| < 0.9$ as a function of $\langle N_{part} \rangle$ is shown in Figure 6.1. The measurement is performed in five centrality classes: 0-10%, 10-20%, 20-40%, 40-60% and 60-90%. The boxes indicate the systematic uncertainties while the vertical bars indicate the statistical uncertainties. The uncertainty due to the inclusive J/ψ cross-section in pp collisions is shown with a box around unity. The corresponding R_{AA} values are listed in Table 6.1.

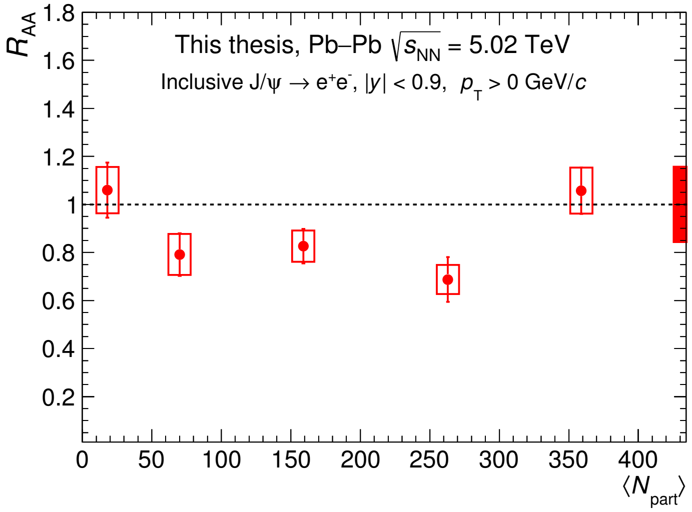

Figure 6.1: Inclusive J/ψ R_{AA} as a function of $\langle N_{part} \rangle$. The boxes indicate the systematic uncertainty while the bars represent the statistical errors. The red box at the right side of the plot indicates the pp cross-section uncertainty of 16.7%.

Inclusive J/ψ R_{AA} values				
Centrality (%)	$\langle N_{\mathrm{part}} \rangle$	R_{AA}	**stat. uncertainty**	**syst. uncertainty**
0-10	359 ± 3.0	1.058	0.096	0.097
10-20	263 ± 3.6	0.688	0.093	0.064
20-40	159.6 ± 2.6	0.827	0.072	0.065
40-60	69.7 ± 1.4	0.792	0.089	0.088
60-90	17.86 ± 0.45	1.060	0.115	0.099

Table 6.1: Inclusive J/ψ R_{AA} in the rapidity range $|y| < 0.9$ with $p_{\mathrm{T}} > 0$ GeV/c. Statistical and systematic uncertainties in the five different centrality categories are also listed. An additional global uncertainty of ±16.6% is added due to the pp reference.

Figure 6.2 shows the inclusive J/ψ R_{AA} compared to measurements at mid-rapidity by PHENIX [81] in Au-Au collisions at $\sqrt{s_{\mathrm{NN}}} = 0.2$ TeV and ALICE [83] in Pb–Pb collisions at $\sqrt{s_{\mathrm{NN}}} = 2.76$ TeV. The most central collisions show an R_{AA} increase with respect to PHENIX measurement. An increase of the R_{AA} towards unity in the most central collisions is observed at $\sqrt{s_{\mathrm{NN}}} = 5.02$ TeV, while the measurement at $\sqrt{s_{\mathrm{NN}}} = 0.2$ TeV shows an opposite behavior decreasing towards most central collisions. Both measurements at LHC energies show a similar flat behavior in the semi-central collisions. An increase with respect to the previous ALICE measurement is also observed.

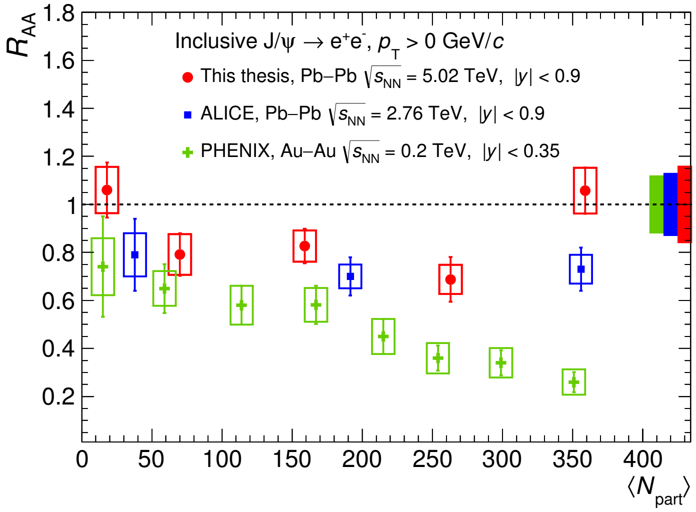

Figure 6.2: Inclusive J/ψ R_{AA} as a function of $\langle N_{part} \rangle$ compared to previous measurement by ALICE [83] at $\sqrt{s_{\mathrm{NN}}} = 2.76$ TeV and PHENIX [81] at $\sqrt{s_{\mathrm{NN}}} = 0.2$ TeV. The behavior observed at different energies towards most central collisions is discussed in the text.

The ratio with respect to the previous ALICE measurement at $\sqrt{s_{\mathrm{NN}}} = 2.76$ TeV is calculated in three different centrality classes as shown in Figure 6.3. The systematic uncertainties are considered as uncorrelated due to the different detector conditions *e.g.* the gas used in the TPC, the space charge distortions and the high interaction rate (see Section 3.4); the uncertainties are thus added in quadrature. The hint of increase in the most central collisions accounts for approximately 45 %. The additional uncertainties due to the pp references prevent to claim a significant increase. The analysis of the 2017 pp reference would allow to decrease this uncertainty significantly, in order to probe what here is shown as an hint of increase.

Figure 6.4 shows the inclusive J/ψ R_{AA} compared to the ALICE measurement at forward-rapidity published in Ref. [149]. A similar flat pattern for $\langle N_{part} \rangle > 40$ is observed in both measurements. A higher measurement at $|y| < 0.9$ is expected with respect to the measurement at forward-rapidity due to the higher charm-quark density which makes the recombination component more important at mid-rapidity. The blue box around the unity represents the global correlated systematic uncertainty of the forward-rapidity measurement, while the red box in the case of mid-rapidity represents the uncertainty due to the pp reference.

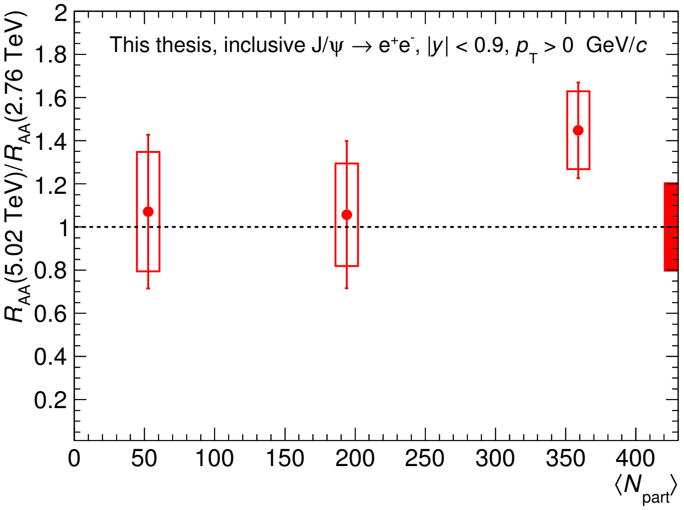

Figure 6.3: Inclusive J/ψ R_{AA} ratio between $\sqrt{s_{\mathrm{NN}}} = 5.02$ and 2.76 TeV as a function of centrality.

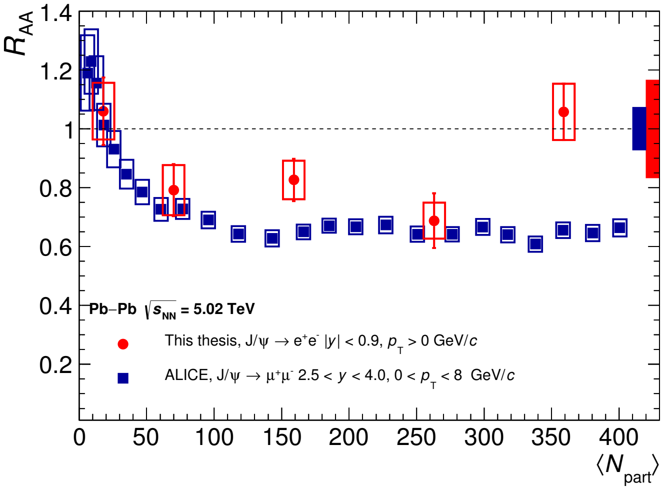

Figure 6.4: Inclusive J/ψ R_{AA} as a function of $\langle N_{part} \rangle$ compared to measurement by ALICE [149] at forward-rapidity.

The most peripheral events contain the highest contribution of the potential J/ψ coherent photo-production (see Section 2.7). The contribution to the hadronic J/ψ production can be removed by selecting J/ψ with $p_{\mathrm{T}} > 150$ MeV/c.

The R_{AA} as a function of $\langle N_{part} \rangle$ including the p_{T} selection above 150 MeV/c is shown in Figure 6.5. A decrease of 2% and 12% on the R_{AA} values for the centralities 40-60% and 60-90% is observed. The effect of the p_{T} selection in semi-central and central events is negligible. The removal of the non-hadronic J/ψ production allows for a fair comparison with the different model calculations, as the potential J/ψ photo-production is not included in the models.

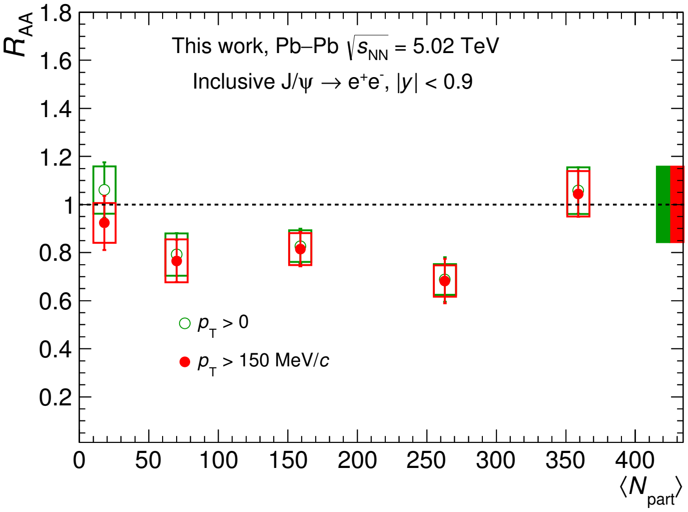

Figure 6.5: Inclusive J/ψ R_{AA} at $\sqrt{s_{\mathrm{NN}}}$ = 5.02 TeV as a function of $\langle N_{part} \rangle$ for p_{T} >0 (green) and p_{T} >150 MeV/c (red). The p_{T} selection removes the potential coherent J/ψ photo-production in peripheral collisions.

6.1.1 Comparison to models

The comparison of the inclusive J/ψ R_{AA} to four different models is shown in Figure 6.6. A brief description of the models and the different input parameters used in the calculations are discussed in the following.

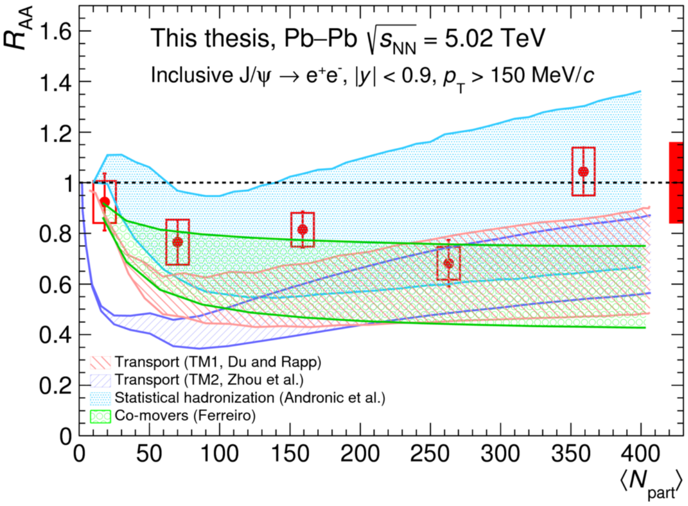

Figure 6.6: Inclusive J/ψ R_{AA} at $\sqrt{s_{\mathrm{NN}}}$ = 5.02 TeV compared to different models. A discussion on the different models is given in the text.

Statistical Hadronization Model (SHM) [60, 150]: In this model, the J/ψ mesons are created together with all other hadrons at chemical freeze-out according to their statistical weights. The $c\bar{c}$ production cross-section per unit of rapidity (d$\sigma_{c\bar{c}}$/dy at $|y| < 0.9$) is taken from the ALICE measurement in pp collisions at $\sqrt{s}$ = 7 TeV [79] and scaled to $\sqrt{s}$ = 5.02 TeV using FONLL calculations [151]. No extra uncertainty is considered due to this scaling. The shadowing factor corresponding to 0.7 is accounted for via the EPS09 NLO parameterization [72]. The d$\sigma_{c\bar{c}}$/dy ($|y| < 0.9$) used by this model after the shadowing correction corresponds to 0.560 ± 0.106 mb.

Transport Model 1 (TM1) [63, 152]: This model is based on the thermal rate equation and takes into account continuous dissociation and regeneration of J/ψ's in the QGP. The d$\sigma_{c\bar{c}}$/dy ($|y| < 0.9$) used corresponds to 0.720 ± 0.130 mb [153]. The shadowing factor considered by this model is 0.7.

Transport Model 2 (TM2) [64]: This model is similar to the TM1. In addition a hydrodynamic description of the medium evolution is implemented. The used d$\sigma_{c\bar{c}}$/dy ($|y| < 0.9$) corresponds to 0.86 mb [154]. The top band corresponds to the case where no shadowing is taken into account. A shadowing factor based on EPS09 NLO [72] accounting for a reduction of 20% for the charm quark cross-section is taken into account in the lower limit band.

Comovers interaction model (CIM) [67]: In this model the J/ψ dissociates via interactions with the comoving medium formed by partons/hadrons, including the recombination of charm quarks pairs to form secondary J/ψ's. This models takes into account the correction due to shadowing effects based on the Glauber-Gribov theory [155], accounting for a centrality-dependent shadowing factor of about 0.6 in the most central cases, and about 0.9 in the most peripheral case. Although the model accounts for shadowing effects, no extra uncertainty is added due to this effect.

Overview of parameters used by the models		
Model	d$\sigma_{c\bar{c}}$/dy ($|y| < 0.9$ (mb))	Shadowing
TM1	0.720 ± 0.130	EPS09 NLO
TM2	0.775 ± 0.085	EPS09 NLO
SHM	0.560 ± 0.106	EPS09 NLO
Comovers	0.555 ± 0.105	Glauber-Gribov theory

Table 6.2: Summary of the input value with uncertainties for the different models.

Table 6.2 summarizes the cross-section values used in the different models. It is important to note that the models use different values for the $d\sigma_{c\bar{c}}/dy$ for their calculations with different uncertainties. The value used by the SHM is defined in the best FONLL fit to the data, while the TM1 and TM2 use values in the upper limit of FONLL calculations. Uniformity in the values used for the different model calculations *e.g.* similar values of $d\sigma_{c\bar{c}}/dy$ and similar shadowing treatment would lead to a more objective comparison. Within the large uncertainties the SHM, TM1 and the CIM models describe the data. The model TM2 fails in the description of the R_{AA} for the 2 most peripheral points. Additional precise measurements of $d\sigma_{c\bar{c}}/dy$ are needed in order to reduce the uncertainties on the models.

6.2 Inclusive J/ψ transverse momentum spectrum

The first measurement at LHC energies of the J/ψ transverse momentum spectrum at mid-rapidity ($|y| < 0.9$) down to 0.15 GeV/c for three different centralities is shown in Figure 6.7. The statistical uncertainties are represented by the vertical bars, while the systematic uncertainties are represented with boxes.

The J/ψ p_{T} spectra are fitted with the function with the phenomenological Equation 4.8, where the parameters, C, p_0, and n are left free. The data is well described by this function in the whole p_{T} range, as shown by the continuous lines in Figure 6.7.

The inclusive J/ψ transverse momentum spectrum in central collisions (0-20%) is compared to the SHM calculation in Figure 6.8. The transverse momentum spectrum of the SHM calculations [156] is based on a collective expansion modelled by a Blast wave function with velocity parameters from hydrodynamical simulations [157] and a corona [1] component in the high p_{T} region. The model is in agreement with the data within the uncertainties. The transport models provide uniquely R_{AA} values (see Section 6.3.2).

---

[1] The corona in a heavy-ion collision refers to the edges region where the density is lower and no QGP formation is expected.

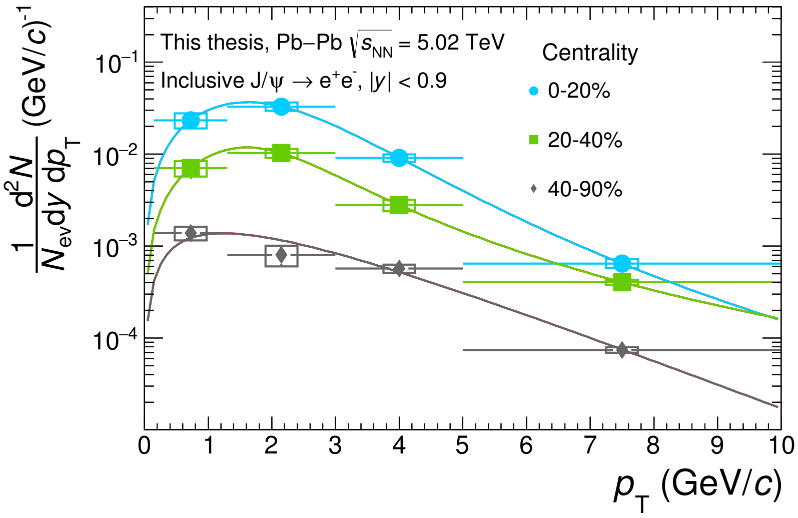

Figure 6.7: J/ψ transverse momentum spectra in the different centralities.

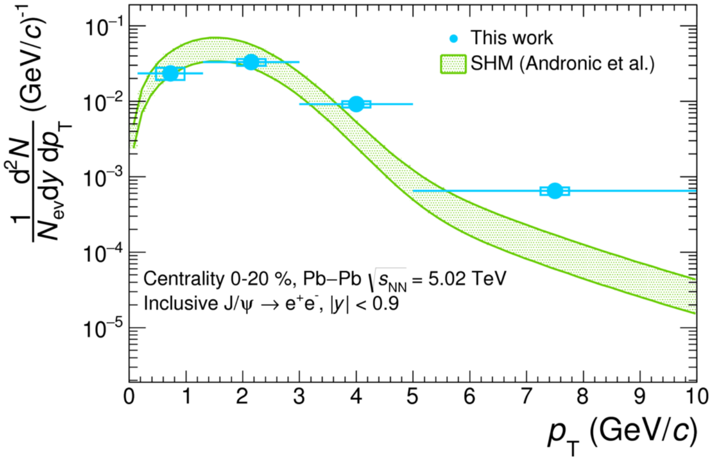

Figure 6.8: Inclusive J/ψ transverse momentum for central collisions (0-20%) compared to statistical model calculations.

6.3 Inclusive J/ψ R_{AA} as a function of transverse momentum

The inclusive J/ψ R_{AA} as a function of transverse momentum for the different centrality classes is shown in Figure 6.9. The p_T dependence of the R_{AA} exhibits a stronger suppression towards high p_T for the most central and semi-central collisions with a value consistent with the unity in the low p_T region. This behavior is in line with (re)combination mechanisms considering that these mechanisms are relevant for the low p_T J/ψ (< 3 GeV/c).

6.3.1 Comparison to other measurements

The p_T-dependence of the inclusive J/ψ R_{AA} in central (0-20%) Pb–Pb collisions at $\sqrt{s_{NN}} = 5.02$ TeV is compared to ALICE measurement at forward rapidity [149] in Figure 6.10. Both measurements show a similar behavior with an increase towards low p_T reaching a similar suppression of about 0.2 at high p_T. At low p_T the R_{AA} at

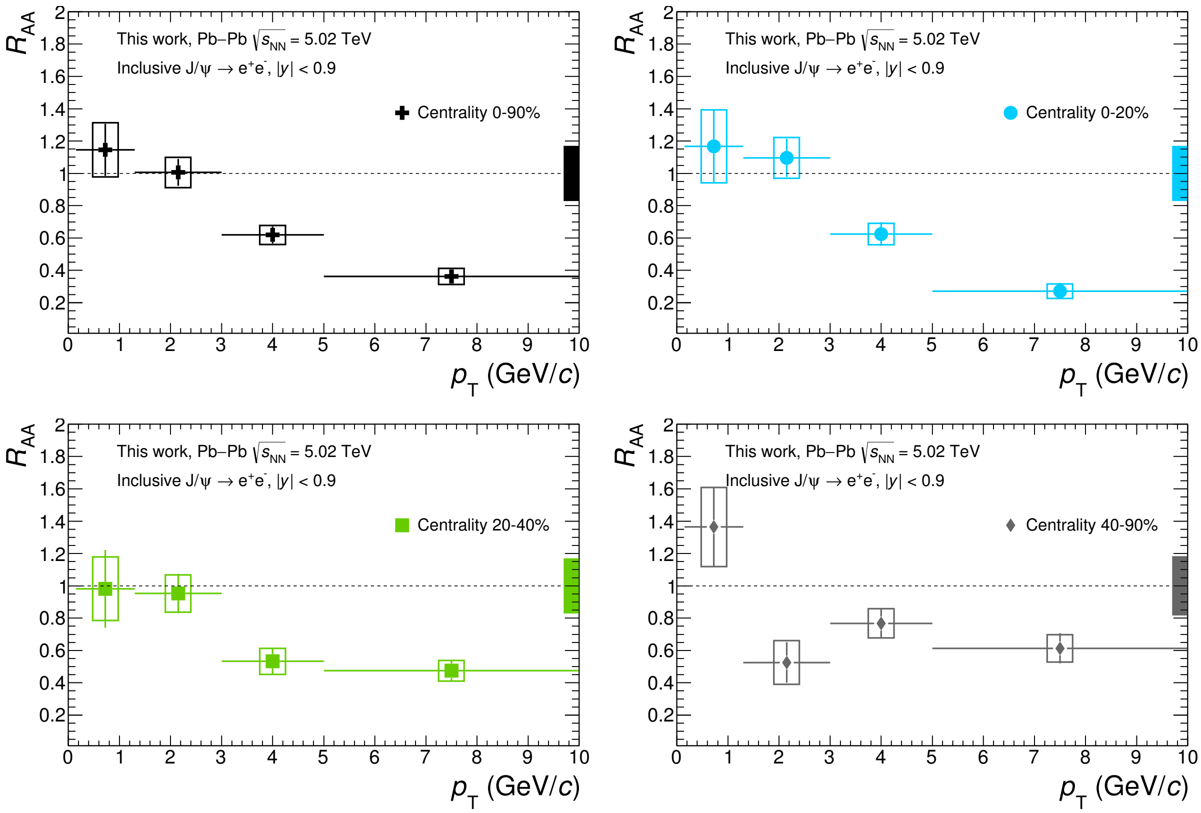

Figure 6.9: Inclusive J/ψ R_{AA} as a function of the transverse momentum in different centralities. The open boxes represent the uncorrelated systematic uncertainty. The correlated systematic uncertainty is indicated in the filled box.

mid-rapidity exhibits higher values, expected due to the higher charm density at mid-rapidity.

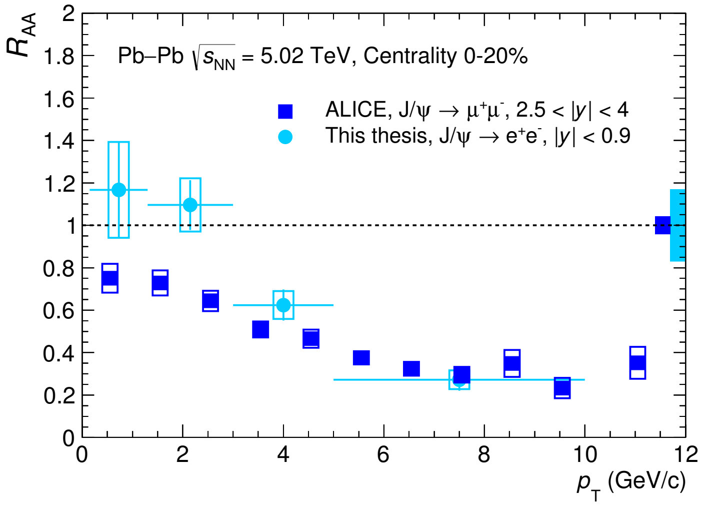

Figure 6.10: Inclusive J/ψ R_{AA} as a function of the transverse momentum compared to the ALICE measurement at forward-rapidity published in Ref. [149]. The open boxes represent the uncorrelated systematic uncertainty. The correlated systematic uncertainty is indicated in the filled box.

Additional evidence in favor of the regeneration scenario at LHC energies is shown in Figure 6.11; the different low p_{T} dependence of the J/ψ R_{AA} at RHIC and at the LHC is clearly observed. In the low p_{T} region ($<$ 3 GeV/c), the R_{AA} at the LHC has a value around one, while the measurements in Au-Au collisions at $\sqrt{s_{\mathrm{NN}}} = 0.2$ TeV show a suppression value of about 0.5.

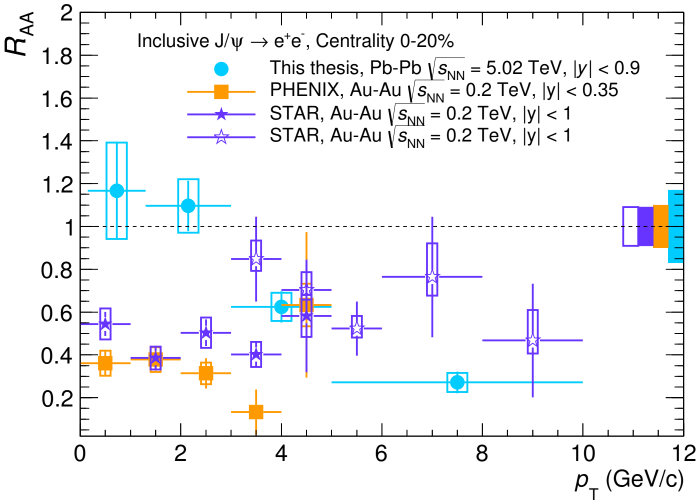

Figure 6.11: Inclusive J/ψ R_{AA} as a function of the transverse momentum measured at mid-rapidity at RHIC and the LHC. Published in Refs [158–160].

6.3.2 Comparison to models

Figure 6.12 shows the measurement of the inclusive J/ψ R_{AA} as a function of transverse momentum in central (0-20%) collisions compared to the SHM and transport model calculations. The TM1 model reproduces a similar trend overall p_{T} range while the SHM underestimate the data at high p_{T}. The $d\sigma_{c\bar{c}}/dy$ and shadowing dominate the uncertainties in the SHM at low p_{T}, while the high p_{T} uncertainties are due to the corona.

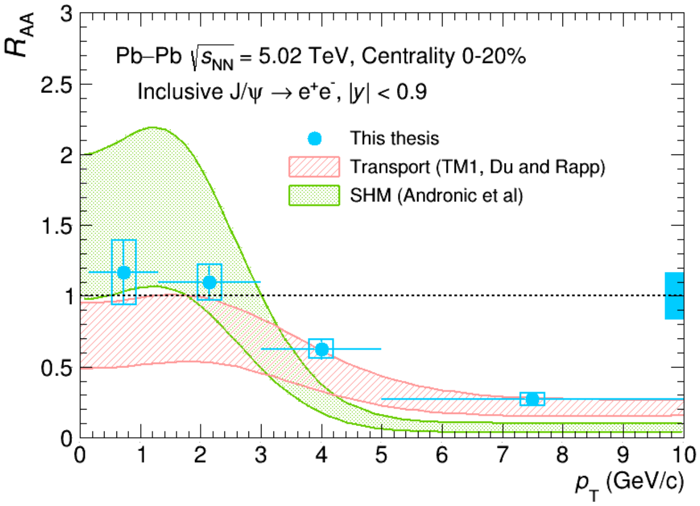

Figure 6.12: Inclusive J/ψ R_{AA} as a function of transverse momentum in central events (0-20%) compared to the transport model TM1 [152] and SHM [150, 156] calculations.

Figure 6.13 (Left) shows the inclusive J/ψ R_{AA} as a function of transverse momentum in semi-central (20-40%) collisions showing a similar behavior also observed for central collisions in agreement with the TM1 model calculation. Figure 6.13 (Right) shows the measurement of the inclusive J/ψ R_AA as a function of transverse momentum compared to theoretical calculations of the models TM1 and TM2 for events in the centrality integrated class (0-90%). The TM1 models shows an agreement within uncertainties, however the model TM2 agrees only in the two low p_T bins and underestimates the data above 3 GeV/c.

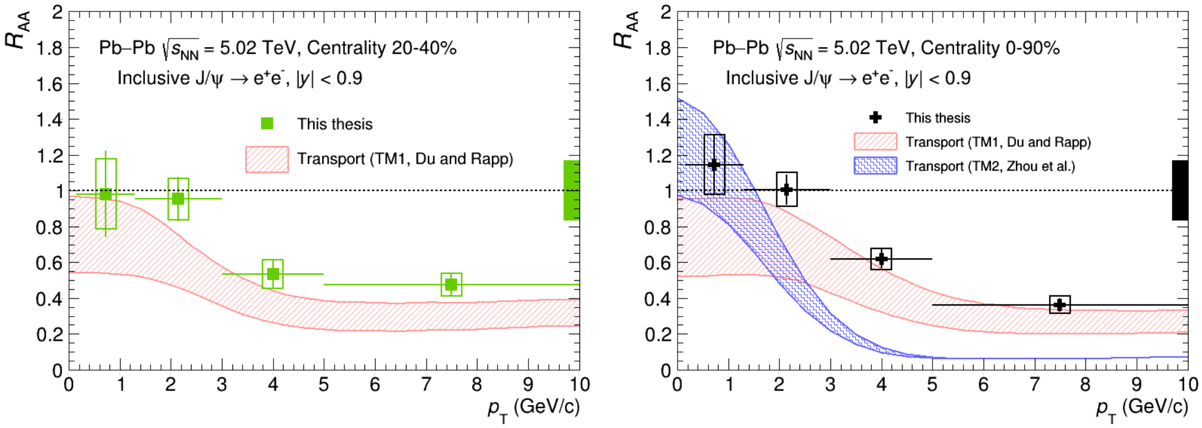

Figure 6.13: Inclusive J/ψ R_AA as a function of the transverse momentum compared to the transport models calculations (TM1 [152], TM2 [64]) in the centrality 0-90%.

6.4 Observation of the very low p_T J/ψ production

The measurement of the J/ψ photo-production cross-section associated with the observed low p_T J/ψ production is outside the scope of this work. However, the R_AA is reported for the most peripheral events (40−90%) in order to confirm the previous observation by ALICE at forward-rapidity [85].

Figure 6.14 shows the inclusive R_AA for the centrality 40−90%, including the p_T range 0−150 MeV/c. The R_AA value for this point corresponds to 9.88 ± 1.97 (stat.) ± 0.91 (syst.) confirming the observation of potential J/ψ photo-production in peripheral collisions.

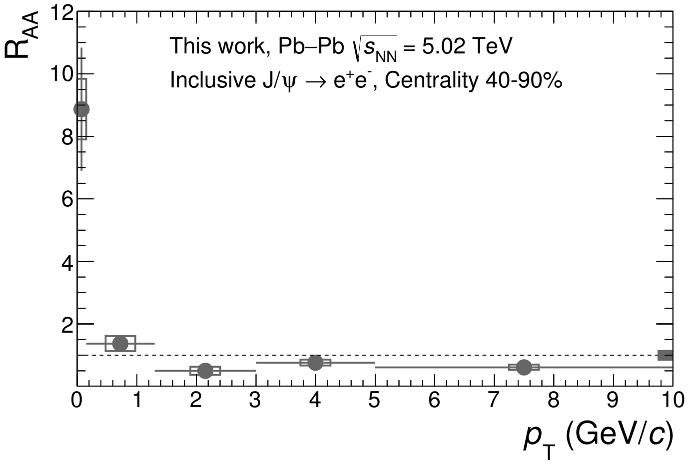

Figure 6.14: Inclusive J/ψ R_AA as a function of the transverse momentum in the most peripheral events including the lowest p_T point.

6.5 Summary and outlook

The results concerning the inclusive J/ψ production in Pb–Pb collisions at $\sqrt{s_{\mathrm{NN}}} = 5.02$ TeV at mid-rapidity ($|y| < 0.9$) are summarized in the following:

- The inclusive J/ψ R_{AA} as a function of centrality shows a similar behavior compared to previous ALICE measurements at half of the collision energy. However, a hint of an increase of approximately 45% in the most central collisions, compatible within uncertainties, is observed. Most of the models describe the data within the large uncertainties, due to uncertainties of the charm quark cross-section and shadowing factors. Nevertheless, the models show already some tension reproducing both the centrality and the p_{T} dependence of the measurement.
- The inclusive J/ψ R_{AA} as a function of transverse momentum exhibits no suppression in the low p_{T} region for central and semi-central events where recombination effects are expected. The J/ψ R_{AA} at high p_{T} exhibits a larger suppression in central collisions than the one observed in peripheral collisions. This is compatible with the energy loss expected in central collisions. The Transport models and the Statistical Hadronization model describe the data qualitatively but show already some tension with the data despite the large uncertainties. The distinction of the two charmonium production mechanisms is not currently possible due to statistical limitations. The distinction between the models will be performed with a measurement of the relative ratio $\psi(2S)$ to J/ψ, where the models have significantly different predictions. [161]

Additional measurements in Pb–Pb collisions at $\sqrt{s_{\mathrm{NN}}} = 5.02$ TeV provide further insights into the charmonium production. The observed significant J/ψ non-zero elliptic flow [162] in semi-central collisions at forward rapidity supports the regeneration mechanism since the J/ψ acquires the flow from the thermalized charm quarks. At mid-rapidity, the current statistics prevents drawing any conclusions.

In 2021, for the start of the high-luminosity LHC, an increase of factor 100 in the event rate together with the ALICE upgrade program will allow for continuous read-out data taking in high luminosity collisions up to 50 kHz for Pb–Pb collisions. High precision measurements on the charmonium production will provide further insights into our current knowledge, and the distinction among the models will be possible.

7

Conclusion

The LHC Run 2 provides an increase in collision energy by a factor two with respect to LHC Run 1 allowing the study of the highest energy densities. The increase in statistics allows studying rare and essential probes such as the charmonium production more differentially with higher accuracy.

In this work, I presented the measurement of the inclusive J/ψ production in Pb–Pb and pp collisions at the highest $\sqrt{s_{\rm NN}} = 5.02$ TeV performed with the ALICE detector in the rapidity region $|y| < 0.9$ down to $p_T = 0$. The measurements of the J/ψ nuclear modification factor as a function of centrality and transverse momentum were shown. After the selection and identification of electron candidates of J/ψ decays, the invariant mass spectrum is calculated, and the raw J/ψ signal extraction is performed and corrected for acceptance times efficiency. An estimation of the systematic uncertainties for all the measurement steps was performed.

The inclusive J/ψ $R_{\rm AA}$ as a function of centrality at $\sqrt{s_{\rm NN}} = 5.02$ TeV exhibits a flat behavior with a hint of an increase in the most central collisions with respect to the previous ALICE measurement at $\sqrt{s_{\rm NN}} = 2.76$ TeV. The inclusive J/ψ $R_{\rm AA}$ in central (0-20%) and semi-central (20-40%) events shows a strong dependence with $p_{\rm T}$, exhibiting a maximum around unity in the low $p_{\rm T}$ region, compatible with no suppression, and decreasing towards high $p_{\rm T}$.

This behavior is different from the one obtained by PHENIX and STAR at lower collision energies, where a significant suppression is observed at low $p_{\rm T}$. This observation gives a clear indication that at the LHC energies the J/ψ at low $p_{\rm T}$ is barely suppressed, in line with the expectations of models including (re)combination.

The different model calculations describe the measurements presented here within uncertainties. Both Transport and the Statistical Hadronization Models describe the behavior of the inclusive J/ψ $R_{\rm AA}$ as a function of $p_{\rm T}$. The maximum value of J/ψ $R_{\rm AA}$ at low $p_{\rm T}$ is expected by the models due to the smaller momentum differences between the charm quarks, favoring the (re)combination mechanism. Although the different models describe the data, they suffer from significant uncertainties due to shadowing and the $c\bar{c}$ production cross-section used in their calculations.

The discrimination between the SHM (re)combination and the Transport Models continuous dissociation and (re)generation will help to understand if the charm is fully thermalized in the medium and hadronize at the same temperature as the light flavor hadrons, or if a partial amount of the initial J/ψ survives the QGP phase. The discernment between these two scenarios will come with a measurement of the ratio ψ(2S) to J/ψ which is currently experimentally limited by large statistical uncertainties.

The inclusive J/ψ cross-section in pp collisions at $\sqrt{s} = 5.02$ TeV, obtained in this work, with approximately 120 million of events collected during 2015 show already a similar overall uncertainty when compared to the interpolation used for the inclusive J/ψ $R_{\rm AA}$ measurement. This is currently our largest uncertainty on the measurement. The addition of the new pp data collected by ALICE at the end of 2017, accounting for ten times more statistics than the results presented here will produce a significant reduction of the uncertainties on the current inclusive J/ψ $R_{\rm AA}$ measurement.

Besides, when analyzing the Pb–Pb collisions in the centrality 40-90%, an excess of J/ψ with very low $p_{\rm T}$ (< 150) MeV/c) was observed for the first time at mid-rapidity. This measurement confirms the presence of potential coherent J/ψ photoproduction in heavy-ion collisions, previously reported by ALICE at forward-rapidity.

A

Inclusive J/ψ production in pp collisions at $\sqrt{s} = 5.02$ TeV

Te measurement of J/ψ production in pp collisions is essential for evaluating the medium effects present in Pb–Pb collisions. The measurement of the p_{T} integrated cross-section in pp collisions at $\sqrt{s} = 5.02$ TeV is presented in this section.

The data sample used for the pp analysis corresponds to the collisions recorded by the ALICE detector during the year 2015. The events were selected using the VO-AND trigger as defined in Section 4.1. Similar to the Pb-Pb analysis, the event selection requires at least one primary vertex contributor in the TPC.

The longitudinal primary vertex distribution (Z_{vtx}) is shown in Figure A.1. The Z_{vtx} distribution is well described by the MC simulations, including the tails of the distribution corresponding to events with a few reconstructed tracks. The event selection is performed in the region $|Z_{\mathrm{vtx}}| < 10$ cm from the nominal interaction point Z_0. The total number of events after the event selection corresponds to 112.5 million of events. The vertex efficiency computed as the fraction of events without a vertex reconstructed accounts for 94.4%.

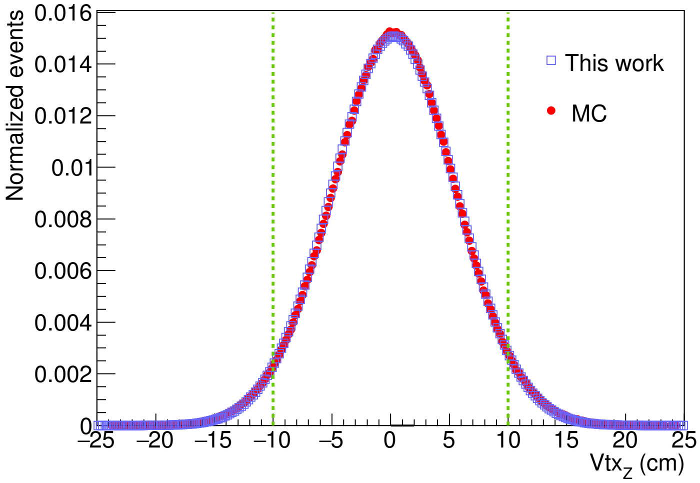

Figure A.1: Primary Z_{vtx} distribution for the events after the trigger selection. The green lines show the excluded events of the analysis.

Track selection

The track and kinematic selection applied in the pp analysis is similar to the one described in Chapter 4 with some slight differences in order to increase the efficiency and reduce the hadron contamination. The track selection criteria is listed in the following:

- **Track requirements:** An ITS and TPC refit is required for all the reconstructed tracks. All tracks are required to have at least 70 out of 159 TPC clusters and a $\chi^2/n_{cls}^{TPC} < 3.0$. A minimum of 6 out of 8 TPC segments is also required. All tracks are required to have a $\chi^2/n_{cls}^{ITS} < 36$ and a fraction of shared clusters < 0.4. SPD any requirement is also applied. The distances of closest approach DCA_{XY} and DCA_{Z} are selected within 3.0 and 1.0 cm respectively. Kink daughters rejection is applied.
- **PID requirements:** The particle identification method relies on the measurement of the specific energy loss on the TPC as well. The electron inclusive selection is performed in the region -2.2 $< TPCn\sigma_e < 3$ .To reduce the hadron contamination on the electron sample, the exclusion of hadrons is applied requiring a $TPCn\sigma_p > 3.5$ and $TPCn\sigma_\pi > 3.5$. Figure A.2 shows the electron after the hadron exclusion cut. The minimum value of 2.2 is selected in order to remove the pion contamination visible in Figure A.2.

  In the region [-3,2.2] the visible pion contamination is removed with the electron inclusion cuts.
- **Kinematic selection:** The electrons are selected in the rapidity range $|\eta| < 0.8$ with a minimum p_{T} of 0.85 GeV/c.

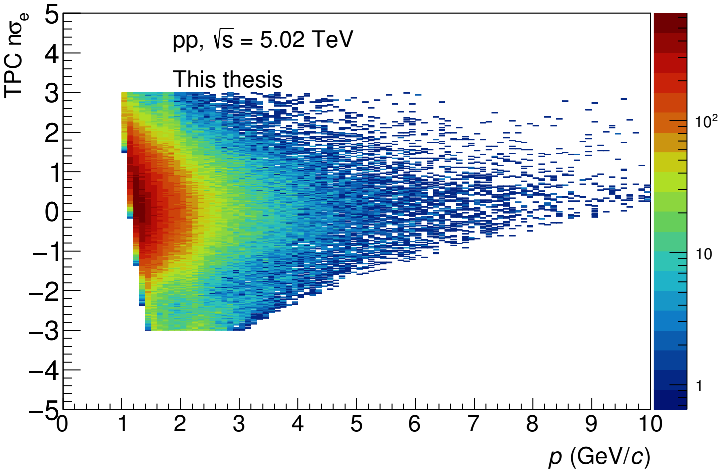

Figure A.2: TPC nσ_e as a function of the momentum at the inner wall of the TPC for electron candidates of J/ψ decays. The distribution is shown in the region.

A.1 Measurement of the inclusive J/ψ yield

The inclusive J/ψ corrected yield is measured as explained in Chapter 4. The small amount of electron candidates of a J/ψ decay in pp collisions is reflected in the low amount of combinatorial background in the invariant mass distribution. This can be observed directly on the signal over background factor observed in the two different colliding systems. The event mixing method classifying the events in four different categories equally distant according to the vtx$_Z$ position in the region [-10−10] cm was used as default to extract the J/ψ signal.

The invariant mass distribution constructed with ULS electron pairs, is shown in the top panel of Figure 4.22. The background produced with the EM method is scaled to match the ULS distribution in two mass ranges: 2.0 $< m_{\mathrm{e^+e^-}} < 2.5$ GeV/c^2 and 3.2 $< m_{\mathrm{e^+e^-}} < 3.7$ GeV/c^2. In contrast to the Pb–Pb analysis the combinatorial background is reduced due to the smaller particle multiplicity in pp. The bottom panel of Figure 4.22 shows the signal after background subtraction. A good agreement of the J/ψ signal expected from MC and the data is observed. The raw yields are extracted by bin counting in the range 2.92 $< m_{\mathrm{e^+e^-}} < 3.16$ GeV/c^2 indicated by the green lines on the figure.

A.1.1 Efficiency

The $Acc \times Eff$ factor is computed with the procedure explained in Section 4.6.3. ALICE measurement in pp collisions at forward-rapidity [149] was used to re-weight the input Monte Carlo transverse momentum spectra. The inclusive J/ψ cross-section was fitted with the function in Equation 4.19. The fitted function is used to re-weight the $Acc \times Eff$ in each p_{T} bin. The value for the $Acc \times Eff$ using the standard selection on the analysis after the re-weight corresponds to 8.22%. The efficiencies are computed for each of the systematic variations that will be explained in the following.

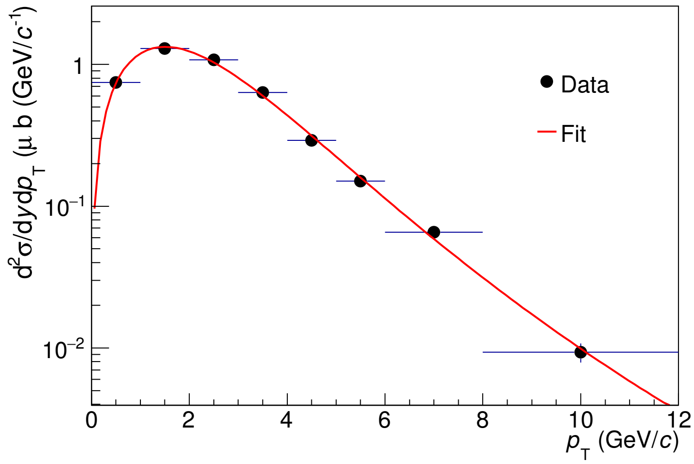

Figure A.3: Fit to the inclusive J/ψ cross-section in pp collisions at $\sqrt{s} = 5.02$ TeV at forward rapidity Published in Ref. [149].

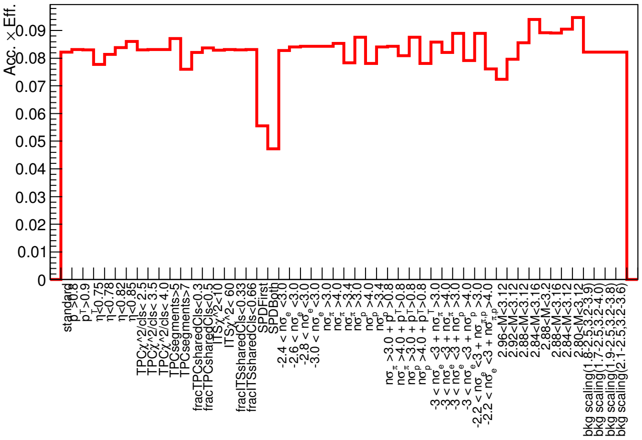

Figure A.4: $Acc. \times Eff.$ for all different systematic variations.

A.2 Systematic uncertainties

The different sources of systematic uncertainties evaluated following the procedure explained in Chapter 5. As the track and PID selections are slightly different compared to the Pb–Pb some additional systematic variations were performed. The systematic variations on the signal extraction, track and PID selections are listed in Tables A.1 to A.3.

The additional combination of the PID and p_{T} selection of the electron candidates of J/ψ decays are studied as systematic uncertainty. A possible systematic arising of the minimum p_{T} selection of the elections and the proton exclusion selection was also considered, in order to account for possible contamination of protons when changing the p_{T} selection. No systematic deviation was observed due to this effect.

Signal extraction parameters		
Parameter	**Standard value (GeV/c^2)**	**Variation (GeV/c^2)**
Signal-background matching range mass	[2.0 - 2.5, 3.2 - 3.7]	[1.8 - 2.5, 3.2 - 3.9] [1.7 - 2.5, 3.2 - 4.0] [1.9 - 2.5, 3.2 - 3.8] [2.1 - 2.5, 3.2 - 3.6]
Signal counting mass window	[2.92 - 3.16]	[2.96 - 3.12] [2.92 - 3.12] [2.88 - 3.12] [2.84 - 3.16] [2.88 - 3.30] [2.88 - 3.16] [2.84 - 3.12] [2.80 - 3.12]

Table A.1: Standard values and variations for the mass window and background scaling region used to evaluate the systematic uncertainties due to signal extraction method.

Track selection variations			
Variable	**Standard selection value**	**Loose variation**	**Tight variation**
$p_{\mathrm{T}\ e^{\pm}}$ (GeV/c)	> 0.85	> 0.8	> 0.9
$\lvert\eta\rvert$	< 0.8	< 0.82, 0.85	< 0.75, 0.78
TPCχ^2/cluster	< 3.0	< 2.5	<3.5
TPC segments	> 6	> 5	> 7
ITS χ^2	< 36	<10	< 60
Frac. ITS$_{shr.cls}$	< 0.4	<0.66	< 0.3
SPD requirement	SPD any	SPD first and SPD both	

Table A.2: Standard values and variations for track selection used to evaluate the systematic uncertainties.

Each of the variations for the track reconstruction and the PID selection is evaluated at data level, extracting the raw number of J/ψ, and at MC level calculating the corresponding value of the $Acc \times Eff$. A summary containing the signal extraction, the signal over background (S/B), the significance on the signal extraction and the $\chi^2/d.o.f.$ of the fit to the data after signal extraction is shown in Figure A.5. The systematic uncertainties arising from the procedure are summarized in Table A.4.

MC input shape

In order to evaluate the impact on the $Acc. \times Eff.$, due to the unknown Monte Carlo input p_{T} shape, the re-weighting efficiency method explained in Section A.1.1 is repeated. This means, the J/ψ measurement at forward rapidity is fitted with Eq. 4.8. The default parameters, used to calculate the efficiency, are randomly varied up to 1 sigma away from the standard value. This is repeated 3000 times and the weighted efficiency calculation is recomputed with the new values of the parameters. All this variations covers the J/ψ measurement at forward rapidity as shown in Figure. A.6.

The different systematic uncertainties in relative values are summarized in Table A.4.

PID selection variations		
Nσ	**Standard selection value**	**Variation**
electron inclusion	-2.2 <Nσ_e < 3	-2.4 <Nσ < 3.0 -2.6 <Nσ < 3.0 -2.8 <Nσ < 3.0 -3.0 <Nσ < 3.0
pion exclusion	Nσ_π > 3.5	Nσ_π > 4.0 Nσ_π > 3.0 Nσ_π > 3.4
proton exclusion	Nσ_p > 3.5	Nσ_p > 4.0 Nσ_p > 3.0 Nσ_p > 3.4
pion exclusion + electron inclusion	Nσ_π > 3.5 + -2.2 <Nσ_e < 3.0	Nσ_π > 3.0 + -2.2 <Nσ_e < 3.0 Nσ_π > 4.0 + -2.2 <Nσ_e < 3.0
proton exclusion + electron inclusion	Nσ_π > 3.5 + -2.2 <Nσ_e < 3.0	Nσ_p > 3.0 + -2.2 <Nσ_e < 3.0 Nσ_p > 4.0 + -2.2 <Nσ_e < 3.0
Track and PID	Nσ_π > 3.5 + p_T > 0.85 GeV/c + Nσ_p > 3.5	Nσ_π > 3.0 + p_T > 0.80 GeV/c Nσ_π > 4.0 + p_T > 0.80 GeV/c Nσ_p > 3.0 + p_T > 0.80 GeV/c Nσ_p > 4.0 + p_T > 0.80 GeV/c

Table A.3: Standard values and variations for PID selection used to evaluate the systematic uncertainties.

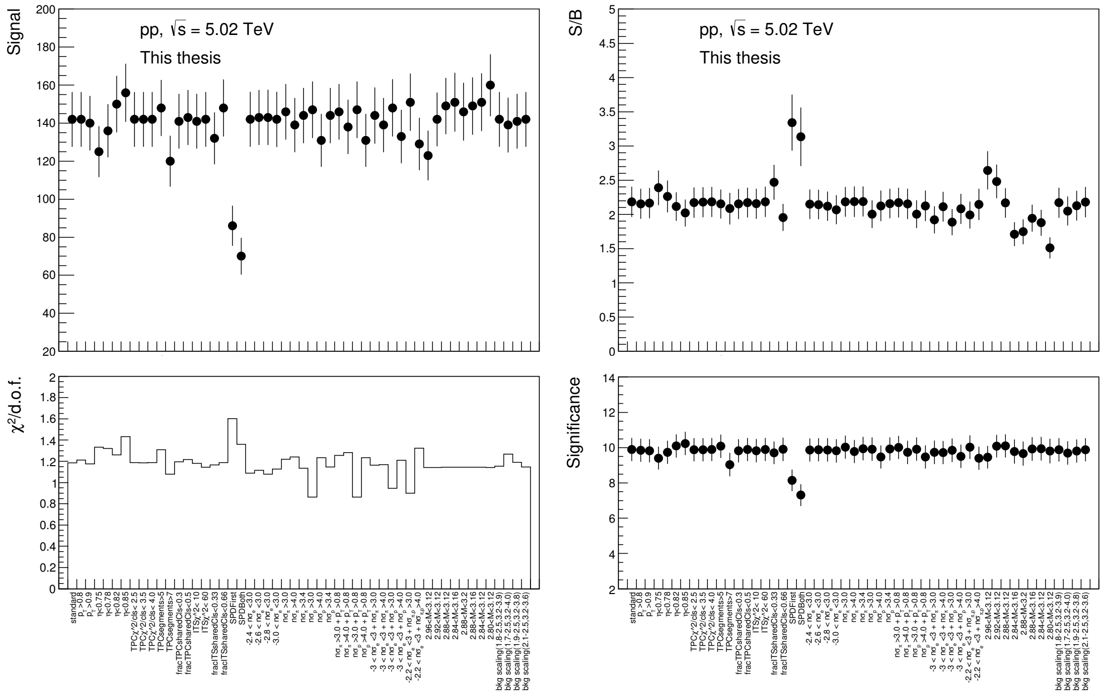

Figure A.5: Summary of the signal extraction parameters. Signal, S/B, significance and $\chi^2/d.o.f.$ for the different track, PID and signal extraction variations.

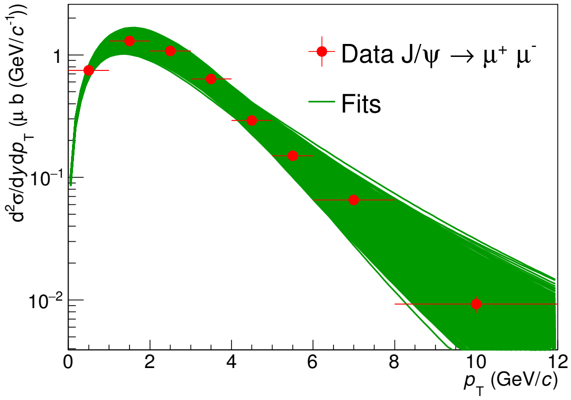

Figure A.6: Systematic evaluation of different fits to the J/ψ cross-section at forward rapidity.

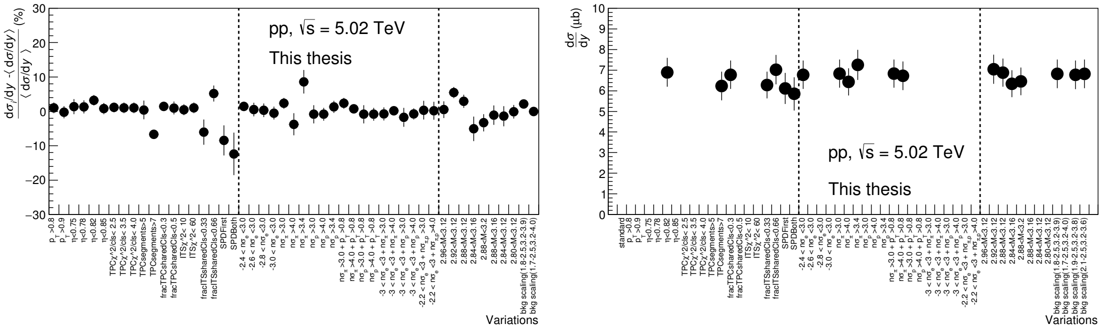

Figure A.7: *Left*: Systematic deviation in percentages for all the variations. The error bar indicates the σ_{dev} obtained with the Barlow's criteria. *Right*: Different values of $d\sigma^{\text{pp}}_{\text{J}/\psi}/dy$ for the systematic variations selected after Barlow's criteria is applied.

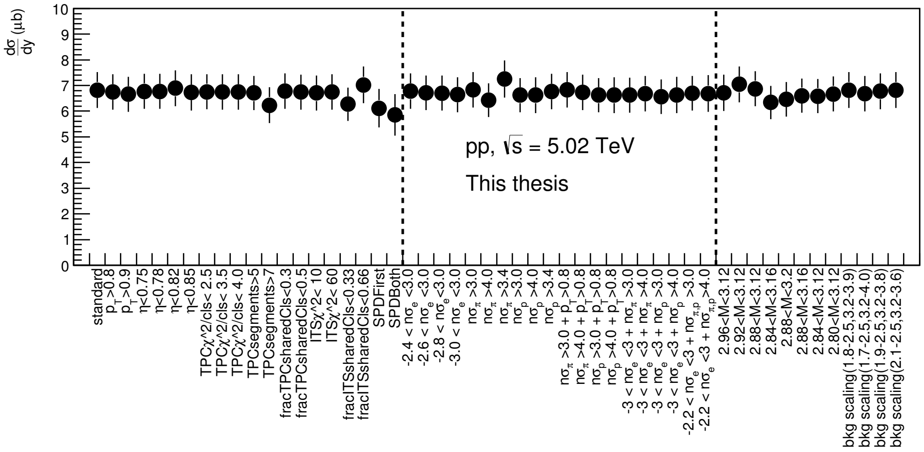

Figure A.8: Uncertainty value assigned as systematic uncertainty

Inclusive J/ψ pp reference at $\sqrt{s} = 5.02$ TeV

The cross-section is obtained using Eq. A.1.

$$\frac{d\sigma^{pp}_{J/\psi}}{dy} = \frac{N_{J/\psi} \cdot \sigma_{V0AND}}{B.R._{J/\psi \to e^+e^-} \cdot Acc \times Eff \cdot N_{ev} \cdot \Delta y} \tag{A.1}$$

The triggered cross-section (σ_{V0AND}) of inelastic processes in pp collisions at $\sqrt{s} = 5.02$ TeV measured by ALICE [163] is 51.2 ± 1.024 mb. The number of events after physics selection and pile-up rejection.The cross-section obtained corresponds to:

$$\frac{d\sigma^{pp}_{J/\psi}}{dy} = 6.80 \pm 0.67(\text{stat.}) \pm 0.53(\text{syst})\mu\text{b}.$$

Systematic uncertainties	
Source	(%)
Tracking	6.02
PID	3.3
Signal ext.	3.1
Luminosity det.	2.1
MC input	1.0
Total	7.88

Table A.4: Summary of different systematic uncertainties of the pp measurement.

Bibliography

[1] S. L. Glashow. "Partial Symmetries of Weak Interactions". *Nucl. Phys.* 22 (1961), pp. 579–588.
[2] S. Weinberg. "A Model of Leptons". *Phys. Rev. Lett.* 19 (21 1967), pp. 1264–1266.
[3] A. Salam. "Weak and Electromagnetic Interactions". *Conf. Proc.* C680519 (1968), pp. 367–377.
[4] CERN 2012-2018 A. Purcell. URL: `https://cds.cern.ch/record/1473657/files/`.
[5] Griffiths D. J. "Introduction to elementary particles; 2nd rev. version". Physics textbook (2008).
[6] D. J. Gross and F. Wilczek. "Ultraviolet Behavior of Nonabelian Gauge Theories". *Phys. Rev. Lett.* 30 (1973), pp. 1343–1346.
[7] H. D. Politzer. "Reliable Perturbative Results for Strong Interactions?" *Phys. Rev. Lett.* 30 (1973), pp. 1346–1349.
[8] C. Patrignani et al. (Particle Data Group). "Review of Particle Physics". *Chin. Phys.* C40.10 (2016), p. 100001.
[9] E. V. Shuryak. "Theory of Hadronic Plasma". *Sov. Phys. JETP* 47 (1978), pp. 212–219.
[10] "FAIR Baseline Technical Report" (2006).
[11] L. Evans and P. Bryant. "LHC Machine". *Journal of Instrumentation* 3.08 (2008), S08001.
[12] M. Harrison, S. Peggs, and T. Roser. "The RHIC Accelerator". *Annual Review of Nuclear and Particle Science* 52.1 (2002), pp. 425–469.
[13] D. J. E. Callaway and A. Rahman. "Lattice gauge theory in the microcanonical ensemble". *Phys. Rev. D* 28 (6 1983), pp. 1506–1514.
[14] Aoki Y. et al. "The QCD transition temperature: results with physical masses in the continuum limit". *Phys. Lett.* B643 (2006), pp. 46–54.
[15] Aoki Y. et al. "The QCD transition temperature: results with physical masses in the continuum limit II." *JHEP* 06 (2009), p. 088.
[16] J. D. Bjorken. "Highly Relativistic Nucleus-Nucleus Collisions: The Central Rapidity Region". *Phys. Rev.* D27 (1983), pp. 140–151.
[17] J. J. Aubert et al. "Experimental Observation of a Heavy Particle J". *Phys. Rev. Lett.* 33 (23 1974), pp. 1404–1406.
[18] J. E. Augustin et al. "Discovery of a Narrow Resonance in e^+e^- Annihilation". *Phys. Rev. Lett.* 33 (23 1974), pp. 1406–1408.
[19] G. S. Abrams et al. "The Discovery of a Second Narrow Resonance in e+ e- Annihilation". *Phys. Rev. Lett.* 33 (1974). [Adv. Exp. Phys.5,150(1976)], pp. 1453–1455.
[20] Appelquist T. and Politzer H. D. "Heavy Quarks and e^+e^- Annihilation". *Phys. Rev. Lett.* 34 (1975), pp. 43–45.
[21] T. Appelquist et al. "Spectroscopy of the New Mesons". 34 (Feb. 1975).
[22] S. Okubo. "Consequences of Quark Line (Okubo-Zweig-Iizuka) Rule". *Phys. Rev.* D16 (1977), pp. 2336–2352.
[23] E. Eichten et al. "Charmonium: The model". *Phys. Rev. D* 17 (11 1978), pp. 3090–3117.
[24] S. Jacobs, M. G. Olsson, and Suchyta C. "Comparing the Schrödinger and spinless Salpeter equations for heavy-quark bound states". *Phys. Rev. D* 33 (11 1986), pp. 3338–3348.
[25] H. Satz. "Colour deconfinement and quarkonium binding". *Journal of Physics G: Nuclear and Particle Physics* 32.3 (2006), R25.

[26] F. Abe et al. (CDF Collaboration). “Production of J/ψ mesons from χ_c meson decays in $p\bar{p}$ collisions at $\sqrt{s} = 1.8$ TeV”. *Phys.Rev.Lett.* 79 (1997), pp. 578–583.

[27] R. Aaij et al. (LHCb Collaboration). “Measurement of the ratio of prompt χ_c to J/ψ in pp collisions at $\sqrt{s} = 7$ TeV”. *Phys.Lett. B* 718 (2012), pp. 431–440.

[28] J. Seixas P. Faccioli C. Lourenco and H.K. Woehri. “Study of J/ψ and χ_c decays as feed-down sources of J/ψ hadro-production”. *JHEP* 10 (2008), p. 004.

[29] B. Abelev et al. (ALICE Collaboration). “Measurement of quarkonium production at forward rapidity in pp collisions at $\sqrt{s} = 7$ TeV”. *Eur. Phys. J. C* 74 (2014), p. 2974.

[30] V. Khachatryan et al. (CMS Collaboration). “Measurement of J/ψ and ψ(2s) prompt double-differential cross sections in pp collisions at $\sqrt{s} = 7$ TeV”. *Phys. Rev. Lett.* 114 (2015), p. 191802.

[31] B. Abelev et al. (ALICE Collaboration). “Inclusive, prompt and non-prompt J/ψ production at mid-rapidity in Pb-Pb collisions at $\sqrt{s_{\mathrm{NN}}} = 2.76$ TeV”. *JHEP* 07 (2012), p. 051.

[32] V. Khachatryan et al. (CMS Collaboration). “Suppression of non-prompt J/ψ, prompt J/ψ and Υ(1S) in Pb–Pb collisions at $\sqrt{s_{\mathrm{NN}}} = 2.76$ TeV”. *JHEP* 05 (2012), p. 063.

[33] G. Aad et al. (ATLAS Collaboration). “Measurement of the differential cross-sections of inclusive, prompt and non-prompt J/ψ production in proton-proton collisions at $\sqrt{s}$= 7 TeV”. *Nucl. Phys. B* 850 (2011), p. 387.

[34] V. Khachatryan et al. (CMS Collaboration). “J/ψ and ψ(2s) production in pp collisions at $\sqrt{s}$= 7 TeV”. *JHEP* 02 (2012), p. 011.

[35] B. Abelev et al. (ALICE Collaboration). “J/ψ and ψ(2s) production in pp collisions at $\sqrt{s}$= 7 TeV”. *JHEP* 11 (2012), p. 065.

[36] D. Acosta et al. (CDF Collaboration). “Measurement of the J/ψ meson and b-hadron production cross sections in $p\bar{p}$ collisions at aaaaaa $\sqrt{s} = 1960$ GeV”. *Phys. Rev. D* 71 (2005), p. 032001.

[37] Michael Krämer. “Quarkonium production at high-energy colliders”. *Prog. Part. Nucl. Phys.* 47 (2001), pp. 141–201.

[38] J.P. Lansberg. *Quarkonium production at high-energy hadron colliders: A Systematic gauge-invariant approach to relativistic effects of J/ψ, ψ' and Υ production.* Liege University (2005).

[39] D. Kharzeev and R. L. Thews. “Quarkonium formation time in a model-independent approach”. *Phys. Rev. C* 60 (1999), p. 041901.

[40] H. Satz D. Kharzeev. “Quarkonium formation time in a model-independent approach”. *Phys. Lett. B* 366 (1996), pp. 316–322.

[41] A. Andronic et al. “Heavy-flavour and quarkonium production in the LHC era: from proton-proton to heavy-ion collisions”. *Eur. Phys. J. C* 76 (2016), p. 107.

[42] H. Fritzsch. “Producing heavy quark flavors in hadronic collisions- A test of quantum chromodynamics”. *Phys.Lett.B* 67 (1977), pp. 217–221.

[43] R. Baier and R. Rückl. “Hadronic production of J/ψ and $\varUpsilon$: Transverse momentum distributions”. *Phys. Lett. B* 102.5 (1981), pp. 364 –370.

[44] R. Baier and R. Ruckl. “Hadronic Collisions: A Quarkonium Factory”. *Z. Phys.* C19 (1983), p. 251.

[45] F. Abe et al. (CDF collaboration). “J/ψ and ψ(2S) production in $p\bar{p}$ collisions at $\sqrt{s}$ =1.8 TeV.” *Phys. Rev. Lett.* 79 (4), pp. 572–577.

[46] Bodwin G. T., Braaten E., and Lepage G. P. “Rigorous QCD analysis of inclusive annihilation and production of heavy quarkonium”. *Phys. Rev.* D51 (1995), pp. 1125–1171.

[47] G. C. Nayak. “Proof of NRQCD factorization at all orders in the coupling constant in heavy quarkonium production”. *The European Physical Journal C* (2016), p. 448.

[48] G. T. Bodwin. “Proceedings of The 5th International Workshop on Charm Physics (Charm 2012)” (2012).

[49] B. Abelev et al. (ALICE Collaboration). “Measurement of quarkonium production at forward rapidity in pp collisions at $\sqrt{s}$ =7 TeV”. *Eur. Phys. J. C* 74 (2014), p. 2974.

[50] R. Aaij et al. (LHCb Collaboration). “Measurement of J/ψ polarization in pp collisions at $\sqrt{s} = 7$ TeV”. *Eur. Phys. J. C* 73.11 (2013), p. 2631.

[51] R. Aaij et al. (LHCb Collaboration). “Measurement of the η_c (1S) production cross-section in proton-proton collisions via the decay η_c (1S) $\rightarrow p\bar{p}$”. *The Eur. Phys. J. C* 75.7 (2015), p. 311.

[52] M. Butenschoen, Z. He, and B. A. Kniehl. “η_c Production at the LHC Challenges Nonrelativistic QCD Factorization”. *Phys. Rev. Lett.* 114 (2015), p. 09200.

[53] T. Matsui and H. Satz. “J/ψ Suppression by Quark-Gluon Plasma Formation”. *Phys. Lett. B* 178 (1986), p. 415.

[54] Karsch F., Mehr M. T., and Satz H. “Color screening and deconfinement for bound states of heavy quarks”. *Z. Phys. C Particles and Fields* 37.4 (1988), pp. 617–622.

[55] N. Brambilla et al. “Heavy quarkonium in a weakly-coupled quark-gluon plasma below the melting temperature”. *JHEP* 9 (2010), p. 38.

[56] A. Rothkopf. “A first look at Bottomonium melting via a stochastic potential”. *JHEP* 1404 (2014), p. 085.

[57] P. Braun-Munzinger and J. Stachel. “On Charm Production near the Phase Boundary”. *Nucl.Phys.A* 690 (2001), pp. 119–126.

[58] R. L. Thews, M. Schroedter, and J. Rafelski. “Enhanced J/ψ Production in Deconfined Quark Matter”. *Phys.Rev.C* 63 (2001), p. 054905.

[59] R. L. Thews. “Quarkonium Formation at High Energy”. *Nucl.Phys. A* 702 (2002), pp. 341–345.

[60] P. Braun-Munzinger, I. Heppe, and J. Stachel. “Chemical equilibration in Pb+Pb collisions at the SPS”. *Phys.Lett.B* 465 (1999), pp. 15–20.

[61] A.Andronic et al. “Evidence for charmonium generation at the phase boundary in ultra relativistic nuclear collisions”. *Phys.Lett.B* 652 (2007), pp. 259–261.

[62] X Zhao and R. Rapp. “Charmonium in Medium: From Correlators to Experiment”. *Phys.Rev.C* 82 (2010), p. 064905.

[63] X Zhao and R. Rapp. “Medium modifications and production of charmonia at LHC”. *Nucl.Phys.A* 859 (2011), pp. 114–124.

[64] K. Zhou et al. “Medium effects on charmonium production at ultrarelativistic energies available at the CERN Large Hadron Collider”. *Phys. Rev. C* 89 (2014), p. 054911.

[65] R. Rapp L. Grandchamp. “Thermal versus Direct J/ψ Production in Ultrarelativistic Heavy-Ion Collisions”. *Phys.Lett.B* 523 (2001), pp. 60–66.

[66] X. Zhao and R. Rapp. “Transverse momentum spectra of J/ψ in heavy-ion collisionss”. *Phys.Lett.B* 664 (2008), pp. 253–257.

[67] E.G. Ferreiro. “Charmonium dissociation and recombination at LHC: Revisiting comovers”. *Phys. Lett. B* 731 (2014), p. 57.

[68] G. Baur, K. Hencken, and D. Trautmann. “Photon-photon and photon-hadron interactions at relativistic heavy ion colliders”. *Progress in Particle and Nuclear Physics* 42 (1999). Heavy Ion Collisions from Nuclear to Quark Matter, pp. 357 –366.

[69] B. Abelev et al. (ALICE Collaboration). “Coherent J/ψ photoproduction in ultra-peripheral Pb–Pb collisions at $\sqrt{s_{\rm NN}} = 2.76$ TeV”. *Phys.Lett. B* 718 (2013), pp. 1273–1283.

[70] N. Brambilla et al. “Heavy quarkonium: progress, puzzles, and opportunities”. *Eur. Phys. J.* C71.2 (2011), p. 1534.

[71] R. Vogt. “Cold nuclear matter effects on J/ψ and Υ production at energies available at the CERN Large Hadron Collider (LHC)”. *Phys. Rev. C* 81 (2010), p. 044903.

[72] K.J. Eskola, H. Paukkunen, and C.A. Salgado. “EPS09: a new generation of NLO and LO nuclear parton distribution functions”. *JHEP* 0904 (2009), p. 065.

[73] C. Lourenço, R. Vogt, and H. K. Wöhri. “Energy dependence of J/ψ absorption in proton-nucleus collisions”. *Journal of High Energy Physics* 02 (2009), p. 014.

[74] Cronin J. W. et al. “Production of hadrons at large transverse momentum at 200, 300, and 400 GeV”. *Phys. Rev. D* 11 (1975), pp. 3105–3123.

[75] J. Hufner, Y. Kurihara, and H. J. Pirner. “Gluon Multiple Scattering and the Transverse Momentum Dependence of J/ψ Production in Nucleus Nucleus Collisions”. *Phys. Lett.* B215 (1988), pp. 218–222.

[76] A. Andronic et al. “Statistical hadronization of heavy quarks in ultra-relativistic nucleus-nucleus collisions”. *Nucl. Phys. A* 789.1 (2007), pp. 334 –356.

[77] A. Andronic for the ALICE Collaboration. “Experimental results and phenomenology of quarkonium production in relativistic nuclear collisions”. *Nucl. Phys. A* 931 (2014), pp. 135–144.

[78] H. Satz. "Calibrating the In-Medium Behavior of Quarkonia". *Advances in High Energy Physics* (2013), pp. 1–6.

[79] B. Abelev et al. (ALICE Collaboration). "D-meson production in p-Pb collisions at $\sqrt{s_{\rm NN}} = 5.02$ TeV and in pp collisions at $\sqrt{s}$ =7 TeV". *Phys.Rev.C* 94 (2016), p. 054908.

[80] R. Arnaldi. "J/ψ production in p-A and A-A collisions at fixed target experiments". *Nuclear Physics A* 830.1 (2009). Quark Matter 2009, pp. 345c –352c.

[81] Adare L. et al. (PHENIX Collaboration). "J/ψ suppression at forward rapidity in Au + Au collisions at $\sqrt{s_{\rm NN}} = 200$ GeV". *Phys. Rev. C* 84 (5 2011), p. 054912.

[82] B. Abelev et al. (ALICE Collaboration). "J/ψ Suppression at Forward Rapidity in Pb-Pb Collisions at $\sqrt{s_{\rm NN}} = 2.76$ TeV". *Phys.Rev.Lett* 109 (2012), p. 072301.

[83] B. Abelev et al. (ALICE Collaboration). "Centrality, rapidity and transverse momentum dependence of J/ψ suppression in Pb-Pb collisions at $\sqrt{s_{\rm NN}} = 2.76$ TeV with ALICE". *Phys. Lett. B* 734 (2014), pp. 314–327.

[84] B. Abelev et al. (ALICE Collaboration). "Inclusive, prompt and non-prompt J/ψ production at mid-rapidity in Pb–Pb collisions at $\sqrt{s_{\rm NN}} = 2.76$ TeV". *JHEP* 07 (2015), p. 051.

[85] Adam J. et al. (ALICE Collaboration). "Measurement of an excess in the Yield of J/ψ at very low p_T in Pb–Pb Collisions at $\sqrt{s}_{NN} = 2.76$ TeV". *Phys. Rev. Lett.* 116 (22 2016), pp. 222–301.

[86] R. Vogt. "Ultrarelativistic Heavy-Ion Collisions" (2007).

[87] G. Aad et al. (ATLAS Collaboration). "The ATLAS Experiment at the CERN Large Hadron Collider". *JINST* 3.08 (2008), S08003.

[88] S. Chatrchyan et al. (CMS Collaboration). "The CMS experiment at the CERN LHC". *JINST* 3.08 (2008), S08004.

[89] S. Chatrchyan et al. (CMS Collaboration). "Observation of a new boson at a mass of 125 GeV with the CMS experiment at the LHC". *Phys. Lett. B* 1 (2012), pp. 30 –61.

[90] G. Aad et al. (ATLAS Collaboration). "Observation of a new particle in the search for the Standard Model Higgs boson with the ATLAS detector at the LHC". *Phys. Lett. B* 1 (2012), pp. 1 –29.

[91] A. Alves Jr et al. (LHCb Collaboration). "The LHCb experiment at the CERN LHC". *JINST* 3.08 (2008), S08005.

[92] K. Aamodt et al. (ALICE Collaboration). "The ALICE experiment at the CERN LHC". *JINST* 3.08 (2008), S08002.

[93] A. Tauro. "ALICE Schematics" (2017). General Photo.

[94] K. Aamodt et al. (ALICE Collaboration). "Definition of the ALICE coordinate system and basic rules for sub-detector components numbering". *ALICE-INT-2003-028* (2003).

[95] K. Aamodt et al. (ALICE Collaboration). "Performance of the ALICE VZERO system". *JINST* 8.10 (2013), P10016.

[96] S.Van Der Meer. ISR-PO/68-31, KEK68-64.

[97] B Alessandro et al. (ALICE Collaboration). "ALICE: Physics Performance Report, Volume II". *Journal of Physics G: Nuclear and Particle Physics* 32.10 (2006), p. 1295.

[98] B. Abelev et al. (ALICE Collaboration). "Technical Design Report for the Upgrade of the ALICE Inner Tracking System". *J. Phys.* G41 (2014), p. 087002.

[99] J Alme et al. "The ALICE TPC, a large 3-dimensional tracking device with fast readout for ultra-high multiplicity events". *Nucl.Instrum.Meth.A* 622 (2010), pp. 316–367.

[100] Harald Appelshäuser et al. *Space-charge distortion measurements and their calibration in the ALICE TPC.* Paper in preparation.

[101] B. Abelev et al. (ALICE Collaboration). "J/ψ and ψ(2s) production in pp collisions at $\sqrt{s}$= 7 TeV". *Eur.Phys.J.C* 71 (2011), p. 1655.

[102] C. Lippmann. "Particle identification". *Nucl. Instrum. Meth.* A666 (2012), pp. 148–172.

[103] ALICE figure repository.

[104] S. Acharya et al. (ALICE Collaboration). "The ALICE Transition Radiation Detector: Construction, operation, and performance". *Nucl. Instr.Meth. A* 881 (2018), pp. 88 –127.

[105] A. Akindinov et al. "The ALICE Time-Of-Flight system: Construction, assembly and quality tests". *Nuovo Cimento B* 124 (2009), p. 235.

[106] B. Abelev et al. (ALICE Collaboration). “The Zero Degree Calorimeters for the ALICE Experiment”. *Nucl. Instrum. Methods Phys. Res., A* 581 (2007), pp. 397–401.

[107] B. Abelev et al. (ALICE Collaboration). “Measurement of the Cross Section for Electromagnetic Dissociation with Neutron Emission in Pb–Pb Collisions at $\sqrt{s_{\rm NN}} = 2.76$ TeV”. *Phys.Rev.Lett* 109 (2012), p. 252302.

[108] Brun R., Rademakers F., et al. *ROOT web page,* `http://root.cern.ch/`. 2001.

[109] “GEANT, Detector descriptions and simulation tool” (1993). http://wwwasd.web.cern.ch/geant/.

[110] X. N. Wang and M. Gyulassy. “Monte Carlo model for multiple jet production in pp, pA, and AA collisions”. *Phys. Rev. D* 44 (1991), p. 3501.

[111] W. T. Deng, X. N. Wang, and R. Xu. “Hadron production in p+p, p+Pb, and Pb+Pb collisions with the HIJING 2.0 model at energies available at the CERN Large Hadron Collider”. *Phys. Rev. C* 83 (2011), p. 014915.

[112] S. Agostinelli et al. “Geant4 a simulation toolkit”. *Nuclear Instruments and Methods in Physics Research Section A: Accelerators, Spectrometers, Detectors and Associated Equipment* 506.3 (2003), pp. 250 –303.

[113] B. Nilsson-Almqvist B. Andersson G. Gustafson. “A model for low-pT hadronic reactions with generalizations to hadron-nucleus and nucleus-nucleus collisions”. *Nucl. Phys. B* 281.1 (1987), pp. 289 –309.

[114] W. T. Deng, X. N. Wang, and R. Xu. “Gluon shadowing and hadron production in heavy-ion collisions at LHC”. *Phys. Lett. B* 701 (2011), pp. 133–136.

[115] R. Fruhwirth. “Application of Kalman filtering to track and vertex fitting”. *Nucl. Instr. and Meth. A* 262 (1987), p. 44.

[116] B. Abelev et al. (ALICE Collaboration). “Performance of the ALICE Experiment at the CERN LHC”. *Int. J. Mod. Phys. A* 29 (2014), p. 1430044.

[117] B. Abelev et al. (ALICE Collaboration). “Centrality determination of Pb-Pb collisions at $\sqrt{s_{\rm NN}} = 2.76$ TeV with ALICE”. *Phys. Rev. C* 88 (2013), p. 044909.

[118] S. Acharya et al. (ALICE Collaboration). *Centrality determination in heavy ion collisions.* ALICE Public note in preparation.

[119] Oystein Djuvsland and Joakim Nystrand. “Single and Double Photonuclear Excitations in Pb+Pb Collisions at $\sqrt{s_{\rm NN}} = 2.76$ TeV at the CERN Large Hadron Collider”. *Phys. Rev. C* 83 (2011), p. 041901.

[120] “Generator for $e^{+}e^{-}$ pairs in Pb–Pb collisions at LHC” (2017). ALICE internal analysis note, ALICE-ANA-2002-27.

[121] B. Alver et al. “The PHOBOS Glauber Monte Carlo” (2008). arXiv: `0805.4411 [nucl-ex]`.

[122] *Luminosity determination for ultra-peripheral triggers in Pb-Pb at* $\sqrt{s_{\rm NN}} = 5.02$ *TeV*. ALICE internal note, ANA-3619.

[123] R.T. Jimenez Bustamante et al. *J/ψ production in Pb–Pb collisions at* $\sqrt{s}_{NN} = 5.02$ *TeV*. ALICE internal analysis note (2017).

[124] Hess. B. *Particle Identification in Jets and High-Multiplicity pp Events with the ALICE TPC.* Tubingen U. (2015).

[125] D. Weiser. *Ph.D thesis in preparation.* Ruprecht-Karls-Universität Heidelberg.

[126] P. Braun-Munzinger P. Crochet. “Investigation of background subtraction techniques for high mass dilepton physics”. *Nucl. Instrum. Meth A* 484 (2002), pp. 564–572.

[127] D. L’Hote. “About resonance signal extraction from multiparticle data: combinatorics and event mixing methods”. *Nucl. Instrum. Meth. A* 337.2 (1994), pp. 544 –556.

[128] D. Acosta et al. (ALICE Collaboration). “Rapidity and transverse momentum dependence of inclusive J/ψ production in pp collisions at $\sqrt{s}$ =7 TeV”. *Physics Letters B* 704.5 (2011), pp. 442 –455.

[129] Abelev B. et al. (ALICE collaboration). “Measurement of prompt J/ψ and beauty hadron production cross sections at mid-rapidity in *pp* collisions at $\sqrt{s} = 7$ TeV”. *JHEP* 11 (2012), p. 065.

[130] S. Acharya et al. (ALICE collaboration). “J/ψ elliptic flow in Pb-Pb collisions at $\sqrt{s_{\rm NN}} = 5.02$ TeV”. *Phys. Rev. Lett.* 119.24 (2017), p. 242301.

[131] A. Jaroslav et al. (ALICE collaboration). "Differential studies of inclusive J/ψ and ψs(2S) production at forward rapidity in Pb-Pb collisions at $\sqrt{s_{\rm NN}} = 2.76$ TeV". *JHEP* 05 (2016), p. 179.

[132] K.J. Eskola, H. Paukkunen, and C.A. Salgado. "The scale dependent nuclear effects in parton distributions for practical applications". *Eur.Phys.J.* C9 (1999), pp. 61–68.

[133] P. Z. Skands. "Tuning Monte Carlo Generators: The Perugia Tunes". *Phys. Rev.* D82 (2010), p. 074018.

[134] D.J. Lange. "The EvtGen particle decay simulation package". *Nucl. Instrum. Meth. A* 462 (2001), p. 152.

[135] E. Barberio and Z.Was. "PHOTOS - a universal Monte Carlo for QED radiative corrections: version 2.0". *Comput. Phys. Commun.* 79 (1994), p. 291.

[136] A. Jaroslav et al. (ALICE collaboration). "D-meson production in p-Pb collisions at $\sqrt{s_{\rm NN}}$ =5.02 TeV and in pp collisions at $\sqrt{s}$ =7 TeV". *Phys. Rev.* C94.5 (2016), p. 054908.

[137] B. Abelev et al. (ALICE collaboration). "Measurement of prompt J/ψ and beauty hadron production cross sections at mid-rapidity in pp collisions at $\sqrt{s} = 7$ TeV". *JHEP* 11 (2012), p. 065.

[138] B. Audurier. "Etude de la production inclusive de J/ψ dans les collisions pp et Pb-Pb at $\sqrt{s}_{NN} =$ 5.02 TeV avec le spectrometre a muons de l'experience ALICE au LHC". PhD thesis. Nantes University, (2017).

[139] Bossu F. et al. "Phenomenological interpolation of the inclusive J/ψ cross section to proton-proton collisions at 2.76 TeV and 5.5 TeV" (2011). arXiv: `1103.2394 [nucl-ex]`.

[140] J. K. Yoh et al. "Study of Scaling in Hadronic Production of Dimuons". *Phys. Rev. Lett.* 41 (10 1978), pp. 684–687.

[141] B. Abelev et al. (ALICE Collaboration). "Rapidity and transverse-momentum dependence of the inclusive J/ψ nuclear modification factor in p-Pb collisions at $\sqrt{s_{\rm NN}} = 5.02$ TeV". *JHEP* 2015.6 (2015), p. 55.

[142] A. Adare et al. (PHENIX Collaboration). "Ground and excited charmonium state production in $p + p$ collisions at $\sqrt{s} = 200$ GeV". *Phys. Rev.* D85 (2012), p. 092004.

[143] D. Acosta et al. (ALICE Collaboration). "Inclusive J/ψ production in pp collisions at $\sqrt{s} = 2.76$ TeV". *Phys. Lett. B* 718.2 (2012), pp. 295 –306.

[144] A. Maire. *Interpolation of J/ψ production cross-sections at $y \approx 0$ in pp collisions at $\sqrt{s}$ =2.76 TeV and 5.02 TeV.* unpublished ALICE internal note, 2015.

[145] J. Book. *J/ψ production in Pb–Pb collisions with ALICE at the LHC.* Johann Wolfgang Goethe Universität, Frankfurt am Main. 2014.

[146] S. Acharya et al. (ALICE Collaboration). "Energy dependence of forward-rapidity J/ψ and ψ(2S) production in pp collisions at the LHC". *Eur. Phys. J.* C77.6 (2017), p. 392.

[147] L. Layer. *Beauty production in Pb–Pb with the ALICE experiment at $\sqrt{s_{\rm NN}} = 5.02$ TeV.* Master thesis. Ruprecht-Karls-Universität Heidelberg (2018).

[148] R. Barlow. "Systematic errors: Facts and fictions, in Advanced Statistical Techniques in Particle Physics". *Advanced Statistical Techniques in Particle Physics. Proceedings, Conference, Durham, UK* (2002).

[149] J. Adam et al. (ALICE Collaboration). "J/ψ suppression at forward rapidity in Pb–Pb collisions at $\sqrt{s}_{NN} = 5.02$ TeV". *Phys.Lett.B.* 766 (2017), pp. 212–214.

[150] A.Andronic et al. "Hadron yields, the chemical freeze-out and the QCD phase diagram". *J. Phys. Conf. Ser.* 779.1 (2017), p. 012012.

[151] M. Cacciari et al. "Theoretical predictions for charm and bottom production at the LHC". *JHEP* 10 (2012), p. 137.

[152] X. Du and R. Rapp. "Sequential Regeneration of Charmonia in Heavy-Ion Collisions". *Nucl. Phys.* A943 (2015), pp. 147–158.

[153] X.Zhao and R.Rapp. Private communication to Andronic. A.

[154] P. Zhuang. Private communication to Andronic. A.

[155] Ferreiro E. Private communication to Andronic A.

[156] M. Köhler and A. Andronic and others. Private communication.

[157] "The iEBE-VISHNU code package for relativistic heavy-ion collisions". *Computer Physics Communications* 199 (2016), pp. 61 –85.

[158] L. Adare et al. (PHENIX Collaboration). *Phys. Rev. Lett.* 98 (23 2007), p. 232301.

[159] Adamczyk L. et al. (STAR Collaboration). "J/ψ production at low p_T in Au + Au and Cu + Cu collisions at $\sqrt{s_{NN}} = 200$ GeV with the STAR detector". *Phys. Rev. C* 90 (2 2014), p. 024906.

[160] L. Adamczyk et al. (STAR Collaboration). "J/ψ production at high transverse momenta in $p+p$ and Au+Au collisions at $\sqrt{s_{NN}} = 200$ GeV". *Phys. Lett.* B722 (2013), pp. 55–62.

[161] A. Andronic. "Experimental results and phenomenology of quarkonium production in relativistic nuclear collisions". *Nuclear Physics A* 931 (2014). Quark Matter 2014, pp. 135 –144.

[162] S. Acharya et al. (ALICE Collaboration). "J/ψ elliptic flow in Pb-Pb collisions at $\sqrt{s_{\mathrm{NN}}} = 5.02$ TeV". *Phys. Rev. Lett.* 119.24 (2017), p. 242301.

[163] "ALICE luminosity determination for pp collisions at $\sqrt{s} = 5$ TeV" (2016). ALICE-PUBLIC-2016-005.

Acknowledgments

I want to thank all the people that helped me to accomplish my Ph.D. research project, the completion of this thesis, and the support during the last four years.

First of all, I would like to thank Prof. Dr. Silvia Masciocchi for giving me the opportunity of doing my Ph.D. in the GSI group. Silvia, thanks for all the support, the endless energy, patience and for pushing me forward. Thanks to Prof. Stephanie Hansmann-Menzemer for agreeing to be the second referee of this thesis, and to Prof. Carlo Ewerz and Prof. Stefan Jordan for accepting to serve as members of the examination committee.

A special mention to the members of the ALICE group at Oslo University, Ionut Arsene and Antone Lardeaux, for hosting me for a couple of months. Thanks for all the support, the nice, detailed and long discussions. The time in Nordic countries had an enormous impact on this work, and I profit from the wonderful collaboration atmosphere of the group. My stay abroad would not have been possible without the support of the Helmholtz Graduate School for Hadron and Ion Research (HGS-HIRe).

Thanks to Andrea Dubla, Steffen Weber, Julius Gronefeld, Alexander Deisting, Anton Andronic, Jana Crkovská and Kai Schweda for reading my thesis. I appreciate your time and patience, all your suggestions helped to improve the quality of my work. Special thanks to Andrea Dubla and Steffen Weber for the countless discussions during the last years. Thanks to the whole ALICE GSI group for the excellent and friendly work environment. I am very grateful to all the people of the J/ψ dielectron working group for providing feed-back suggestions and valuable comments during our Monday meetings.

Thanks to Denise and Karin for the efficient support in all kind of non-physics related topics. Thanks also to all the friends for all the pleasant memories during my last years.

En notas más personales gracias a mi hermano César por el apoyo y los buenos momentos en tierras teutonas. Edgar, gracias por el apoyo y la amistad durante el doctorado. Nos seguimos formando en el camino de la ciencia.

Finalmente, mi más grande agradecimiento a mi madre Luz María, mi padre Raúl, mi abuela Luz María, a mis hermanos Ehecatl y Tlacaelel por su carino e inspiración. Ustedes son mi motor para seguir adelante en todo.

Financial support is also acknowledged from the Consejo Nacional de Ciencia y Tecnologia (CONACYT No. de Becario 269759).

List of Figures

Index of tables